ELEMENTAL SUBSTITUTIONS IN LEAD ZIRCONATE TITANATE:
A COMBINED DENSITY FUNCTIONAL THEORY AND EXPERIMENTAL STUDY

ZHANG ZHEN

NATIONAL UNIVERSITY OF SINGAPORE

2008

ELEMENTAL SUBSTITUTIONS IN LEAD ZIRCONATE TITANATE:
A COMBINED DENSITY FUNCTIONAL THEORY AND EXPERIMENTAL STUDY

ZHANG ZHEN

(Bachelor of Science, Fudan University, Shanghai, China)

A THESIS SUBMITTED

FOR THE DEGREE OF DOCTOR OF PHILOSOPHY OF

MATERIALS SCIENCE DIVISION,

DEPARTMENT OF MECHANICAL ENGINEERING,

NATIONAL UNIVERSITY OF SINGAPORE

2008

ACKNOWLEDGEMENTS

I am pleased to take this opportunity to appreciate many people for their support and encouragement, without which, it would have been impossible for me to complete this thesis.

First and foremost, I would like to express my heartfelt appreciations to my supervisor, Prof. Lu Li, from Department of Mechanical Engineering, National University of Singapore (NUS), for his strong support and guidance, as well as continuous understanding and encouragement in the past four years. I would also like to thank Dr. Wu Ping, from Institute of High Performance Computing (IHPC) for the invaluable ideas and stimulating advice, which are of vital importance to this thesis. I am also grateful to Prof. Shu Chang, from Department of Mechanical Engineering, NUS, for his support and encouragement. Working with their supervisions is such a rewarding and pleasant experience.

Thanks will also go to some special individuals in IHPC. Many thanks to Dr. Yu Zhigen for his immense help, constructive comments, and important discussions. I would also like to thank Dr. Michael B. Sullivan, for his professional grammatical and typographic corrections in this thesis. Thanks to Dr. Ong Phuong Khuong, Dr. Bai Kewu, and Dr. Zhang Shuowang for the discussions and help.

In addition, I want to thank Department of Mechanical Engineering, National University of Singapore, and Institute of High Performance Computing, for providing computing resources and funding to this research.

Finally, a heartwarming thank to my family. Thanks for my wife Hellen Jiang Hanglei, and my parents for the love, understanding and support throughout my life.

TABLE OF CONTENTS

SUMMARY

We systematically and exhaustively investigate the effects of elemental substitutions on the ferroelectric properties of lead zirconate titanate (PZT), using first-principle density functional theory calculations. Our studies reveal that different mechanisms behind governing the improved ferroelectric properties of lead zirconate titanate with regards to the donor substitutions and the acceptor substitutions.

For donors substitutions, we conclude that two mechanisms contribute to the improved ferroelectric properties in the donor-doped PZT. First, the formation energy of the oxygen vacancies is increased by substituted donors, resulting in a diluted oxygen vacancy concentration in the lead zirconate titanate lattice. Therefore the domain pinning effect and space charge effect are reduced. Second, the electronic states of donors share the conduction band minima with the Ti 3d states, reduce the occupation of the Ti 3d states by the electrons released by the formation of oxygen vacancies, and weaken the electronic suppression effect on the polarization in lead zirconate titanate.

It is also interesting to observe the systematic variation in the band gaps of lead zirconate titanate with the donor substitutions. For the group IIIA elements substituted

lead titanate by A-site donors, we find that correlations between the dopant electrons introduce the Mott-Hubbard band gap into PZT, which is intrinsically a charge-transfer insulator. This leads to a systematic reduction of energy and optical band gaps with increased atomic number of group IIIA elements. The similar chemical trend is found for group VB substitutes, which is, however, closely related to the electron bandwidth of Ti 3d states in the charge-transfer band gaps.

For acceptor substitutions, the mechanisms dominating the substitution effects on the improved ferroelectric properties are related to the defect structures. Through our calculations, we identify three types of defects structures for different types of acceptors: isolated point defects, cluster structure along z direction, and cluster structure in xy plane. More importantly, our calculations reveal that the acceptor-oxygen-vacancy-acceptor cluster structure either along z direction or in xy plane is energetically preferred for most acceptors substituted lead zirconate titanate. This cluster configuration greatly reduces the oxygen vacancy mobility, therefore diminishing the domain pinning effects and space charge effects. Moreover, close examinations of the atomic positions in the clusters indicate that the domain pinning enforced by the tail-to-tail polarization patterns along the z direction are relieved by the group IIIB and 3d transition metal substitutes. However, the more striking finding is that the group VB substitutes induce head-to-head polarization patterns in the xy plane, which makes the domain pinning effects even weaker.

In summary, we predict that group VA elements (V^{5+}, Nb^{5+}, Ta^{5+}) and group VIA elements (W^{6+}, Mo^{6+}) as B-site donors, group IIIA elements (Sc^{3+}, Y^{3+} and La^{3+}) as A-site donors, and the group IIIB elements (Al^{3+}, Ga^{3+}, In^{3+}, Tl^{3+}), group VB(Bi^{3+}, Sb^{3+}), transition mental elements (Mn^{3+}, Fe^{3+}) as B-site acceptors can effectively improve the ferroelectric properties and degradation behaviors of PZT. It is also noteworthy that Nb^{5+} Ta^{5+} and W^{6+} among all the donors, and Bi^{3+}, Sb^{3+} among all the acceptors are theoretically predicted to have the optimal substitution effects.

Experimental verification on W substituted lead zirconate titanate is conducted following the theoretical predictions. The microstructure, ferroelectric property, and degradation behavior of the fabricated W-substituted PZT are characterized. The experimental results are in consistency with our theoretical predictions.

In this work, the highly efficient theoretical calculations are conducted before the experimental investigations. Moreover, they work as guidance to the experimental realizations. Therefore, we believe that the methodology adopted in this work opens a way for future computational material design.

LIST OF TABLES

LIST OF FIGURES

LIST OF PUBLICATIONS

1. **Zhen Zhang**, Ping Wu. Li Lu and Chang Shu, Study on vacancy formation in ferroelectric PbTiO3 from *ab initio*, **Applied Physics Letters** 88, 142902 (2006)

2. **Zhen Zhang**, Ping Wu. Li Lu and Chang Shu, Computational investigation of donor doping effect on fatigue behavior of lead zirconate titanate, **Applied Physics Letters** 89, 152909 (2006).

3. **Zhen Zhang**, Li Lu, Chang Shu, Ping Wu, and Wendong Song, Ferroelectric properties of W-doped lead zirconate titanate, **Journal of Applied Physics** 102, 074119 (2007).

4. **Zhen Zhang**, Ping Wu, Khuong P. Ong, Li Lu and Chang Shu, Electronic properties of A-site substituted lead zirconate titanate: Density functional calculations, **Physical Review B** 76, 125102 (2007).

5. **Zhen Zhang**, Ping Wu, Li Lu, and Chang Shu, *Ab-initio* study of formations of neutral vacancies in ferroelectric $PbTiO_3$ at different oxygen atmospheres, **Journal of Alloys and Compounds** 449, 362 (2008).

6. **Zhen Zhang**, Ping Wu. Li Lu and Chang Shu, Defect and electronic structures of acceptor substituted lead titanate, **Applied Physics Letters** 92, 112909 (2008).

7. **Zhen Zhang**, Shijie Wang, Wendong Song, Li Lu, Chang Shu, and Ping Wu, Comparative study of effects of Mo and W doping on the ferroelectric property of $Pb(Zr_{0.3}Ti_{0.7})O_3$ thin films, **Journal of Physics D** 41, 135402 (2008).

8. **Zhen Zhang**, Ping Wu, Li Lu, and Chang Shu, Acceptor Modulated Defect and Electronic Structures in Ferroelectric Lead Titanate, **Functional Material Letters** (In press).

Chapter I

Introduction

This chapter is intended as a brief introduction to this thesis. Section 1.1 offers a short overview of the applications and development of lead zirconate titanate, as well as introduces the reliability issues. Besides, the current research status on the degradation enhancement of lead zirconate titanate is briefly reviewed. Most importantly, the motivations of this thesis are presented. In Section 1.2, the outline of this thesis is described.

1.1 Overview & Motivations

As one of the most important perovskite ferroelectrics, lead zirconate titanate (PZT, formula: $Pb(Zr_xTi_{1-x})O_3$ $0<x<1$), since its discovery, have been receiving wide-scale academic and industrial attentions due to their rich functionality and potential applications. Lead zirconate titanate has remarkable ferroelectric and piezoelectric effects, which feature superior remnant polarization, high dielectric constants, outstanding piezoelectric electromechanical coupling factor, superb piezoelectric coefficient, and low process temperatures. These merits bring about a wide range of applications, such as actuators, tunable devices and optical devices, and nonvolatile memories [1-6].

However, for the realization of the high-density commercially available PZT-based ferroelectric devices, some technical reliability issues still remain unresolved [7-10]. These reliability concerns of the ferroelectric PZT include fatigue, retention, and imprint. All three degradations accompany the loss of the polarization, which makes0 it hard to obtain high density ferroelectric devices.

The mechanisms behind these reliability issues have been intensively explored from the prospects of both experiments and theoretical simulations, and abundant evidences have revealed that these reliability issues are closely related to the defects in the lead zirconate titanate lattice [7-10]. Many models have also been proposed, among which the space charge effect [11], the domain pinning effect [12-15], and the electronic

suppression effect [16, 17] are widely accepted as the origins of the property degradations in the ferroelectric perovskite oxides.

In addition to understanding the mechanisms behind the reliability issues, much effort has also been made to improve the degradation behaviors of PZT [18-32]. Currently, elemental substitution has proven to be a very effective way to control the ferroelectric behaviors of PZT [20-31]. A significant number of experimental studies on substituted PZT thin films have been conducted, resulting in an optimized PZT material with excellent properties. A great number of the donors, including Nb^{5+}, Ta^{5+}, W^{6+}, and Mo^{6+} as the B-site donors, and Y^{3+}, La^{3+} and the aliovalent rare-earth elements as the A-site donors, have been investigated experimentally on the PZT thin films, and improved ferroelectric properties were reported for these groups of dopants [20-26, 33-35]. In contrast to the results on the donor-doped PZT, the experiments on the acceptors doped PZT thin films are relatively fewer. Only Fe^{3+}, Mn^{3+}, Sb^{3+}, Al^{3+} as the B-site acceptors are known to us [27-31, 36].

Despite the great success in the PZT synthesis and fabrications, the investigations on the mechanisms behind the elements substitutions in PZT are frustrating, as a result of the controversial and even conflicting conclusions inferred from the experimental observations [37]. Contrary to the conventional investigations from the experiments, the *ab initio* density functional theory (DFT) studies can offer great opportunities to shed light on the mechanisms behind the doping effects, thanks to the fact that these theoretical studies are immune to the experimental conditions [38-40]. Moreover, the *ab*

initio DFT calculations describe the most fundamental nature of elements from the atomic level, which provides us a deeper understanding of the elemental substitutions. Besides, the *ab initio* calculations require no empirical data and are very cost effective, which make the large-scale material designs feasible and affordable.

Using the *ab initio* DFT calculations, several authors have reported their theoretical results of PZT doped with Nb^{5+}, La^{3+}, and Fe^{3+}. Miura and Tanaka found that in the Nb^{5+}, La^{3+} doped PZT systems, the donor dopant states at the conduction band minimum can share the remaining electrons released by the oxygen vacancies with the Ti *3d* orbitals. Thereby, the bonds between the Ti and O are maintained, and the PZT can be less susceptible to the ferroelectric fatigue [41, 42]. Mestric *et al* pointed out that acceptors associate with oxygen vacancies as defect clusters and reduce their mobility, therefore reducing the domain pinning and the space charge effects [29, 43]. These conclusions are enlightening since they enhance our understanding toward the elements substitution and provide clues to the material design for PZT-based ferroelectric devices.

However, a systematic study of doping effects of the dopants on the ferroelectric properties of PZT is still lacking. Therefore, the aim of this research is to systematically investigate the effects of elemental substitutions on the ferroelectric properties of lead zirconate titanate, using *ab initio* density functional theory calculations. The substitution candidates were exhaustively selected by screening the periodical table of elements, via matching the ionic sizes with the original ions, and choosing the desired valences for donors and acceptors. In this study, group VA, VIA elements (B-site donors), group IIA

elements (A-site donors), group IIIB elements (B-site acceptors), and group VB elements (A-site donor, B-site acceptor/donors) are investigated as the dopants in PZT. For each substituted system, the electronic structure, the ionic structure and the formation of defects are examined in order to reveal the mechanisms behind the elemental substitutions. Furthermore, we compare various mechanisms associated with the diverse groups of the dopants, and identify the distinct mechanisms for donor and acceptor substitutions.

1.2 Outline

This thesis is organized as follows:

Chapter I introduces the background and the motivations of this work.

Chapter II provides a review of the structure and applications of lead zirconate titanate. And more importantly, the origins of degradations and approaches to improve the degradations are discussed in details.

Chapter III describes the *ab-initio* calculation methodology applied in this work. The principles of the *ab-initio* calculations, the density functional theory (DFT), the generalized gradient approximation (GGA)/local density approximation (LDA), and the pseudopotentials are presented.

Chapter IV contains the discussion on the prediction of perovskite structures and the analysis of the ionic and electronic structures of lead titanate and lead zirconate titanate, which are the most fundamental studies aimed at providing important references for the following studies.

Chapter V presents the point defect calculations for lead titanate, including the neutral and charged defects. The formations of these defects under different thermodynamic conditions are studied, and their impacts on the properties of lead titanate are discussed. The study on neutral defects was published in Journal of Alloys and Compounds (volume 449, page 362), and the study on charged defects was published on Applied Physics Letters (volume 88, page 142902).

Chapter VI systematically explores the density of states, optical properties, and formations of the oxygen vacancies of the donor-substituted lead zirconate titanate. The distinct effects of different groups of the donor dopants on the ferroelectric properties are concluded. This part of study was published in Physical Review B (volume 76, page 125102) and Applied Physics Letters (volume 89, page 152909).

Chapter VII focuses on the effects of acceptor substitutions on the defect structures, electronic structures, and ferroelectric properties of lead titanate. The discrepancy between groups of acceptors is identified, and reasons behind are offered. This part of study was published in Applied Physics Letters (volume 92, page 112909) and Functional Materials Letters (In press).

Chapter VIII presents our experimental study of the W-doped lead zirconate titanate, which is theoretically predicted to be degradation-improved, which was published in Journal of Applied Physics (volume 102, page 074119).

Chapter IX concludes the main findings presented in this thesis, and suggests future research directions.

Chapter II

Literature Review

An introduction to the crystal structure of lead zirconate titanate is first offered in Section 2.1, and the most popular application of PZT as the non-volatile random access memory is presented in Section 2.2. More importantly, in Section 2.2, the current research status of the degradation origins is presented, where three important mechanisms are described in detail. Furthermore, two approaches to decreae the degradation are discussed in Section 2.3.

2.1 Structures & Application of $Pb(Zr_xTi_{1-x})O_3$

2.1.1 Structures of $Pb(Zr_xTi_{1-x})O_3$

Lead zirconate titanate (PZT, $PbZr_xTi_{1-x}O_3$) is one of the most technologically important perovskite-structure oxides. The basic chemical formula of the perovskite oxides can be expressed by ABO_3, where A and B are the cations with different valences, and O is the oxygen anion. The perovskite oxides can be regarded as cubic close packed arrangements of A and O ions with B ions filling the octahedral interstitial positions, forming a three-dimensional network of BO_6 octahedra, as shown in Fig. 2.1.

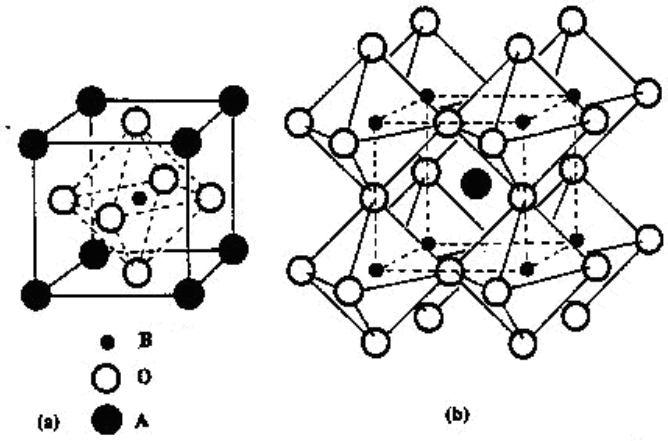

Figure 2.1: Structure of perovskite oxide: (a) A cubic ABO_3 perovskite-type unit cell, and (b) three dimensional network of corner sharing octahedra of O^{2-} ions [4].

These perovskite oxides become ferroelectric when A is a monovalent or divalent cation with a large radius and B is a pentavalent or tetravalent metal with a small radius. In both ferroelectrics and dielectrics, the positive and negative charges will be displaced from their original positions upon the application of an electric field (so-called

polarization). However, the difference between ferroelectrics and dielectrics is that the polarization vanishes in a dielectric but is maintained in a ferroelectric when the electric field goes back to zero. This spontaneous polarization of ferroelectrics in the absence of electric field comes from the displacement inherent to the crystal structure of the ferroelectrics, as we will discuss in Chapter IV. Moreover, the direction and magnitude of the polarization can be changed and reoriented by applying an electric field in cycles. A typical change of the polarization or the charge (equals to the polarization times the area) on the ferroelectric capacitor as a function of the applied voltage is shown in Fig. 2.2, which is generally known as ferroelectric hysteresis loop.

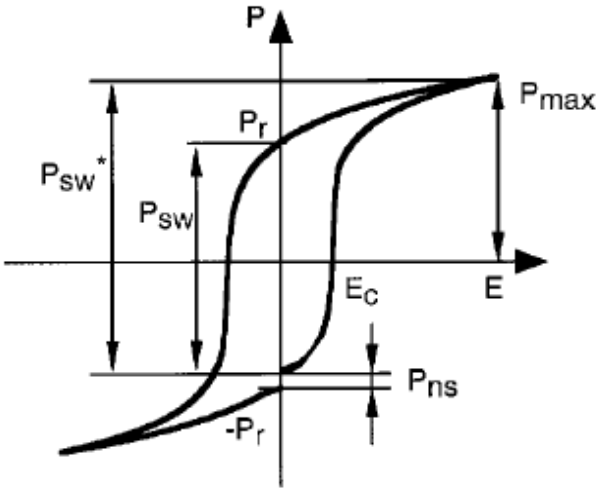

Figure 2.2: A typical polarization–electric field (*P*–*E*) hysteresis loop of ferroelectric materials. The loop is characterized by the following parameters: amplitude of cycling field (E_m), remanent polarization (P_r), switchable polarization (P_{sw}), nonswitchable polarization (P_{ns}), and coercive field (E_c).

The phase diagram of PZT is shown in Fig. 2.3. PZT has a wide range of Curie

temperatures The Curie temperature is defined as the temperature at which the phase transition between the ferroelectric to the paraelectric takes place. It increases from 230°C to 490°C as the Ti content increases from 0% to 100%. PZT has two different ferroelectric structures (tetragonal and rhombohedral) below the Curie temperature, depending on the Zr/Ti composition ratio. On the Ti rich side of the phase diagram, the PZT shows the tetragonal structure; on the Zr rich side, it has the rhombohedral structure. There is morphotropic phase boundary (MPB) region in which the tetragonal and rhombohedral structures coexist.

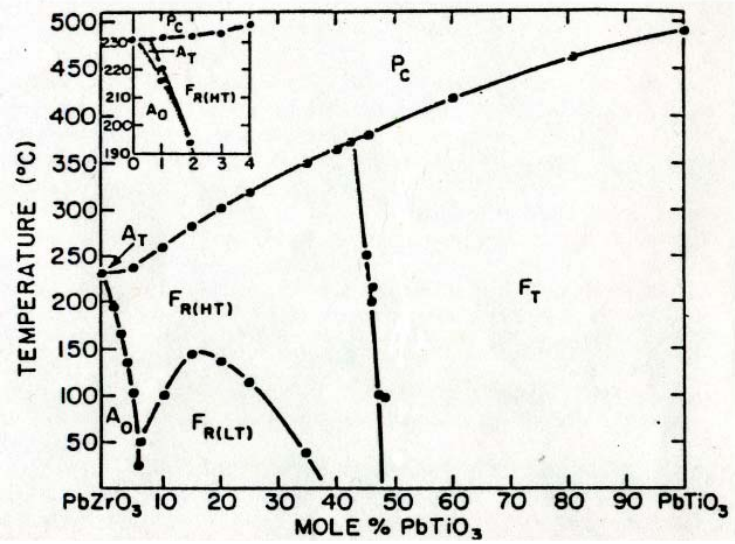

Figure 2.3: $PbTiO_3$-$PbZrO_3$ phase diagram [44].

2.1.2 Applications of $Pb(Zr_xTi_{1-x})O_3$

Lead zirconate titanate has remarkable ferroelectric and piezoelectric properties, which feature superior remnant polarizations, high dielectric constants, outstanding piezoelectric electromechanical coupling factor (k_p), superb piezoelectric coefficient (d_{ij})

and low process temperatures. These benefits have brought about a wide range of applications, such as actuators, tunable devices and optical devices, and nonvolatile memories [1-6]. Perhaps most importantly, its potential usage as a thin film material in the non-volatile random access memories (NVRAM) has been a focus of intensive research recently [6-8, 10].

The nonvolatile random access memory (NVRAM) offers features consistent with a RAM device, but is still non-volatile like a ROM device. As one of the most promising non-volatile RAM, the PZT-based ferroelectric random access memory (FeRAM) has many advantages over those widely-used memory devices currently in the market, as listed below. A comparison between FeRAM and the popular memories in the current market is also given in Table 2.1:

(1) Low voltage operation: The operation voltage is only about 1V.

(2) Fast switching: The switching time is smaller than 100 picoseconds.

(3) Good non-volatility properties: Retention time at 85°C is up to 10 years.

(4) Density comparable to DRAM: The cell structure is similar to that of DRAM.

(5) Radiation hardness: Good for space and military usage.

Table 2.1: Comparison of the characteristics of FeRAM, DRAM, SRAM, and Flash. The number in the parenthesis refers to predicted values for further generations [45].

	FeRAM	DRAM	SRAM	FLASH
Non-volatility	Yes	No	No	Yes
Write cycle	10^{12}	10^{15}	10^{15}	10^{15}
Write speed	100 ns(20 ns)	ns	ns	μs
Read cycle	10^{12}	10^{15}	10^{15}	10^{15}
Access time	100 ns(20 ns)	40 – 70 ns	6 - 70 ns	40 - 70 ns
Data retention	10 years	None	None	10 years
Relative cell size	2×-5× (1×)	1 ×	> 4 ×	1 ×

Currently, the advantages of FeRAM are particularly important in the low-density end market. FeRAM can be utilized in a variety of portable & battery operated systems, contactless smartcards, ID tags and other ultra-low power applications because of FeRAM's low voltage, low power and fast reading/writing access. Sony Playstation 2 already uses a FeRAM chip made by Fujitsu. Samsung also markets a 64 Mb FeRAM. Low-cost, and low-capacity FeRAM chips have been churned out in their millions for 'smart cards' such as Japanese railway tickets. In addition, the industry is actively using FeRAMs to replace flash in cameras and handphones. The ultimate goal of FeRAM manufacturers is to make FeRAM as the "Universal Memory" candidate, which acts as memory device in every electronic system and even replaces the widely-used RAM and hard-disk in the laptops and PCs. Many industry players including Ramtron, NEC, Panasonic, Fujitsu, and Texas Instruments are boosting the development and mass production of FeRAM.

2.2. Origins of Degradations of $Pb(Zr_xTi_{1-x})O_3$

2.2.1 Types of Degradation Behaviors

The methods for testing ferroelectric thin films have been standardized by the IEEE Committee [46]. These standards describe the methods for current transient, radiation, leakage current, fatigue, and retention. Of all the observations revealed by these tests, fatigue, retention and imprint are the three most important degradation behaviors, as shown in Figure 2.4.

(1) Fatigue: Fatigue is a characteristic of ferroelectrics where the amount of charge decreases with cycling as a bipolar voltage is repeatedly applied.

(2) Retention: Retention is the ability of a ferroelectric capacitor cell to retain its stored charges and hence the stored information for a long period of time. It measures the decrease of polarization after long-term storage described by the signal polarization with the time.

(3) Imprint: Imprint is a phenomenon where one polarization state becomes more stable than the other state, which implies a preferential polarization state for domains, usually the one into which they were first poled.

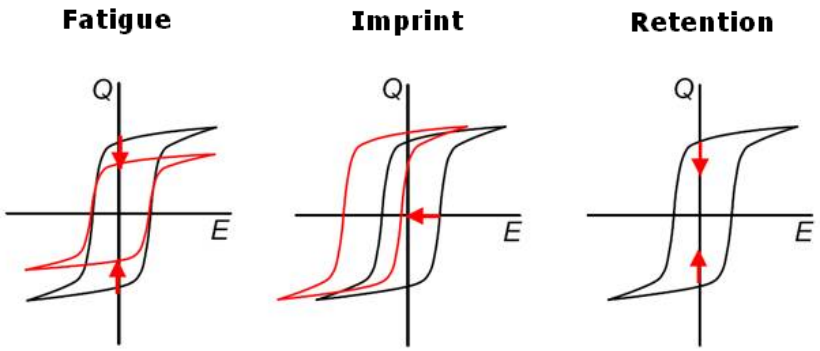

Figure 2.4: Effects of fatigue, imprint, and loss of retention on the ferroelectric cells.

Intensive academic and industrial attention has attempted to understand the origin of the fatigue. The discussions on the mechanisms behind the fatigue were quite controversial, and it has been commonly recognized that not one but many mechanisms contribute to the problem. Most importantly, it is now widely accepted that the fatigue is closely related to the defects in lead zirconate titanate lattice, and is mainly associated with the formation and redistribution of oxygen vacancies through the domain wall pinning effect, the space charge effect, and the electronic suppression effects.

2.2.2 Domain Wall Pinning Effect

The pinning of domain walls by oxygen vacancies, which pins the polarization in a particular direction, may lead to fatigue. Raman spectroscopy of KNO_3 conducted by Scott and Pouligny revealed that only a very small part of the KNO_3 sample was converted from the ferroelectric to the paraelectric phase with fatigue, which is strong evidence that fatigue must be caused by pinning of the domain walls [47]. In addition,

two other groups of researchers (Gruverman *et al* [48], and Colla *et al* [49]) also independently observed the pinning of domain walls with atomic force microscopy.

The origin of the domain pinning was first proposed by Brennan to be the oxygen vacancies perpendicular to the polarization direction [50]. This idea has been confirmed by a great portion of following studies. Arlt and Neumann demonstrated that when bulk ferroelectrics are under repetitive cycling, the oxygen vacancies can move from their originally randomly distributed sites in the perovskite structure to sites in planes parallel to the ferroelectric-electrode interface [51]. Scott and Dawber have also suggested that in thin films, a high concentration of oxygen vacancies can order themselves into planes [52]. Similar conclusions were also drawn on PZT by the atomic force microscope and on barium titanate reduced after an accelerated life test [53]. In addition, theoretical microscopic study of oxygen-vacancy defects in $PbTiO_3$ lattice also confirmed the idea that oxygen vacancies are effective at pinning domain walls [54]. As shown in Figure 2.5, 180-degree domain walls are stabilized around the oxygen vacancy sites.

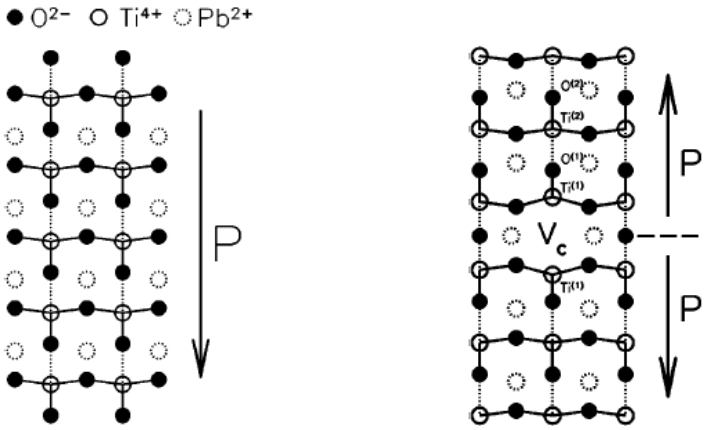

Figure 2.5: Schematic groundstate atomic structures for (a) tetragonal phase of $PbTiO_3$, and (b) tetragonal phase of $PbTiO_3$ with an oxygen vacancy along c direction [54].

2.2.3 Space Charge Effect

In ferroelectric thin films, oxygen vacancies migrate towards the interface under an ac field and it is the high concentration of vacancies in this region that results in ordering of the vacancies and pinning of domain walls. Auger data of Scott *et al.* revealed the existence of a space charge region in the lead zirconate titanate near the interface with the electrodes, where the oxygen concentration decreases sharply rather than maintains constant throughout the film [55]. Their results also showed that the oxygen concentration drops by about 50% of the value in the center of the film while still 20 nm from the Pt surface, as shown in Figure 2.6. The oxygen depletion creates an n-type region in the film, in contrast to the p-type PZT throughout the interior of the film. Moreover, they also demonstrated that the film that had been fatigued by 10^{10} cycles

shows an increase in the width of the space charge region. The interfacial nature of fatigue in thin films has also been demonstrated by Dimos *et al.* [56] and by Colla *et al.* [49]. First-principle calculations conducted by Poykko and Chadi [57] also indicated that this Schottky vacancy is not closely bound, and hence the oxygen vacancies are sufficiently mobile to migrate to the electrode interface, or form oxygen vacancy planes to pin the domain walls.

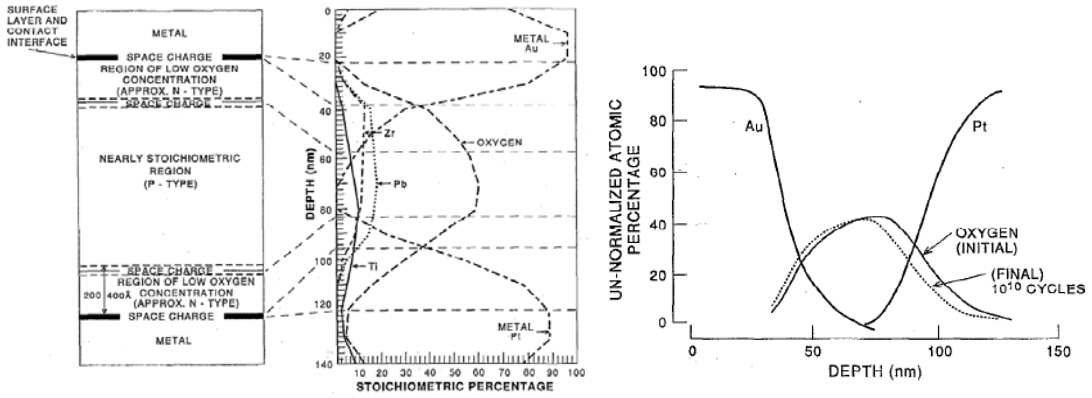

Figure 2.6: (a) Auger depth profile of PZT thin film capacitor, and (b) Effect of fatigue on oxygen concentration near the electrode.[55]

2.2.4 Electronic Suppression of Polarization

Miura and Tanaka calculated the electronic states of ferroelectric perovskite oxides, $PbTiO_3$, using the discrete variational Xα cluster method [17]. They found that the bond order of the π bonds between Ti 3*d* and O 2*p* as a function of titanium ion displacement in $PbTiO_3$ shows a maximum, suggesting that the magnitude of the ferroelectricity is related to the strength of the π bonds. Moreover, by calculating the bond order (Figure

2.7), they found that the π bonds between a titanium ion and oxygen ions are weakened by the remaining electrons of oxygen vacancies. Therefore, they proposed that the appearance of oxygen vacancies is one of the origins of fatigue in PZT.

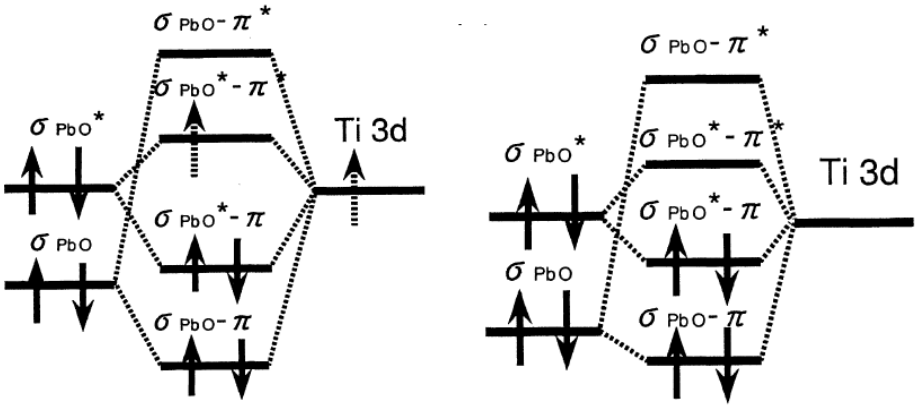

Figure 2.7: Energy diagrams between σ_{PbO}, σ^*_{PbO} states and a titanium *3d* orbital of $PbTiO_3$ (left), and when one electron occupies a titanium *3d* orbital (right) [17].

2.3 Degradation Improvement: Experimental Approaches

Approaches to improve the degradation behaviors of lead zirconate titanate have been intensively explored, and experiments have shown that the modification of electrodes and modification of the elemental substitution in PZT are two most successful ways.

2.3.1 Modification of Electrodes

To overcome the fatigue problem, researchers have tried modification of electrodes.

When oxide or hybrid-metal-oxide electrodes, such as $LaNiO_3$, $La_{0.5}Sr_{0.5}CoO_3$, RuO_2 and IrO_2, are used to replace the Pt electrode, the fatigue problem can be solved [19, 58-62]. The improved fatigue resistance can be explained by the fact that these electrodes can reduce or reoxidize reversibly and repeatedly without degradation [63]. However, this non-degrading reduction and oxidization process complicate the leakage-current properties of these electrodes, and generally films on the oxide or hybrid-metal-oxide electrodes have higher leakage currents than those with platinum electrodes. Lastly, these electrodes are more difficult to synthesize than pure Pt electrode resulting in an increase of production cost.

2.3.2 Modification of Elemental Substitution

Currently, the elemental substitution has been proven to be a very effective way to control the ferroelectric behavior of PZT. The types of substitutions can be divided into several subgroups according to whether they occupy the A site (Pb site) or B site (Ti/Zr site), as well as whether they are the donors or acceptors based on their chemical valences relative to the original ions. Generally, donors soften the ferroelectric properties of PZT. For example, they can enhance the elastic compliance coefficient, dielectric constants, bulk resistivity, and remnant polarization, as well as reduce the coercive field and improve the fatigue behavior of PZT. A great number of donors, including Nb^{5+}, Ta^{5+}, W^{6+},and Mo^{6+} as B-site donors, and Y^{3+}, La^{3+} and aliovalent rare-earth elements as A-site donors, have been investigated experimentally on donor-doped PZT thin films for

memory applications, and improved ferroelectric properties were reported for this group of dopants [20-26, 33-35, 64-67].

Doping with an acceptor usually hardens the ferroelectric properties of PZT. For example, acceptor doped thin films have lower dielectric constants, lower dielectric loss, higher coercive fields, higher mechanical quality factors, slightly lower coupling factors, and lower bulk resistivities. In contrast to the results on donor-substituted PZT, experiments on the acceptors substituted PZT thin films are relatively few; only Fe^{3+}, Mn^{3+}, Sb^{3+}, Al^{3+} as B-site acceptors are known to us [27-31, 36, 43, 68, 69]. Moreover, it is noteworthy that all the reports show optimal ferroelectric properties of acceptors-doped PZT thin films at certain diluted doping concentrations, which indicate that unique mechanisms contrary to the empirical perception exist in these thin films [27, 43].

2.4 Theoretical Studies of Perovskite Oxides

In parallel with advances in laboratory synthesis, we have witnessed a revolution in the atomic-scale theoretical understanding of ferroelectricity in perovskite oxides in the past decade through first-principles density functional theory (DFT) investigations. The pivotal result of a density functional theory calculation is the ground-state energy computed within the Born-Oppenheimer approximation from which we can directly predict the ground-state crystal structure, phonon dispersion relations, and elastic constants. The ideas and methodology of density functional theory are discussed in Chapter 3.

For the physics of ferroelectrics, the electric polarization and its derivatives, such as the Born effective charges and the dielectric and piezoelectric tensors, are as important as the structural energetics. Proper formulations have been set up in the first-principle methodologies. Expressions for derivatives of the polarization corresponding to physically measurable quantities were presented and applied in density functional perturbation theory calculations in the late 1980s [70]. A key conceptual advance was establishing the correct definition of the electric polarization as a bulk property through the Berry-phase formalism of King-Smith, Vanderbilt, and Resta [71, 72]. With this and the related Wannier function expression [73], the spontaneous polarization and its derivatives can be computed in a post-processing phase of a conventional total-energy calculation, greatly facilitating studies of polarization-related properties.

For perovskite oxides, the presence of oxygen and first-row transition metals significantly increases the computational demands of density-functional total energy calculations compared to those for typical semiconductors. Numerous first-principle methods for accurate representation of the electronic wave functions have been adopted in the calculations for perovskite oxides, e.g. linearized augmented plane wave (LAPW) [74] and fullpotential linearized augmented plane wave (FLAPW) [75], linear muffin-tin orbitals [76], norm-conserving [77] and ultrasoft pseudopotentials (USPP) [78, 79], and projector-augmented wavefunction (PAW) potentials [80, 81]. The effects of different choices for the approximate density functions have been examined; while most calculations were carried out with the local density approximation, the effects of the

generalized-gradient approximation (GGA) and weighted density approximation have been investigated for many systems, as well as the alternative use of the Hartree-Fock approach [82]. Furthermore, many commercial and academic packages are available to implement the first principle methodology, including VASP [83, 84] (with ultrasoft pseudopotentials and projector-augmented wave function potentials), ABINIT [85] (with norm-conserving pseudopotentials and projector-augmented wave function potentials), PWscf (with normconserving and ultrasoft pseudopotentials), SIESTA [86] (with norm-conserving pseudopotentials), WIEN2k [75] and CRYSTAL [87].

To predict ground-state crystal structures, the usual process is to minimize the total energy with respect to free structural parameters in a chosen space group, in a spirit similar to that of a Rietveld refinement in an experimental structural determination. The space group is usually implicitly specified by a starting guess for the structure. For efficient optimization, the calculation of forces on atoms and stresses on the unit cell is essential and is included now in every standard first-principles implementation following the formalism of Hellmann and Feynman (1939) [88] for the forces and Nielsen and Martin (1985) for stresses [89].

The accuracy of density-functional theory for predicting the ground-state structures of ferroelectrics was first investigated for the prototypical cases of $BaTiO_3$ and $PbTiO_3$ [90-92] and then extended to a larger class of ferroelectric perovskites [73]. Extensive studies of the structures of perovskite oxides and related ferroelectric-oxide structures have since been carried out [93]. The predictive power of first principles calculations is

well illustrated by the results of Singh for $PbZrO_3$ [94], in which the correct energy ordering between ferroelectric and antiferroelectric structures was obtained and, furthermore, comparisons of the total energy resolved an ambiguity in the reported space group and provided an accurate determination of the oxygen positions.

Minimization of the total energy can also be used to predict atomic arrangements and formation energies of point defects [54, 95-99], domain walls [13-15, 57], and nonstoichiometric planar defects, such as antiphase domain boundaries [100, 101] in perovskite oxides. The supercell used must accommodate the defect geometry and generally must contain many bulk primitive cells to minimize the interaction of a defect with its periodically repeated images. Thus, these calculations are extremely computationally intensive, and many important questions remain to be addressed.

While much of the essential physics of ferroelectrics arises from the structural energetics, the polarization, and the coupling between them, there has been increasing interest in ferroelectric oxides as electronic and optical materials, for which accurate calculations of the gap and dipole matrix elements are important. Furthermore, the band structures enter in an essential way in understanding the charge transfer and dipole layer formation of heterostructures involving ferroelectrics, other insulators, and metals. While density-functional theory provides a rigorous foundation only for the computation of Born-Oppenheimer ground-state total energies and electronic charge densities, it is also often used for investigation of electronic structure. In the vast majority of density functional implementations, calculation of the ground state total energy and charge

density involves the computation of a band structure for independent electron states in an effective potential, following the work of Kohn and Sham [102]. This band structure is generally regarded as a useful guide to the electronic structure of materials, including perovskite and layered perovskite oxides [90, 103]. It should be noted that with approximate functions, such as the local-density approximation, the fundamental band gaps of insulators and semiconductors, including perovskite ferroelectrics, are substantially under-estimated.

While for narrow gap materials the system may even be erroneously found to be metallic, for wider gap systems such as most of the simple ferroelectric perovskite compounds considered here, the band gap is still nonzero and thus the structural energetics in the vicinity of the ground-state structure is unaffected. While this error might be considered to be an insuperable stumbling block to first-principles investigation of electronic structure and related properties, there is no widely available, computationally tractable alternative. The truth is that these results can, with care, awareness of the possible limitations, and judicious use of experimental input, be used as extract useful information about the electronic structure and related properties in individual material systems.

2.5 Summary

In this chapter, the applications of lead zirconate titanate are first presented, which demonstrate the appealing potential of these materials in modern electronic devices, especially as non-volatile memory material.

However, the applicable PZT material suffers from long term degradation. The studies on the origins of these degradations are collected, and most studies relate the degradation to the oxygen vacancies. Three remarkable mechanisms are identified thereafter: domain pinning effect (oxygen vacancies pin the domain walls, and hence pin the polarization in a particular direction), space charge effect (oxygen vacancies migrate under an ac field and result in a high concentration of vacancies at the interface), and electronic suppression of polarization (π bonds between a titanium ion and oxygen ions are weakened by remaining electrons of oxygen vacancies).

Two experimental approaches (electrode modification and elemental substitution) to improve the degradation behaviors are described. Both experimental and theoretical studies by these two approaches are collected.

All these remarkable studies conducted by the previous researchers inspire the ideas of our study, and more importantly, lay the foundation for our study. In this work, we extend the investigation from the pure lead zirconate titanate to their substituted derivatives. By conducting theoretical studies before experimental synthesis, we predict

the effect of substitution of individual element, as well as understand the mechanisms behind the substitution. This appealing methodology is applied to systematically study the substituted lead zirconate titanate for the first time.

Chapter III

Density Functional Theory

First-principle density functional theory (DFT) calculations have been recognized as a powerful tool for condensed matter studies. In this chapter, a brief introduction of DFT is presented. First of all, the fundamental theorems of DFT, which help to calculate the ground state energy, are described. Two schemes for the exchange-correlation functionals, local density approximation (LDA) and generalized gradient approximation (GGA), are introduced. Other density functional theory methodologies, such as plane-wave basis set, pseudopotential, and k point sampling, are also presented.

3.1 First Principles of Quantum Theory

Today, the advanced quantum mechanical software and the rapid increase in the computing hard ware speed have allowed large-scale and high quality simulations. “First principles”, or “*ab initio*”, methods have been widely used in the fields of materials science, electronics, mechanical engineering and bioscience, as well as physics and chemistry. Contrary to a classical force field which uses empirical results averaged over a large number of molecules, the principal idea of the first-principle methodology is to regard the many-atom system as a many-body system composed of the electrons and nuclei, and to treat everything on the basis of the first principles of quantum mechanics without introducing empirical parameters. Therefore, first-principle calculations can elucidate many important questions in chemistry, physics and materials science, which can not be addressed through experiment, e.g. the properties that are derived only from the potential energy surface, and the properties depending directly on the electron density distribution.

In quantum chemistry, a system is described by a wavefunction which can be determined by solving the Schrodinger equation:

$$\hat{H}\Psi = E\Psi . \qquad (3\text{-}1)$$

In this equation, $\hat{H}$ is the Hamiltonian operator which gives the kinetic and potential energies of a system of atomic nuclei and electrons. Ψ is a wavefunction, one of the solutions of the eigenvalue equation. E is the energy of the system. This wavefunction depends on the coordinates of the electrons and nuclei. The Hamiltonian $\hat{H}$ is

composed of several parts: kinetic energy of the nuclei (T_N), kinetic energy of the electron (T_e), and Coulomb interaction within or between nuclei and electrons ($V_{ee}(r)$, $V_{NN}(R)$, $V_{Ne}(r,R)$), written as follows:

$$\hat{H} = T_N + T_e + V_{ee}(r) + V_{NN}(R) + V_{Ne}(r,R) \quad . \tag{3-2}$$

To be more detailed, the Hamiltonian operator can be written as:

$$H = \sum_{I=1}^{N} \frac{P_I^2}{2M_I} + \sum_{i=1}^{n} \frac{P_i^2}{2m_i} + \sum_{i>j} \frac{e^2}{|r_i - r_j|} + \sum_{I>J} \frac{Z_I Z_J e^2}{|R_I - R_J|} - \sum_{i,I} \frac{Z_I e^2}{|R_I - r_i|} \quad , \tag{3-3}$$

where P_I and P_i denote the momenta of ions and electrons, r and R denote the coordinates of electrons and ions, Z and e the charges of the ions and electrons, m and M their masses.

Equation (3-3) is a very complex differential equation. In order to make the equation computationally tractable, especially in a system that has many-particles, several approximations are made, and these approximations do not affect the descriptions of the system in most cases. Here are the major approximations made in quantum chemistry:

1. Time independence: The states of electrons are stationary in time.
2. Neglect of relativistic effects: This can be warranted unless the velocity of the electrons approaches the speed of light, which is the case only in heavy atoms with very high nuclear charge.
3. Born-Oppenheimer approximation: Electrons can move so as to follow very quickly the motion of nuclei, thus the electrons are always in a steady state.

4. Orbital approximation: The total wavefunction of a quantum system is approximated by the Slater determinants of one electron orbital.

In the approximations above, the Born-Oppenheimer approximation decouples the dynamics of ions from that of the electrons. Therefore, the total wavefunction of a system is a product of the wavefunction of ions $\chi(R)$ and the wavefunction of electrons $\Phi(x, R)$:

$$\psi(x, R) = \Phi(x, R)\,\chi(R) \quad . \tag{3-4}$$

The electronic wavefunction $\Phi(x, R)$ can be obtained by solving the electronic Schrodinger equation:

$$\left[T_e + V_{ee}(r) + V_{Ne}(r, R)\right]\Phi(x, R) = \varepsilon_n(R)\Phi(x, R) \quad . \tag{3-5}$$

This equation contains the ion position as well as the electronic positions, but it depends parametrically on the ion positions; ions positions are not variables in this equation. The electronic Hamiltonian contains three terms: kinetic energy, electrostatic interaction between electrons and nuclei, and electrostatic repulsion between electrons. The detailed Schrodinger equation for electronics can be written as:

$$H_e = -\frac{1}{2}\sum_{i=1}^{n}\nabla_i^2 - \sum_{i=t}^{n}\sum_{A=2}^{N}\frac{Z_A}{|R_A - r_i|} + \sum_{i<j}^{n}\frac{1}{r_{i,j}} \quad . \tag{3-6}$$

The symbol ∇ is a Laplace operator, where $\nabla_i^2 = \frac{\partial^2}{\partial x_i^2} + \frac{\partial^2}{\partial y_i^2} - \frac{\partial^2}{\partial z_i^2}$. The total energy in the Born-Oppenheimer model is obtained by adding the nuclear repulsion energy in the electronic energy:

$$E_{Total} = E_e(R) + V_{NN}(R) \quad . \tag{3-7}$$

According to the Born-Oppenheimer adiabatic approximation, ions move on the potential-energy surface of the electronic ground state only. Thus the total energy defines a potential energy hypersurface E which can be used to solve a Schrodinger equation for the nuclear motion subsequently:

$$\left[T_N + V_{NN}(R) + \varepsilon(R)\right]\chi(R) = E\,\chi(R) \quad , \tag{3-8}$$

where $\chi(R)$ is the wavefunction of the ions. Schrodinger equation is associated with the stationary states of the system and their energies to the Hamiltonian operator, which can be viewed as the recipe to obtain the energy associated with a wavefunction describing the positions of the nuclei and electrons in the system.

3.2 Density Functional Theory

While many methods were developed to accurately solve the Schrodinger equation of the complex many-body systems, density functional theory (DFT) has been recognized as one of the most successful approaches. Density functional theory emerged in the early days of quantum mechanics and the solid foundations of the DFT were established in the 1960s with the classic papers of Hohenberg and Kohn [104], and Kohn and Sham [102].

Thereafter, remarkable progress in the theory formalism and basic principles of DFT has been witnessed. However, it still took many years for the advantages of DFT to be taken, before the modern super-computers made large-scale calculations affordable [39]. The 1998 Nobel Prize was awarded to Walter Kohn "for his development of the density-functional theory" [102] and to John Pople "for his development of computational methods in quantum chemistry" [105].

3.2.1 The Hohenberg-Kohn Theorems

Modern DFT originates from Hohenberg-Kohn theorems [104], which relate to any system consisting of electrons moving under the influence of an external potential $v_{ext}(\mathrm{r})$. It states that the external potential $v_{ext}(\mathrm{r})$, and hence the total energy, is a unique functional of the electron density $\rho(r)$. The energy functional $E[\rho(r)]$ can be written in terms of the external potential $v_{ext}(\mathrm{r})$ in the following way:

$$E[\rho(r)] = \int \rho(r) v_{ext}(r) dr + F[\rho(r)] \quad , \tag{3-9}$$

where F[ρ(r)] is a universal functional of the electron density ρ(r) only. Correspondingly, a Hamiltonian for the system can be written such that the electron wavefunction Ψ minimizes the expectation value gives the groundstate energy (assuming a non-degenerate groundstate),

$$E[\rho(r)] = \left\langle \Psi \middle| \hat{\mathrm{H}} \middle| \Psi \right\rangle \quad . \tag{3-10}$$

The Hamiltonian can be written as,

$$\hat{\mathrm{H}} = \hat{F} + \hat{V}_{ext} \quad , \tag{3-11}$$

where $\hat{F}$ is the electronic Hamiltonian consisting of a kinetic energy operator $\hat{\mathrm{T}}$ and an interaction operator $\hat{V}_{ee}$,

$$\hat{F} = \hat{T} + \hat{V}_{ee} \quad . \tag{3-12}$$

The electron operator $\hat{F}$ is the same for all N-electron systems, so $\hat{\mathrm{H}}$ is completely defined by the electron number N, and the external potential $v_{ext}(\mathrm{r})$.

Furthermore, Hohenberg-Kohn theorems state that the ground state energy can be obtained variationally: the density that minimizes the total energy is the exact ground state density.

3.2.2 Kohn-Sham Scheme

Kohn and Sham introduced a formalism that laid the foundation for the application of DFT methods in computational chemistry [102]. The Kohn-Sham formulation centers on mapping the full interacting system with the real potential, onto a fictitious non-interacting system. Therefore the electrons move within an effective ``Kohn-Sham'' single-particle potential $v_{ks}(\mathrm{r})$. The Kohn-Sham method greatly facilitates the calculation, yet still exactly yields the same ground state density as the real system.

As presented in the Hohenberg-Kohn theorem, the ground state energy of a many-electron system can be obtained by minimizing the energy functional, subject to the constraint that the electron number N is conserved, which leads to:

$$\delta\left[\mathrm{F[n(r)]}+\int \mathrm{v_{ext}(r)n(r)dr}-\mu(\int \mathrm{n(r)dr}-\mathrm{N})\right]=0 \quad , \tag{3-13}$$

and the corresponding Euler equation is given by,

$$\mu=\frac{\delta F[n(r)]}{\delta n(r)}+v_{ext}(r) \quad , \tag{3-14}$$

where μ is a Lagrange multiplier associated with the constraint of constant N. Kohn and Sham set up a system where the kinetic energy could be determined exactly. This was achieved by invoking a non-interacting system of electrons. The corresponding ground state wavefunction Ψ_{ks} for this type of system is given exactly by a determinant of single-particle orbitals $\psi_i(r_i)$,

$$\Psi_{ks}=\frac{1}{\sqrt{N!}}\det[\psi_1(r_1)\psi_2(r_2).....\psi_N(r_N)] \quad . \tag{3-15}$$

The universal functional $F[\rho(r)]$ was then partitioned into three terms:

$$F[\rho]=T^S[\rho]+E^H[\rho]+E^{EC}[\rho] \quad . \tag{3-16}$$

$\mathrm{T^S[\rho]}$ is the kinetic energy of a non-interacting electron gas of density ρ, $\mathrm{E^H[\rho]}$ the classical electrostatic energy of the electrons(Hatree energy),

$$E^H[\rho]=\frac{1}{2}\iint\frac{\rho(r)\rho(r')}{|r-r'|}drdr' \quad , \tag{3-17}$$

and $E^{EC}[\rho]$ the exchange-correlation energy, which contains the difference between the exact and non-interacting kinetic energies and also the non-classical contribution to the electron-electron interactions. In the Kohn-Sham prescription, the Euler equation given in (3.14) now becomes:

$$\mu = \frac{\delta F[\rho]}{\delta \rho} + v_{ks}(r) \quad , \tag{3-18}$$

where the Kohn-Sham potential $v_{ks}(\mathrm{r})$ is given by:

$$v_{ks}(\mathrm{r}) = v_{ext}(r) + v_H(r) + v_{XC}(r) \quad , \tag{3-19}$$

with the Hartree potential $v_H(r)$ given by

$$v_H(r) = \frac{\delta E_H[\rho]}{\delta \rho} = \int \frac{\rho(r')}{|r - r'|} dr' \quad , \tag{3-20}$$

and the exchange-correlation potential $v_{XC}(r)$ given by,

$$v_{XC}(r) = \frac{\delta E_{XC}[\rho(r)]}{\delta \rho(r)} \quad . \tag{3-21}$$

The crucial point to understand Kohn-Sham theory is to know that the density obtained when solving the alternative non-interacting Kohn-Sham system is the same as the exact ground state density. The ground state density is obtained in practice by solving the N one-electron Schrödinger equations,

$$[-\frac{1}{2}\nabla^2 + v_{ks}(r)]\psi_i(r) = \varepsilon_i \psi_i(r) \quad , \tag{3—22}$$

where ε_i are Lagrange multipliers corresponding to the orthonormality of the N single-particle states $\psi_i(r)$, and the density is constructed from,

$$\rho(r) = \sum_{i=1}^{N} |\psi_i(r)|^2 \quad . \qquad (3-23)$$

The non-interacting kinetic energy $T^s[\rho(r)]$ is therefore given by,

$$T^s[\rho(r)] = -\frac{1}{2}\sum_{i=1}^{N}\int \psi_i^*(r)\nabla^2\psi_i(r)dr \, . \qquad (3-24)$$

In order to handle the kinetic energy in an exact manner, N equations have to be solved in the Kohn-Sham theory to obtain one set of Lagrange multipliers $\{\varepsilon_i\}$. However, an advantage of the Kohn-Sham method is that as more electrons are added to the system, i.e. studying a system with more atoms, the problem becomes only more difficult because there are more single-particle equations to be solved.

Although exact in principle, Kohn-Sham theory is approximate in practice because the exact exchange-correlation functional, $E^{EC}[\rho]$, has not been identified. The intention of Kohn and Sham was to make the unknown contribution to the total energy of the non-interacting system as small as possible, and this is indeed the case with the exchange-correlation energy; however, it is still an important contribution since the binding energy of many systems is about the same magnitude as $E^{EC}[\rho]$, so an accurate description of exchange and correlation is crucial for the prediction of binding properties.

3.2.3 Exchange-Correlation Functional

Two approximation schemes are popular to describe the exchange-correlation energy. One is local density approximation (LDA), which approximates the functionals $T[\rho]$ and $E^{EC}[\rho]$ by the corresponding energies of a homogeneous electron gas of the same local density, where the density varies slowly in space. In LDA, $E_{XC-LDA}[\rho]$ can be written as:

$$E_{XC-LDA}[\rho(r)] = \int \rho(r)\varepsilon_{XC}(\rho(r))dr \quad , \tag{3-25}$$

where $E_{XC-LDA}[\rho] = E_{X-LDA}[\rho] + E_{C-LDA}[\rho]$ represents the exchange-correlation energy per electron of a uniform electron gas. The exchange part is commonly expressed by simple Slater-Dirac exchange. As to the correlation part, several groups have offered their solutions to the correlation energy expression, such as Vosko, Wilk, and Nusair [106], as well as Perdew and Zunger [107]. These LDA exchange-correlation functions may be supplemented with relativistic corrections to the exchange part, as given by MacDonald and Vosko [108].

The other scheme is generalized gradient approximation (GGA), which puts the density gradient into consideration as well as the local density, since the density is more generally a non-uniform electron gas. GGA is currently the most popular exchange-correlation formalism in condensed matter physics. GGA can be conveniently written in terms of an analytic function known as the enhancement factor, $F_{XC}[\rho(r),\nabla\rho(r)]$, that directly modifies the LDA energy density,

$$E_{XC-GGA}[\rho(r)] = \int \rho(r)\varepsilon_{XC}(\rho(r))F_{XC}[\rho(r),\nabla\rho(r)]dr \tag{3-26}$$

Moreover, the gradient corrections are split into separate exchange and correlation contributions. A number of gradient corrected functional forms were developed for both contributions. The exchange functionals include PW86 (Perdew and Wang) [109], and PBE (Perdew, Burke, and Ernzerhof) [110]. The GGA correlation functionals include LYP (Lee, Yang, and Parr) [111], and PW91(Perdew and Wang) [112].

3.3 Bloch's Theorem and Plane-Wave Basis Set

Bloch's theorem [113] states that the wavefunction of an electron $\psi_{j,k}$, within a periodic potential, can be written as the product of a lattice periodic part $u_j(r)$ and a wavelike part $e^{ik\cdot r}$,

$$\psi_{j,k} = u_j(r)e^{ik\cdot r} \quad , \tag{3-27}$$

where the subscript j indicates the band index and k is a continuous wavevector that is confined to the first Brillouin zone of the reciprocal lattice. Since $u_j(r)$ has the same periodicity as the direct lattice, it can be expressed in terms of a discrete plane-wave basis set with wavevectors **G** that are reciprocal lattice vectors of the crystal, i.e.

$$u_j(r) = \sum_G c_{j,G} e^{iG\cdot r} \quad . \tag{3-28}$$

Where $G \cdot R = 2\pi m$, where m is an integer, R are the crystal lattice vectors and $c_{j,G}$ the plane-wave coefficients. The above results show that the electron wavefunctions can be expanded in terms of a linear combination of plane-waves,

$$\psi_{j,k}(r) = \sum_{G} c_{j,k} + Ge^{i(k+G)\cdot r} \quad . \tag{3-29}$$

Plane-waves are a simple way of representing electron wavefunctions. They offer a complete basis set that is independent of the type of crystal, which treats all areas of space equally. This is in contrast to some other basis sets which use localized functions such as Gaussians which are dependent on the positions of the ions.

Using a plane-wave basis set to expand the electronic wavefunctions in periodic systems leads to a particularly simple formulation of the Kohn-Sham equations in DFT. Accounting for the fact that the various contributions to the local potential in the Kohn-Sham equation can be written in the form,

$$v(r) = \sum_{G} \overline{v}(G) e^{iG\cdot r} \quad , \tag{3-30}$$

where $\overline{v}(G)$ represents the Fourier transform of the corresponding real-space quantity, and substituting the plane-wave solutions into (Eq. 3-21), leads to a reciprocal-space representation of the Kohn-Sham equations，where the kinetic energy is diagonal, and the remaining three terms on the left-hand-side are the Fourier components of the external, Hartree and exchange-correlation potentials respectively. The $G = 0$ component of the Hartree and external potentials diverge due to the long-range nature of the Coulomb interaction, however the divergences cancel to give a constant value that is ill-defined. However, the value of this constant can be set arbitrarily and does not affect the physical properties of a system.

For an exact calculation, the dimension of the plane-wave basis set should be infinite. Fortunately the plane-waves at the lower end of the kinetic energy range are most important, so a practical solution of Eq. 3.31 can be obtained by truncating the basis set to a finite number of plane-waves. This is defined by the kinetic cutoff energy E_{cut},

$$\frac{1}{2}|k+G|^2 \le E_{cut} \qquad (3.31)$$

This leads to another advantage of the plane-wave basis set in that the accuracy can be systematically improved by increasing E_{cut} - a feature that is not always shared by localized basis sets. The main disadvantage of plane waves is that they are not efficient at describing wavefunctions with large curvature such as the core regions of atoms, consequently such regions of space require an unreasonably large number of planes to be sufficiently accurate, and so would dominate the convergence of E_{cut}. This problem has been overcome by the pseudopotential approximation.

3.4 Pseudopotentials

In order to improve the calculation efficiency, the pseudopotential approximation is adopted in many *ab-initio* calculations. In pseudopotential approximations, the core electrons are frozen to the nucleus and the valence electrons are optimized. The total external potential of the original reference all-electron atom is replaced by a smooth, non-singular potential known as the pseudopotential which only acts on the valence electrons. In the core region, pseudopotential may not represent the real potential, which

is acceptable so long as the atomic cores interact weakly with neighboring atoms and are not sensitive to their environment. This only results in a reduction of the total energy. Actually, only the rearrangement of the valence electrons is meaningful in pseudopotential calculations; outside the core region, the pseudopotential is identical to the corresponding all-electron AE potential and orbitals.

There are two widely-used types of pseudopotentials. One is a norm-conserving pseudopotential, in which a pseudo-wavefunction description of the system is constructed so as to be equal to the actual valence wavefunction beyond some defined core radius r, but different from the actual core wavefunction inside r, while retaining an identical norm (i.e. net charge density within the sphere of radius r). The motivation behind this approach is three fold:

1. To have a soft pseudopotential (i.e. use relatively few plane waves in the expansion of the valence pseudo-wavefunction)
2. To insure that a pseudopotential generated for a given atomic configuration is transferable to other atomic configurations
3. To have a pseudo-charge density that accurately reproduces the valence charge density

The pseudopotential generated in this approach is called semi-core, since it depends on the angular momenta l as follows:

$$V^{ps} = V^{LOC}(r) + \sum_{l=0}^{l_{\max}} V_1^{ps} \hat{P}_1 ,$$

where V^{LOC} represents the local potential, l_{max} typically 1 or 2, the V_l^{PS} the non-local component of the pseudopotential, and an angular momentum projector.

Vanderbilt removed the norm-conservation criterion of the pseudopotential, so that the pseudo-wavefunctions inside r could be made as soft as possible (ultrasoft) [79]. His approach greatly reduces the plane wave cutoff threshold (and thus the size of the plane wave expansion), but introduces some complications:

1. The pseudo-wavefunction is no longer normalized inside r, thus introducing a nontrivial overlap in the secular equation.
2. The pseudo-charge density is no longer obtained as in the norm conserving approach, so a term of the following form must be added in the core region:

$$\rho(\mathrm{r}) = \sum_{\mathrm{OCC}} \left[\Phi^*(\mathrm{r})\Phi(\mathrm{r}) + \sum_{\mathrm{nm}} \mathrm{Q}_{\mathrm{nm}} \langle \Phi_{\mathrm{j}} \mid \beta_{\mathrm{n}} \rangle \langle \beta_{\mathrm{m}} \mid \Phi_{\mathrm{j}} \rangle \right].$$

Given the complication of generating a pseudopotential in the ultrasoft formalism, this approach is best used in a large calculation where the generation of the pseudopotential in negligible compares to the cost of the calculation.

Ultrasoft pseudopotentials (USPP) have another advantage besides being much softer than norm-conserving potentials. The USPP generation algorithm guarantees good scattering properties over a pre-specified energy range, which results in much better transferability and accuracy of pseudopotential.

Blochl has further developed the US-PP concept by combining ideas from pseudopotential and LAPW (linearized augmented-plane-wave) methods in a conceptually elegant framework, called the projector augmented-wave method (PAW) [81]. Furthermore, G. Kresse and D. Joubert derived the formal relationship between ultrasoft Vanderbilt-type pseudopotentials and Blochl's projector-augmented wave method [80]. It was shown that the total energy functional for US pseudopotentials can be obtained by linearization of two terms in a slightly modified PAW total energy functional. Generally the PAW potentials are more accurate than the ultra-soft pseudopotentials. There are two reasons for this: first, the radial cutoffs (core radii) are smaller than the radii used for the US pseudopotentials, and second the PAW potentials reconstruct the exact valence wave function with all nodes in the core region. Since the core radii of the PAW potentials are smaller, the required energy cutoffs and basis sets are also somewhat larger. If such a high precession is not required, the older US-PP can be used. In practice, however, the increase in the basis set size will be anyway small, since the energy cutoffs have not changed appreciably for C, N and O, so that calculations for models, which include any of these elements, are not more expensive with PAW than with US-PP.

Given the approximated exchange-correlation potential and pseudopotential, the Kohn-Sham Hamiltonian, is well defined except for boundary conditions on the Hatree potential and explicit external potential $V_{ext}(r)$. To solve the Kohn-Sham equations numerically, one must employ a set of basis functions in order to efficiently represent the electronic wavefunction. Several factors determine the choice of basis set including ease of implementation, accuracy, speed, and geometry of the system. In general, one chooses

between a plane-wave or related basis localized in k-space, or a basis that is localized in real space.

3.5 *k*-point Sampling

Electronic states are allowed only at a set of *k* points determined by the boundary conditions that apply to the bulk solid. Bloch's theorem transforms the electronic structure problem from one of the calculating an infinite number of electronic states (for an infinite periodic system) to one of calculating for a finite number of bands at an infinite number of k points within the Brillouin zone of the system. K points are the set of special points in the irreducible Brillouin which provides an efficient means of integrating periodic functions of the wave vector. The integration can be over the entire Brillouin zone or over specified portions. There are some different schemes to generate k point sets to optimize the calculation, including ones by Monkhorst and Pack [114], Lehmann and Taut [115].

3.6 Summary

In this chapter, the theoretical background of this study is briefly introduced. Instead of examining each electron in the system directly, Schrodinger equation is solved through considering the electron density based on Hohenberg and Kohn Theorem. This strategy greatly reduces the number of variables and thus the calculation cost. However, DFT was not applicable until the birth of Kohn-Sham equation because the functional

between density and the ground state energy, especially the kinetic energy, was not clear. Kohn-Sham equation estimates the kinetic energy with a good approximation and absorbs the presumably small non-classical correction into exchange-correlation potential is still elusive, different approaches towards it have been proposed, like the LDA and the GGA.

Pseudopotential is a smooth, non-singular potential replacing the total external potential of the reference. It only acts on the valence electrons. To solve the Kohn-Sham equations numerically, a set of basis functions must be employed in order to efficiently represent the electronic wave functions. In principle, an infinite plane-wave basis set is required to expand the electronic wave functions. However, plane-waves with larger kinetic energy are less important. With a cutoff energy, plane-wave basis set can be reduced to finite according to requirement on calculation accuracy. With a basis set and pseudopotentials, we also need to compute the periodic functions at a carefully selected set of points in reciprocal space which can be then reduced by symmetry operations/Bloch's theorem to a few points for efficient calculation, cutoff energy and the k point sampling are two crucial parameters in the first principle calculations.

Chapter IV

Pure Lead Zirconate Titanate

Lead titanate ($PbTiO_3$) is studied using *ab initio* density functional theory calculations to investigate its origin of ferroelectricity by examining the crystal structure and electronic structure. Furthermore, we extend our research into a more complex perovskite oxide lead zirconate titanate ($PbTi_{0.5}Zr_{0.5}O_3$), a more interesting material for practical ferroelectric devices. The preliminary calculations in this chapter are vital for the following studies on the more complex crystal structures, such as lead zirconate titanate and their doped derivatives.

4.1 Introduction

Lead zirconate titanate is one of the most important ferroelectric materials characterized by a switchable macroscopic polarization. However, the origin of its ferroelectric behavior was unclear for a long time. There was incomplete understanding of why similar, but chemically different, perovskites should display very different ferroelectric behaviors. Later it is recognized that the great sensitivity of ferroelectrics to chemistry, defects, electrical boundary conditions and pressure arises from a delicate balance between long-range Coulomb forces (which favor the ferroelectric state) and short-range repulsions (which favor the non-polar cubic structure). Theoretical studies, particularly first-principle density functional theory calculation has played an important role in identifying the origin of ferroelectricity in perovskite oxides. Here, we report the results of our DFT calculations on two ferroelectric perovskites, $PbTiO_3$ and $Pb(Zr_{0.5}Ti_{0.5})O_3$, and demonstrate that the hybridization between the titanium 3*d* states and the oxygen 2*p* states is essential for ferroelectricity.

4.2 Origin of Ferroelectricity in $PbTiO_3$

4.2.1 Computational Methodology

The optimization on the crystal and electronic structures of lead titanate is performed with the generalized gradient approximation (GGA) and the local density approximation (LDA), respectively, within density functional theory (DFT), using the

projector-augmented wave (PAW) method for both GGA and LDA. Furthermore, the Perdew-Burke-Ernzerhof (PBE) / Ceperly-Alder (CA) exchange-correlation parameterization is employed for the GGA/LDA calculation. The pseudopotential approach is used, where Pb *5d*, *6s*, *6p*, Ti *3d*, *4s*, and O *2s*, *2p* orbitals are treated as the valence orbitals. One unit cell is used for this calculation, as shown in Figure 4.1, and the structural optimization was determined within *P4mm* symmetry for ferroelectric phase. To reveal the ferroelectric effects on the crystal and electronic structures, a centrosymmetric cell is used, which exhibits an inversion symmetry about the central Pb atom.

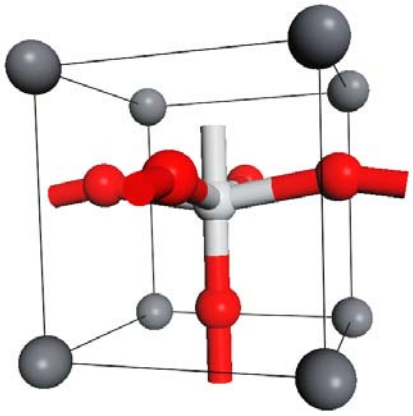

Figure 4.1: Unit cell of lead titanate, where grey spheres denote lead atom, and red /white spheres are oxygen atoms and titanium atoms.

4.2.2 Prediction of Ground State

To ensure the validity of the calculations, convergence tests for the cutoff energy and the k mesh size are performed before any geometry relaxation and property calculation throughout our studies. The convergence test results for $PbTiO_3$ unit cell is shown in Fig.

4.2, from which it is safe to conclude that the cutoff energy be set at 700 eV, and the special-point method applied for the Brillouin zone sampling (k mesh) be set at 8×8×8 Monkhorst Pack mesh.

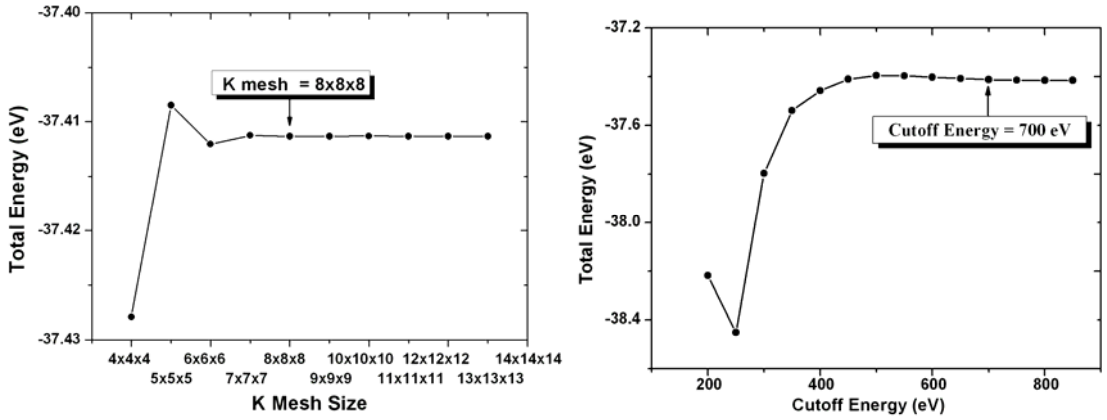

(a) (b)

Figure 4.2: Convergence test results on (a) the k mesh size in the Brillouin zone and (b) the cutoff energy using GGA.

The general method to predict the ground state of a crystalline system is to combine fixed-volume geometry relaxations and equation-of-state (EOS) fitting. First of all, a series of geometry relaxations have been conducted where the volume of the cell is fixed for 30 sets of different values. After this, the energies of the relaxed cells are fitted to the EOS to find the ground state lattice constants. Normally, this is a reliable and robust way to find out the ground state of any system which structure information is unknown.

However, in the study of perovskite structure materials, this method seems incompatible. We have implemented both GGA and LDA methods to test its validity. In

each method, the perovskite structures were tested with 30 sets of volumes and their cell shapes and ionic positions were fully relaxed under each fixed volume. The results are shown in Fig. 4.3. The optimized volume for GGA is $70.81\times10^{-30}m^3$, and for LDA, it is $60.51\times10^{-30}m^3$. As compared to the experiment value of 63.28×10^{-30} m^3, they are either overestimated (about 9%) or underestimated (about 5%). We also calculate the lattice parameters of the calculated ground states. GGA also shows a large overestimation of the c/a ratio (17.22%), while LDA underestimates the ratio (-2.63%) (Table 4.1).

Therefore it is important to note that there seems to be limitations of density functional theory calculations on the accuracy to which structural parameters, particularly lattice constants, can be obtained. Most obvious is the underestimation of the lattice constants within the local-density approximation, typically by about 1% (generalized-gradient approximation tends to shift lattice constants upward, sometimes substantially overcorrecting). Considering that the calculation involves no empirical input whatsoever, an error as small as 1% could be not regarded as a failure, but as a success of the method. Moreover, the fact that the underestimate varies little from compound to compound means that the relative lattice constants and thus the type of lattice mismatch (tensile/compressive) between two materials in a heterostructure is generally correctly reproduced by using computed lattice parameters. However, for certain questions, even a 1% underestimate can be problematic. The ferroelectric instability in the perovskite oxides, in particular, is known to be very sensitive to pressure [116] and thus to the lattice constant, so that 1% can have a significant effect on the ferroelectric instability. A great number of researchers have confirmed that small variations of the lattice parameter have

tremendous effects on the magnitude of ferroelectric instability of the perovskite oxides, such as $BaTiO_3$ and $PbTiO_3$ [73, 117-120]. For instance, in $BaTiO_3$, a reduction in the lattice parameter by 2% completely washes out the ferroelectric instability [121]. In addition, full optimization of all structural parameters in a low-symmetry space group can in some cases, $PbTiO_3$ being the most well-studied example, lead to an apparently spurious prediction, though fixing the lattice constants to their experimental values leads to good agreement for the other structural parameters [119]. Thus it has become acceptable, at least in certain first-principle contexts, to fix the lattice parameters or at least the volume of the unit cell, to the experimental value when this value is known. Therefore, we always obey this rule throughout our studies; even though this is an unsatisfactory retreat from pure *ab initio* approaches, where no experimental data should actually be used.

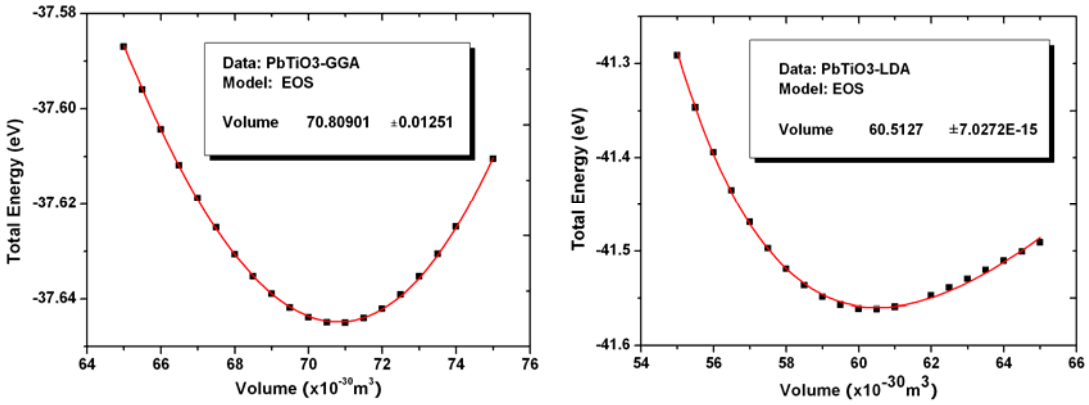

(a) (b)

Figure 4.3: EOS fitting of $PbTiO_3$ model within (a) GGA and (b) LDA. The data are obtained through a static calculation after a geometry optimization with the cell size fixed on a series of selective cell sizes.

Table 4.1.: Calculated Lattice Parameters via Different Schemes

	Experiment [122]	Fixed Volume	EOS(GGA)	EOS(LDA)
a	3.904	3.912 (0.21%)	3.845 (-1.52%)	3.881 (-0.60%)
c	4.152	4.131 (-0.50%)	4.791 (15.38%)	4.018 (-3.22%)
c/a	1.063	1.056 (-0.66%)	1.246 (17.22%)	1.035 (-2.63%)

4.2.3 Crystal Structures

The ground state ionic positions of the ferroelectric phase cell were determined by volume-fixed geometry relaxation with GGA-PBE calculations. The comparison of ion positions with other results from literatures and experiment observations is listed in the Table 4.2.

Table 4.2: Comparison of ion positions of $PbTiO_3$ (Fractional coordinates)

	X	Y	Z (GGA-PBE)	Z (Reference [118])	Z (Experiment [122])
Pb	0.000	0.000	0.000	0.000	0.000
Ti	0.500	0.500	0.536 (-0.36%)	0.547 (1.62%)	0.538
O_1	0.500	0.500	0.117 (-0.38%)	0.121 (3.67%)	0.117
O_2	0.000	0.500	0.612 (-0.03%)	0.627 (2.46%)	0.612
O_3	0.500	0.000	0.612 (-0.03%)	0.627 (2.46%)	0.612

The crystal structures of centro-symmetric and ferroelectric phases are shown in Fig. 4.4. A comparison of ferroelectric and centro-symmetric structures leads to following observation: (1) O_2, and O_3 at the O-Ti plane move significantly upwards to the upper Pb-O_1 plane; (2) Ti also moves upwards but only slightly;(3) O_1 below the Pb-O plane move upwards, but not as much as the O_2 and O_3. These tremendous ion motions contribute to bonds length change--lengthened O_2-Ti/O_3-Ti bonds and shortened O_1-Ti bond. Particularly, the atomic relaxation yields to two different O_1-Ti bonds in the (001) direction: a very long (2.40 Å) and a very short bond (1.73 Å).

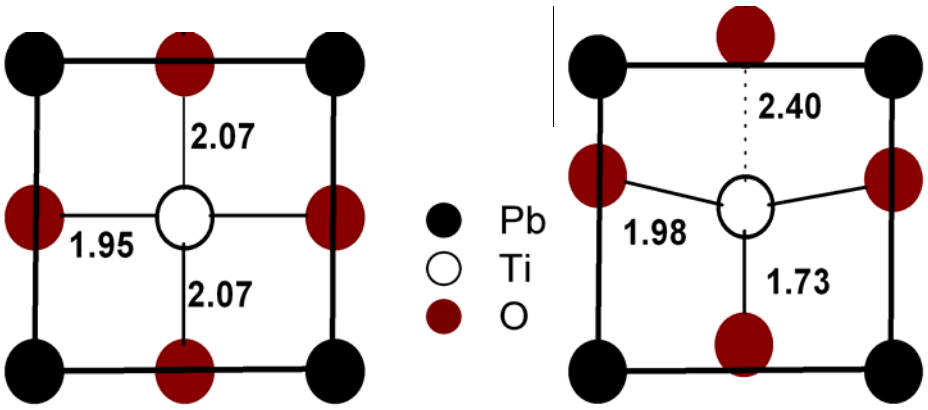

Figure 4.4: The groundstate unit cell structure of $PbTiO_3$: (a) centro-symmetric phase and, (b) ferroelectric phase.

4.2.4 Electronic Structures

Together with significant movement of ions, major changes in the electron structures also take place. The electron density distributions in both the ferroelectric phase and centro-symmetric phase are compared (Figure 4.5). It indicates that ferroelectricity in

$PbTiO_3$ leads to (1) a chemical weakening of some Ti-O_1 bonds in the (001) direction, and (2) a stronger covalence between Ti and O_1 at the other side, which is the cause of the short bond of 1.73 Å.

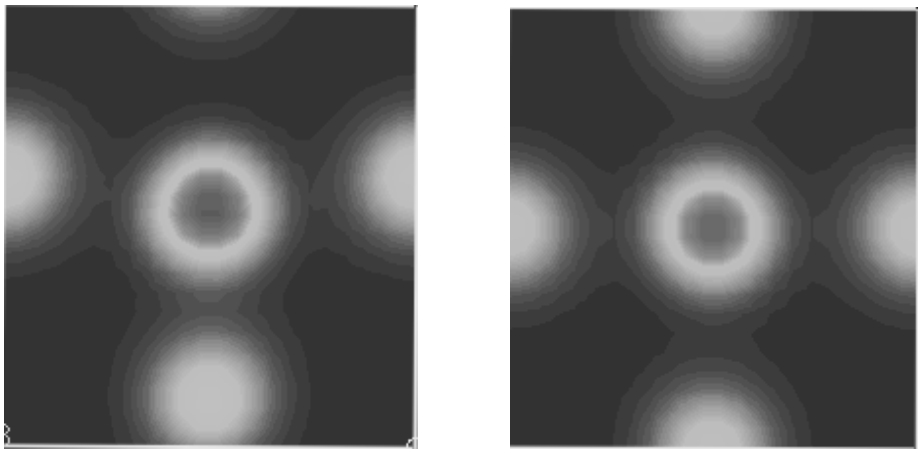

Figure 4.5: (a) Electron density plotted in the Ti-O plane (100) for ferroelectric unit cell. (b) Electron density plotted in the Ti-O plane (100) for ideal perovskite unit cell. Ti^{4+} anion is in the centre, the rest are O^{2-} cations.

Besides, the density of states (DOS) and partial density of states (PDOS) are calculated in order to reveal the roles of the Pb, Ti, O in the ferroelectric $PbTiO_3$ (Figure 4.6). The Fermi energy is 5.41 eV and the band gap for $PbTiO_3$ is 1.5 eV. In Fig. 4.6(b), there are sharp peaks for Ti *3d* and O *2p* around 8 eV in the conduction band and around 3 eV in the valence band. These peaks indicate that the number of Ti *3d* and O *2p* electrons in the same energy range increases greatly, and thus there is a strong hybridization between Ti *3d* and O *2p* in the ferroelectric $PbTiO_3$. Hybridizations between O *2s* and Pb *5d* can also be observed at around -10.5 eV. These hybridizations between O *2p* electrons and Ti *3d* electrons and between O *2s* and Pb *5d* electrons are the main forces behind the dramatic ionic movement in the ferroelectric lead titanate, as they

weaken the short range repulsion, and hence stabilize the ferroelectric structure of lead titanate. This observation is consistent with many simulation and experiment results [73, 92, 117-121, 123, 124].

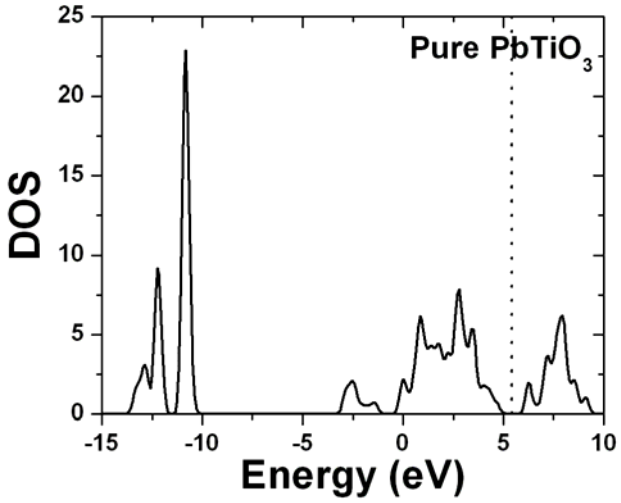

(a)

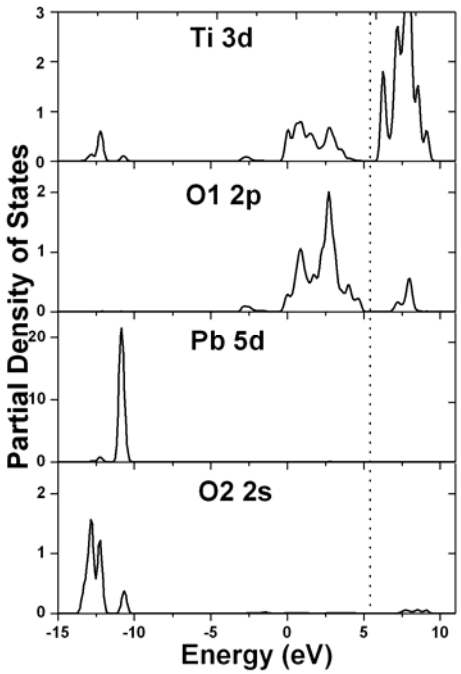

(b)

Figure 4.6: (a) Total DOS of $PbTiO_3$, and (b) PDOS of Pb, Ti and O ions

4.3 Crystal and Electronic Structures of Lead Titanate Zirconate

4.3.1 Computational Methodology

Following the study of $PbTiO_3$, we study the more complicate structure of $Pb(Zr_{0.5}Ti_{0.5})O_3$, a supercell containing two subcells (Figure 4.7). Each subcell is a simple perovskite structure, where Zr^{4+}/Ti^{4+} anion is located at the centre and Pb^{2+} anions at the corners. In this model, the $PbTiO_3$ subcell is on the top of the $PbZrO_3$ subcell. The calculation was performed with generalized gradient approximation (GGA) to the density functional theory (DFT), using the projector-augmented wave (PAW) method. The Perdew-Burke-Ernzerhof (PBE) exchange-correlation parameterization was used in the calculations. Pb *5d*, *6s*, *6p*, Ti *3d*, *4s*, Zr *4s*, *4p*, *4d*, *5s* and O *2s*, *2p* orbitals are treated as valence orbitals. The supercell is calculated by fixing its volume to the experimental value ($141.86\times10^{-24}cm^3$) throughout the geometry relaxation; as we have discussed previously, small differences have great impact on the ferroelectric properties of the material. Convergence tests were performed before geometry relaxation. As seen from Figure 4.8, the cutoff energy can be set at 700 eV, and the special-points method applied for the Brillouin zone sampling is 8×8×4 Monkhorst Pack mesh.

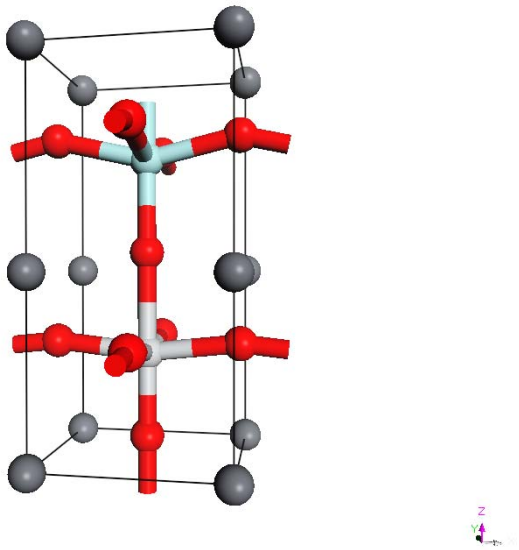

Figure 4.7: Unit cell of $Pb(Zr_{0.5}Ti_{0.5})O_3$, where the grey spheres denote Pb atom, the red spheres are oxygen atoms, the white/cyan spheres are Ti/Zr atoms.

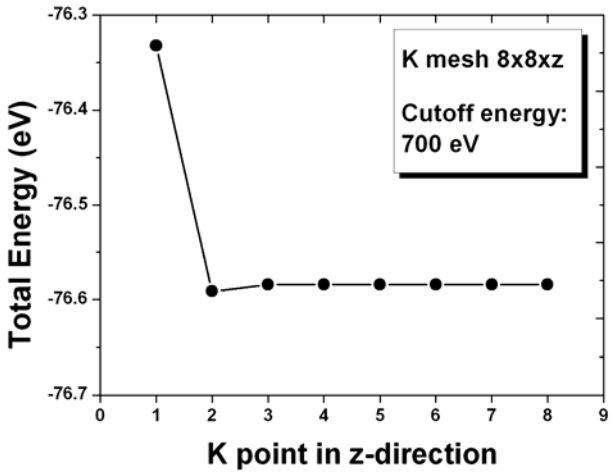

(a)

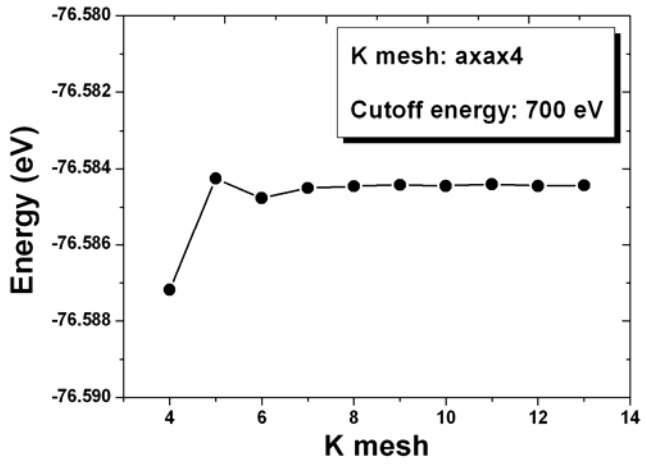

(b)

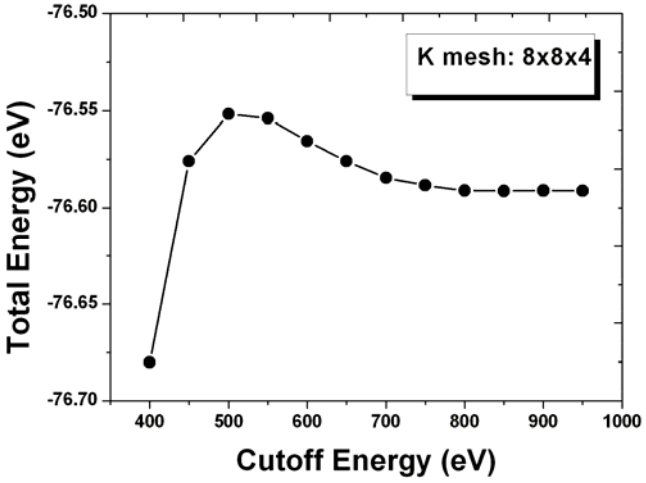

(c)

Figure 4.8: Convergence tests on (a), (b) k mesh size in Irreducible Brillouin Zone (IBZ), and (c) cutoff energy using GGA.

4.3.2 Crystal Structure

After the geometry optimization, the ions are fully relaxed to their equilibrium positions. The optimized ion positions are shown in Table 4.3. Particularly, O_1 denotes the oxygen in the bottom plane, and O_4 denotes the oxygen in the plane in between the

$PbZrO_3$ subcell and $PbTiO_3$ subcell. Some comments should be made here. Firstly, both zirconium and titanium show small displacements towards the topmost Pb-O plane in the supercell. Moreover, $O_{2,3}$ and $O_{5,6}$ display larger displacements towards the same plane, similar to those in the single $PbTiO_3$ unit cell. Furthermore, the middle Pb-O plane separates the Zr and Ti cells move toward the bottom Pb-O plane to compress the $PbTiO_3$ subcell, thus shrinking the $PbTiO_3$ subcell and correspondingly an expansion of $PbZrO_3$ subcell. The c/a ratio of $PbTiO_3$ subcell decreases from 1.065 to 0.976, thus its cell is no longer tetragonal.

Table 4.3: Comparison of calculated and experimental lattice parameters of $Pb(Ti_{0.5}Zr_{0.5})O_3$.

	Tetragonal(*P4mm*)			
	Experiment [118]	GGA-PBE	$PbTiO_3$ subcell	$PbZrO_3$ subcell
a	4.009	4.009	4.009	4.009
c/a	1.027	1.044	0.976	1.112

Table 4.4: Relaxed fractional positions of ions in the $Pb(Ti_{0.5}Zr_{0.5})O_3$ supercell.

Ion Type	x	y	z(equilibrium)	z(centro-symmetry)
Pb1	0	0	0	0
Pb2	0	0	0.467	0.467
Ti	0.5	0.5	0.259	0.234
Zr	0.5	0.5	0.754	0.734
O1	0	0	0.043	0.000
O2	0	0.5	0.285	0.234
O3	0.5	0	0.285	0.234
O4	0.5	0.5	0.516	0.467
O5	0.5	0	0.809	0.734
O6	0	0.5	0.809	0.734

4.3.3 Electronic Structure

We further compare the electron density distribution in order to understand the ferroelectric effects in $Pb(Ti_{0.5}Zr_{0.5})O_3$ (Figure 4.9), and the difference with lead titanate. The diagrams show that the ferroelectricity in PZT results in two different behaviors of $PbZrO_3$ subcell and $PbTiO_3$ subcell. Firstly, as to the $PbZrO_3$ subcell, ferroelectricity results in the same behavior as in the pure PbTiO3 unit cell: (1) a chemical breaking of some Zr-O_1 bonds in the (001) direction and (2) a strong covalence between Zr and O_4 at the other side. Thus we can say the formation of ferroelectricity in PZT leads to an enhancement of hybridization between Zr and O orbitals. Secondly, in the $PbTiO_3$ subcell, we can see: (1) a strong covalence between Ti and O_4, and (2) no obvious chemical breaking of Ti-O_1 bond in the (001) direction.

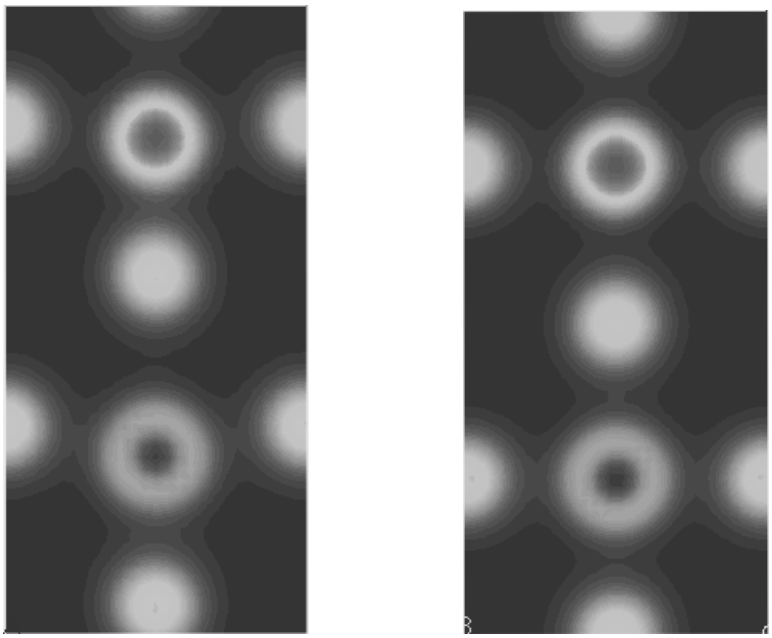

(a) (b)

Figure 4.9: (a) Electron density plotted in the (100) plane for ferroelectric $Pb(Zr_{0.5}Ti_{0.5})O_3$ supercell cell, (b) Electron density plotted in the (100) plane for centro-symmetric $PbZr_{0.5}Ti_{0.5}O_3$ unit cell. Ti^{4+} anion is in the centre of the upper sub-cell and the Zr^{4+} is in the centre of the bottom cell. The rest are O^{2-} cations.

Table 4.5: Comparison of bond lengths in equilibrium and ideal states of $Pb(Ti_{0.5}Zr_{0.5})O_3$.

Bond Type\Length	Equilibrium	Centro-symmetry	Δ%
O_1-Ti	1.808	1.956	-7.67%
O_4-Ti	2.151	1.956	9.88%
$O_{2,3}$-Ti	2.017	2.004	0.61%
O_1-Zr	2.419	2.229	8.60%
O_4-Zr	1.992	2.229	-10.54%
$O_{2,3}$-Zr	2.056	2.004	2.58%

This observation can be confirmed by calculating the bond-lengths among different ions in the ferroelectric phase. These bond lengths in the ferroelectric state are compared with those in the centro-symmetry structure (Table 4.5), and are visualized in Figure 4.10. It can be seen from Table 4.5 that when transition from centro-symmetric phase to ferroelectric phase takes place, bond length between ions changes: (1) in the $PbTiO_3$ subcell the O_4-Ti bond is lengthened from 1.96 Å to 2.15 Å and O_1-Ti bond is shortened from 1.96 Å to 1.81 Å; in the $PbZrO_3$ subcell, the O_4-Zr bond is shortened from 2.23 Å to 1.99 Å and O_4-Zr is lengthened from 2.23 Å to 2.42 Å. These changes are caused by the relative motions of Zr, Ti, O_1 and O_4; (2) both $O_{2,3}$ – Ti bonds in $PbTiO_3$ subcell and $O_{2,3}$-Zr bonds in $PbZrO_3$ subcell are lengthened (from 2.00 Å to 2.02 Å, and from 2.00 Å to 2.06 Å, respectively). When the structure is at its equilibrium, we can observe that the O_1-Ti bond is the shortest and O_1-Zr bond is the longest.

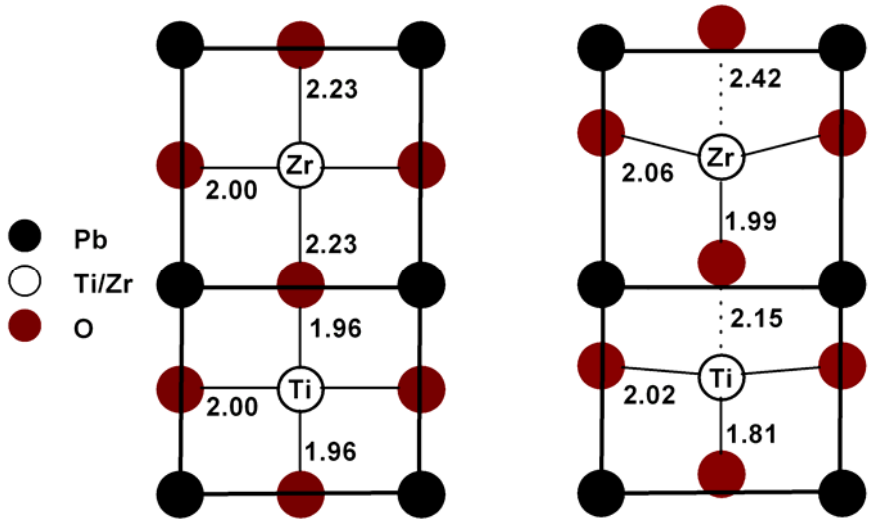

Figure 4.10: Ideal and equilibrium states of $Pb(Ti_{0.5}Zr_{0.5})O_3$ supercell. The unit for the bond length is Å.

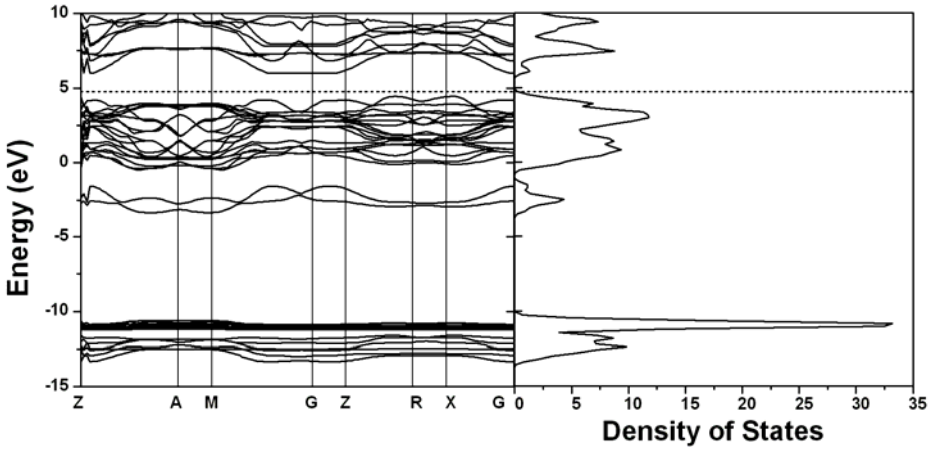

Figure 4.11: Band structure and density of states (DOS) of $Pb(Ti_{0.5}Zr_{0.5})O_3$.

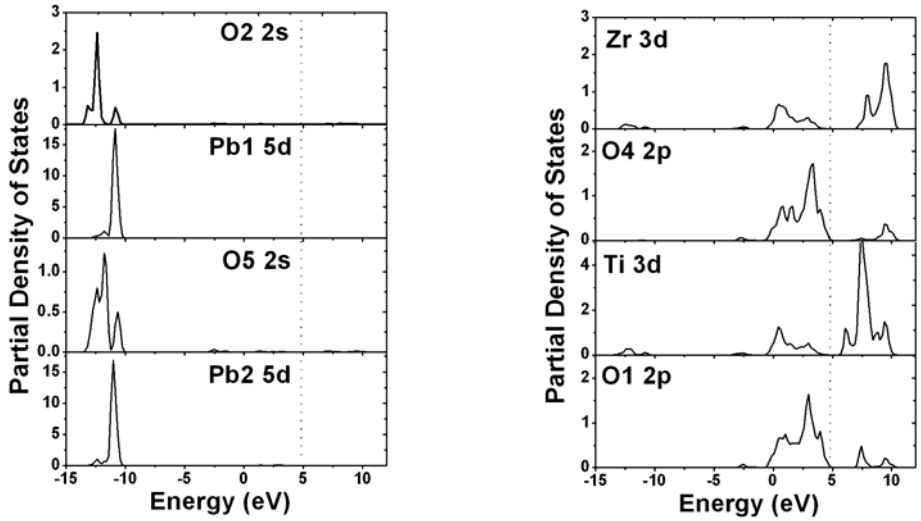

Figure 4.12: Partial density of states (PDOS) for Pb, Ti, Zr, and O ions

In order to understand more clearly the ferroelectricity of lead zirconate titanate, its band structure, density of states and partial density of states were calculated (Figs. 4.11, 4.12). Similar to lead titanate, there are sharp peaks for both O_1 2p - Ti 3d and O_4 2p - Zr 3d electrons at about 7.5 eV and 3 eV (Figure 4.), indicating strong hybridizations

between O_1 2p - Ti 3d and O_4 2p - Zr 3d pairs. Besides, a strong hybridization can be found between Pb_1 p and $O_{2,3}$ 2p, and Pb_2 and $O_{5,6}$ at 6eV.

4.4 Summary

In summary, we investigate the crystal structure, electronic structure, and origin of ferroelectricity in lead titanate and lead zirconate titanate to provide basic information for our further studies.

The failure of the density function theory to describe the ground states of perovskite oxides is firstly identified, and hence all the calculations on the perovskite structures are conducted by either fixing the unit cell at experimental volume or at experimental lattice parameters.

By examining the ionic motion and density of states of electrons, we discussed the origin of the ferroelectricity in lead zirconate titanate. It is generated by the significant ionic displacement stabilized by the hybridizations between oxygen and B-site ions. These hybridizations weaken the short-range repulsions between ions and stabilize the ferroelectric structure of lead zirconate titanate.

In summary, the preliminary studies on the pure lead zirconate titanate in this chapter identify several important technical and physics issues that are of vital

importance to the accuracy and validity of our calculations. Therefore this chapter lays a solid foundation for our further investigations.

Chapter V

Point Defects in Lead Zirconate Titanate

Materials in this chapter have been published in Applied Physics Letters (Volume 88, Page 142902), and Journals of Alloys and Compounds (Volume 449, Page 362). They are reproduced with permission of American Institute of Physics and ELSEVIER.

The abundance of the intrinsic defects in lead zirconate titanate, particularly the vacancies, brings about severe long-run performance degradations and reliability issues including fatigue, imprint, and retention in the ferroelectric devices. Therefore, the information about the formations of the point defects in lead zirconate titanate is of great interest, not only to the understanding the origin of degradation behaviors, but also as an important reference for the studies on the elemental substitution effects in the following chapters.

5.1 Introduction

It has long been experimentally observed that either $Pb(Zr,Ti)O_3$ or $PbTiO_3$, in whichever form (thin film or bulk), contains abundant intrinsic defects due to high Pb evaporation during fabrication through the following defect reaction [125-127]:

$$Pb_{Pb} + \frac{1}{2}O_2(gas) \rightarrow PbO + V''_{Pb} + 2h^{\bullet\bullet} \qquad (5\text{-}1)$$

where Pb_{Pb} denotes lead in the lattice, and V''_{Pb} represents the Pb vacancy. Furthermore, the formation of Pb vacancies may cause the creation of oxygen vacancies through the Schottky equilibria in order to keep local electro-neutrality, as shown in Eq. (5-2):

$$\text{null} \rightarrow V''_{Pb} + V^{\bullet\bullet}_{O}. \qquad (5\text{-}2)$$

These intrinsic defects have tremendous impacts on the overall performance of the ferroelectric devices. Loss of lead from the lead titanate and PZT has been experimentally confirmed to contribute to initial reduction in remnant polarization and leakage current [128]. The oxygen vacancies are responsible for the polarization fatigue by playing different roles such as trapping charge carriers, pinning domain walls, screening the electrical field near the space charge region, and impeding the displacement of the Ti ion [9, 11, 13-15, 52, 53, 57].

Therefore, intensive experiments [37, 125, 126, 128] have been carried out to investigate the formation of defects in lead titanate and lead zirconate titanate. It was

found that increasing oxygen partial pressure reduces the concentration of oxygen vacancies but increases the number of metal vacancies and holes [37, 125, 126]. However, the studies so far have been limited to theoretical ones. Man et al. [97] calculated formation of vacancies in $PbTiO_3$ based on molecular dynamic simulation. Poykko et al. [95] calculated V_{Pb} and Vo pairs. However, formation energies of V_{Pb} and Vo were not calculated because of the difficulty in estimating the chemical potentials of oxygen and Pb in lead titanate system.

Therefore, in this part, the formation of intrinsic vacancies is studied. Specifically, we are interested in presenting important information on the formation energies of different types of vacancies under different thermo-chemistry conditions (oxidizing and reducing) and with different charged states. In addition, we propose the ionization levels can offer more reliable explanations to the origin of p-type conductivity in the lead titanate system. This fundamental information is important because it allows us to obtain a clear and thorough image of the defect formations in $PbTiO_3$ and PZT systems, which is essential for future investigations on elemental substitutions.

5.2 Computational Methodology

The calculations in this study are based on GGA to the DFT using the projector-augmented wave (PAW) method. Perdew-Burke-Ernzerhof (PBE) exchange-correlation parameterization is used in the calculation. The pseudopotential approach is adopted in which electrons close to the nuclei were frozen, and only valence

electrons were considered to contribute to the bonding between atoms. Pb *5d*, *6s*, *6p*, Ti *3d*, *4s*, and O *2s*, *2p* orbitals are regarded as valence orbitals. Therefore 36 electrons are regarded as valence electrons per lead titanate unit cell.

The formation energy of a charged vacancy in certain system can be calculated using the equation below:

$$E_f^q = (E_{defect}^q - E_{perfect}^q) - \mu_v + qE_f \tag{5-3}$$

where E_{defect}^q and $E_{perfect}^q$ are the total energy of the defected and perfect lead titanate respectively in the charged state q, μ_v denotes the corresponding atomic chemical potential, and E_f is the Fermi energy of $PbTiO_3$. In our calculations, we apply a monopole correction $\frac{e^2Q^2\alpha}{a\varepsilon}$ to the total energy of the charged systems, where α is the Madelung constant, a is the lattice constant, and ε is the dielectric constant of the lead titanate.

2×2×2 supercells with 40 atoms are used to calculate the perfect and defected lead titanate. In addition to the lead and titanium vacancies, two types of oxygen vacancies are also considered: the oxygen ion (O_1) bonded with titanium in z direction, and the oxygen ion (O_2) bonded with titanium in x-y plane. Moreover, in order to test the validity of the results, these vacancies are also considered in 2×2×4 supercells with 80 atoms. The calculated formation energy and the predicted ionization levels show no great differences (<0.02eV) with those by 40-atom supercells. Before any geometry relaxation and energy or property calculation, the convergence tests are performed from which the cutoff

energies for all supercells are obtained to be 400 eV. The numerical integration is precisely carried out by using 8 k-points in the Brillouin zone. For all the calculations in this work, the unit cell volume of lead titanate is fixed at experimental volume (63.28 $Å^3$/unit cell) [122]. The ion positions and the shape of the lead titanate in the equilibrium state were then determined at this given volume. The total energy of the supercell with a point defect is calculated in the partial relaxed condition where only the first and second nearest ions near the vacancy are allowed to move during computation while lattice parameters and other ion positions are kept fixed. In another test, the total energy of the supercell is calculated in the condition where all ion positions are relaxed. Difference of energies obtained from these two conditions is within 0.2%.

Table 5.1 Comparison of theoretical lattice parameters with experiment values of $PbTiO_3$, Ti, PbO, TiO_2, Pb, and O_2.

Material	$PbTiO_3$		Ti			½ O_2
Space Group	P4mm		$P6_3/mmc$			Isolated Molecular
Lattice parameter	a	c	a	c	α	bond length
Calculated (Å)	3.91	4.15	2.93	4.88	120.0	1.20
Experiment (Å)	3.90	4.15	2.96	4.68	120.0	1.21
Chemical Potential (eV)	-37.5725		-7.67			-4.47
Material	PbO		TiO_2			Pb
Space Group	P4/nmm		$P4_2/mnm$			$Fm\bar{3}m$
Lattice parameter	a	c	a	c		a
Calculated (Å)	4.04	4.98	4.60	2.95		4.95
Experiment (Å)	3.95	4.99	4.95	3.00		4.95
Chemical Potential (eV)	-10.88		-26.43			-2.75

The chemical potentials are also calculated for the reference materials including Pb ($Fm\bar{3}m$), Ti ($P6_3/mmc$), PbO (P4/nmm), and TiO_2 ($P4_2/mnm$). In addition, the chemical potential of oxygen is considered to be in the form of isolated molecules, placed in a periodic box with dimension 20Å×20Å×20Å. The numerical integration is carried out at the Gamma Point only. For all the materials considered in this study, the ions and lattice parameters are relaxed to equilibrium states when the system energies reached to the minima. When the calculated results are compared with the experimental values, they show good agreement as tabulated in Table 5.1. Their chemical potentials, evaluated as per unit formula, are also given in Table 5.1.

5.3 Formation Energy of Intrinsic Neutral Vacancies

As can be derived from equation (5-3), the formation energy E_f of a neutral vacancy in a closed system (where q=0) is written as:

$$E_f^0 = (E_{defect}^0 - E_{perfect}^0) - \mu_v \tag{5-4}$$

where E_{defect}^0 and $E_{perfect}^0$ are respectively the total energy of the supercell with a neutral vacancy and the total energy of the perfect supercell, and μ_v denotes the chemical potential of escaping atom. Eq. (5-4) states that the formation energy not only depends on the difference between the energies of defect and perfect systems but also on the chemical potential of escaping atom, which may end up in various phases. For example, assuming that Pb can be present in two forms, pure Pb and PbO, after escaping from the $PbTiO_3$, the chemical potential, μ_{Pb}, in the former case is the chemical potential of Pb

in its pure state while that in the latter case the chemical potential, μ_{Pb}^{PbO}, is that in PbO state.

Therefore, the chemical potential depends on different parameters such as partial pressures and growth conditions. However, in a ternary element system, the determination of the chemical potential of atoms in the system is more complex than that of binary element system; we should take a ternary-phase equilibrium state into consideration so that we can gain insight on all the chemical potentials of atoms. Therefore, in our calculations, we assume that a $PbTiO_3$ system is respectively placed in five different environments. In all thermo-chemical conditions, $PbTiO_3$ finally reaches its equilibrium with respective environmental atmospheres. In the equilibrium state, chemical potentials of the Pb, Ti and O should satisfy the following relationship in order to coexist in the lead titanate system:

$$\mu_{Pb} + \mu_{Ti} + 3\mu_{Ti} = \mu_{PbTiO_3} \tag{5-5}$$

where μ is respectively the chemical potential of Pb, Ti or O in $PbTiO_3$ system. Moreover, their chemical potentials are equal to those in the environment in equilibrium conditions. The details on five thermo-chemistry conditions and chemical potentials of Pb under each thermo-chemistry point are given in Table 5.2.

Table 5.2: The external atmospheres and chemical potentials of lead in lead titanate under five thermo-chemistry conditions.

Condition	External Atmosphere	Chemical potential of lead, μ_{Pb}
1	PbO, Pb	$\mu_{Pb(reference)}$
2	PbO, O_2	$\mu_{PbO(reference)} - \mu_{O(reference)}$
3	TiO_2, O_2	$\mu_{PbTiO3(reference)} - \mu_{O(reference)} - \mu_{TiO2(reference)}$
4	TiO_2, Ti	$\mu_{PbTiO3(reference)} - \mu_{Ti(reference)} - 3(\mu_{TiO2(reference)} - \mu_{Ti(reference)})/2$
5	Ti, Pb	$\mu_{Pb(reference)}$

The reference chemical potentials in Table 5.2 can be obtained by calculating the reference materials, as given in Table 5.1. The chemical potentials of all other types of ions such as Ti and O in the ternary system under different conditions can be deduced in the same manner. The results for all chemical potentials are shown in Table 5.3.

Table 5.3: Calculated chemical potentials of elements in ferroelectric phase lead titanate under five thermo-chemistry conditions.

Chemical Potential	μ_{Pb} (eV)	μ_{Ti} (eV)	μ_{O} (eV)
Condition 1	-2.75	-10.41	-8.14
Condition 2	-6.42	-17.75	-4.47
Condition 3	-6.67	-17.49	-4.47
Condition 4	-1.76	-7.67	-9.38
Condition 5	-2.75	-7.67	-9.05

Table 5.4: Calculated formation energy for the neutral vacancies in lead titanate system under five thermo-chemistry conditions.

Condition	O_2 Atmosphere	Pb Vacancy (eV)	Ti Vacancy (eV)	O_1 Vacancy (eV)	O_2 Vacancy (eV)
1	Poor	4.96	10.78	1.40	1.50
2	Rich	1.29	3.44	5.07	5.17
3	Rich	1.03	3.70	5.07	5.17
4	Poor	5.94	13.52	0.16	0.26
5	Poor	4.96	13.52	0.49	0.59

Substituting the chemical potentials of Pb, O and Ti in five conditions into Eq. (5-4), respectively, the formation energy of three types of vacancies can be calculated; the results are tabulated in Table 5.4.

Comparison of the formation energies among Pb, O and Ti vacancies explicitly indicates that the formation energy of an oxygen vacancy possesses the lowest level in all the O_2-poor conditions (0.26 – 1.50 eV), indicating that the oxygen vacancy is always relatively easier to form in the lead titanate system. This conclusion agrees well with experimental findings that oxygen vacancies are natural defects in $PbTiO_3$ and PZT after firing in reducing atmosphere [125, 126, 128]. In addition, we can see a reduction in the formation energy of Pb vacancy in conditions 2 and 3 where the system is placed in an O_2-rich (oxidizing) environment, compared with those in conditions 1, 4 and 5 where the system is synthesized in an O_2-poor (reducing) atmosphere. The present calculated results prove the experimental observations that a relatively high partial oxygen pressure can

cause the Pb loss during synthesis, forming p-type conductivity structure [125, 126, 128]. As the oxygen partial pressure increases, the $PbTiO_3$ conductivity was found to increase [125, 126, 128]. However, this phenomenon seems to be contrary to the experimental observation in pulsed laser deposition, where the Pb loss is prevented when elevated oxygen partial pressure is employed. The reason for this is that the high oxygen partial pressure can suppress re-sputtering of Pb [127]. However as the oxygen partial pressure increases above acertain value, the Pb loss will again be induced because of its low formation energy.

The formation energy of titanium vacancies is relatively higher under either the O_2 rich or O_2 poor conditions. Therefore, it is difficult to form titanium vacancies, which also well agrees with experimental observations that Ti vacancies are seldom present. Moreover, under all conditions, the formation energy of the vacancy of oxygen bonded with Ti in the z direction is always 0.1 eV smaller than that of the oxygen bonded with Ti in the x-y plane. Due to the fact that ferroelectricity of $PbTiO_3$ can be greatly stabilized by high hybridization of O_1 and titanate [118, 119, 124], the present *ab initio* study clearly indicates that the atmosphere greatly affects the ferroelectricity.

5.4 Formation Energy of Intrinsic Charged Vacancies

We also calculated the vacancies in lead titanate with charged states, which could offer more insight into the origin of leakage current in lead titanate. In order to obtain a simple picture, only two thermochemistry conditions in Table 5.2 are considered, under

which two other phases coexist with $PbTiO_3$: oxygen-rich condition (1) and oxygen-poor condition (4). The chemical potential can be deduced in the same way as shown in Table 5.3. However, the other conditions can be derived in the same manner.

Formation energies as a function of Fermi level for the charged vacancies were calculated under two thermo-chemistry conditions. Under the oxygen rich condition (Figure 5.1), the formation energies of lead vacancies are negative throughout the band gap; that is to say, the formation of lead vacancy is exothermic and therefore spontaneous during the $PbTiO_3$ crystal growth and the lead vacancies may contribute to the p-type conduction. In addition, no potential 'hole-killer' vacancy is stable in Figure 5.1.

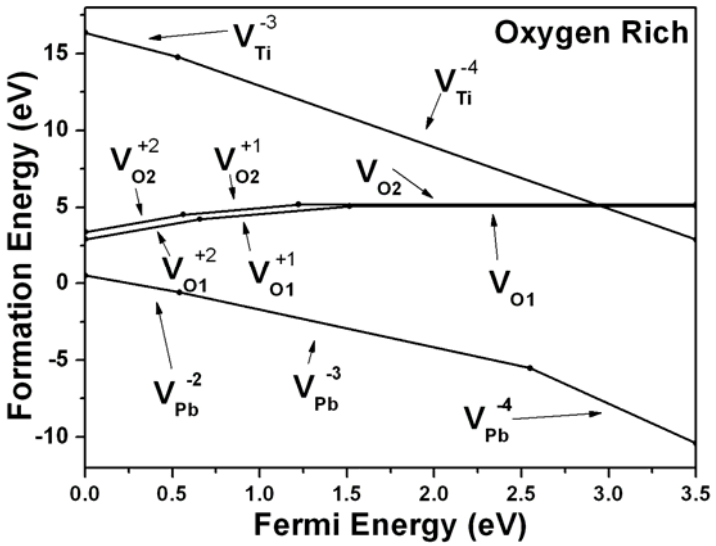

Figure 5.1: Calculated defect formation energy for vacancies as a function of the Fermi level in oxygen rich condition. Only the vacancies among the lowest formation energies are shown. The zero of the Fermi level is set to the top of the valence band.

Under the oxygen poor conditions (Figure 5.2), however, lead titanate does not possess the p-type conductivity experimentally. This can be explained by the negative formation energy of oxygen vacancy (V_O^{+2}) at the top of valence band, which is even lower (or more stable) than that of lead vacancy at the same Fermi level. The huge rise in population of the oxygen vacancies has negative effects on the conductivity of the system. On the one hand, these oxygen vacancies are able to "kill" most of the holes emitted by the lead vacancy (-2) and weaken the p-type conduction; on the other hand, these oxygen vacancies are too far from the conduction band to contribute to the n-type conduction. This corresponds to the experiment findings that the conductivity of lead titanate decreases as the external oxygen partial pressure decreases and no n-type conductivity is observed in experiments [125, 126].

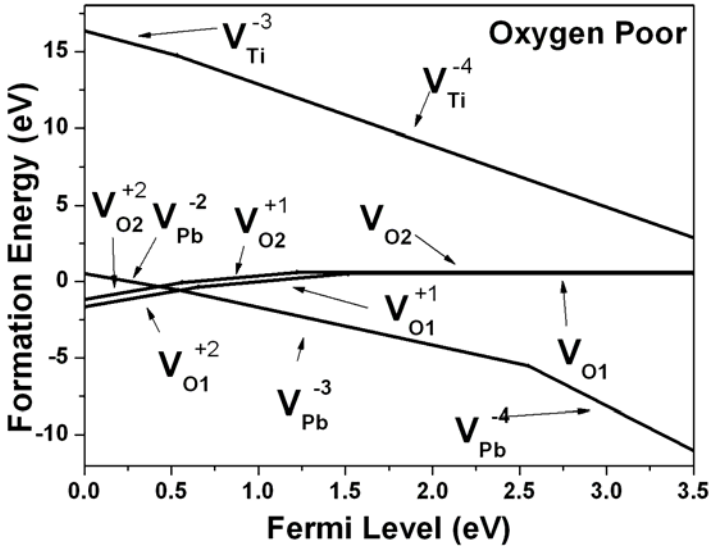

Figure 5.2: Calculated defect formation energy for vacancies as a function of the Fermi level in oxygen-poor condition. Only the vacancies among the lowest formation energies are shown. The zero of the Fermi level is set to the top of the valence band.

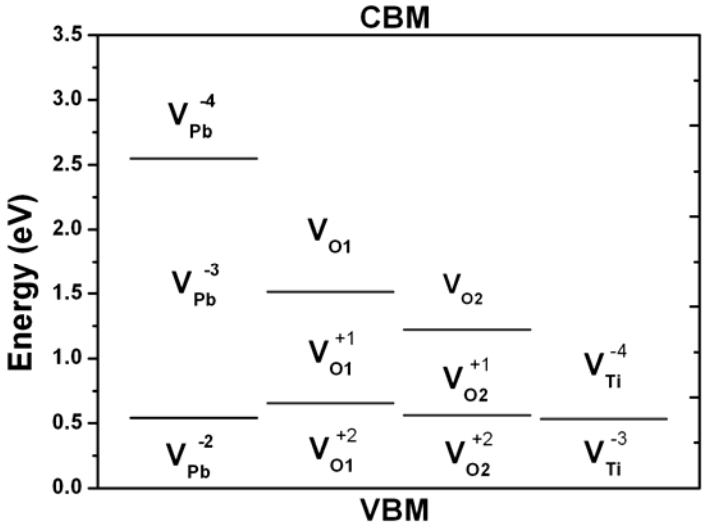

Figure 5.3: Ionization levels in the bandgap for V_{Pb}, V_{O1}, V_{O2} and V_{Ti} in $PbTiO_3$. VBM stands for valence band maximum and CBM for conduction band minimum.

Furthermore, the studies on charged states confirmed that under either reducing or oxidizing atmosphere, the formation energy of O_1 is 0.1 eV lower than that of O_2, which indicates that an O_1 vacancy is more readily formed than an O_2 one, and thus influence the ferroelectricity of the crystal. In addition, the formation energy of all charged and neutral titanium vacancies is positive across the band gap under both the oxygen rich and oxygen poor conditions; this may explain why titanium vacancies are hardly observed experimentally.

5.5 Summary

We have calculated the formation energies of the neutral and charged vacancies in lead titanate system at different thermochemical conditions. Our simulation results

indicate that under an oxidizing atmosphere, lead vacancies can easily form during high temperature heating. Under a reducing atmosphere, oxygen vacancies are more stable than any other vacancies. Furthermore, under both atmospheres the vacancies of the oxygen bonded with Ti in z direction are always easier to form than those bonded with Ti in x–y plane. Our calculations also show that the Ti vacancy is difficult to form due to its high formation energy under all conditions.

Moreover, we found that the lead vacancy has a stable charge states from -2 to -4, under oxygen rich conditions, while metastable oxygen as well as unstable titanium vacancies have charge states from 0 to +2, and -3 to -4 respectively (Figure 5.3). We demonstrated that lead vacancies are acceptors and contribute to p-type conduction under oxygen-rich condition, which agrees well with experiments. However, under oxygen poor conditions, the oxygen vacancy is stable near the top of valence band (as a deep donor), which may dilute the accepter carriers (hole-killer) to weaken the p-type conduction. Furthermore, as a deep donor, oxygen vacancy is not expected to contribute to n-type conduction neither. Thus for non-volatile application, the oxygen rich condition is preferred in order to suppress the oxygen vacancy formation. However, the chemical potential (thus the oxygen pressure) can be controlled in case of a huge population of Pb vacancies, which are also not welcomed in ferroelectric devices.

Chapter VI

Donors Substituted Lead Zirconate Titanate

Materials in this chapter have been published in Applied Physics Letters (Volume 89, Page 152909), and Physical Review B (Volume 76, Page 125102). They are reproduced with permission of American Institute of Physics and American Physical Society.

In chapter V, the formations of the intrinsic defects and their detrimental effects on the ferroelectricity in lead zirconate titanate have been discussed. In order to reduce the effects of these intrinsic defects, we introduce dopants into the lead zirconate titanate lattice. By controlling the concentration of the intrinsic defects, substitutions offer an opportunity to tune the properties and performances of lead zirconate titanate. In this chapter, we look into the donor substitution effects on lead zirconate titanate.

6.1 Introduction

We have presented in chapters II that lead zirconate titanate with its high remnant polarization, a high dielectric constant and a low processing temperature, currently is one of the most technologically important materials. However, PZT suffers from a severe fatigue problem, particularly when platinum is used as the electrode. It is now widely believed that many crucial mechanisms leading to fatigue are associated with the formation and redistribution of oxygen vacancies in the PZT thin films [8, 52]. Oxygen vacancies are believed to be trapped at the interfaces between PZT and electrodes resulting in a space charge layer, which has the same characteristic as a Schottky barrier [11]. Furthermore, oxygen vacancies can also pin the movement of domain walls by forming oxygen vacancy planes [48, 49, 54], leading to a reduction in the domain wall mobility. Therefore, suppression of the oxygen vacancy concentration in the PZT thin films is the key in improving their fatigue properties. In addition, some theoretical studies have shown that the possible origin of the fatigue is associated to the reduced π bonds between Ti *3d* and O *2p* states caused by electrons released from oxygen vacancies [17]. While the appearance of ferroelectricity is closely related to the magnitude of these bonds, occupation of Ti *3d* states by electrons is detrimental to the bonding. Consequently, the ferroelectricity is undermined. Therefore, a reduction in the occupation of Ti *3d* states by the electrons could be another key to improving the fatigue behavior of PZT.

Unfortunately, as discussed in the Chapter IV, the formation of oxygen vacancies seems to be inevitable in PZT due to Pb evaporation during the processing. Experiments

have shown that lead vacencies can be easily formed [129, 130], which is also verified by our *ab initio* calculation in the last chapter. Furthermore, the formation of Pb vacancies may cause the creation of oxygen vacancies through the Schottky equilibrium in order to keep local electro-neutrality, as shown in Eq. (1):

$$null \rightarrow \mathrm{V}_{\mathrm{Pb}}^{''} + \mathrm{V}_{\mathrm{O}}^{\bullet\bullet} \tag{6-1}$$

Poykko and Chadi [95] found that this Schottky vacancy pair is not closely bounded. Therefore, the oxygen vacancies are sufficiently mobile to migrate to the electrode interface, or form oxygen vacancy planes to pin the domain walls. To reduce formation of oxygen vacancies, some donors could be used, while still allowing the Pb vacancy to exist. The donors Nb, W, and La are shown as examples. As shown in Eq. (6-2), Eq. (6-3) and Eq. (6-4), the two holes caused by Pb evaporation can be compensated by two electrons from the donor dopants instead of formation of oxygen vacancies:

$$Nb_2O_5 \rightarrow V_{Pb}^{''} + 2Nb_{Ti}^{\bullet} + 5O_O^x \tag{6-2}$$

$$WO_3 \rightarrow V_{Pb}^{''} + W_{Ti}^{\bullet\bullet} + 3O_O^{\mathrm{x}} \tag{6-3}$$

$$La_2\mathrm{O}_3 + \frac{7}{2}\mathrm{O}_2 \rightarrow V_{Pb}^{''} + 2La_{Pb}^{\bullet} + 9\mathrm{O}_O^x \tag{6-4}$$

Several dopants have been explored for PZT, and an improved fatigue behavior was found with prevention of the formation of oxygen vacancies [20-26, 33-35, 64-67]. As there is lack of thorough study on the elemental substitution effect of donors, we provide a systematic study on the effect of B-site donor substitution on fatigue behavior of PZT using *ab initio* calculations.

6.2 Selection of Substitution Candidates

In order to offer a systematic study, all the appropriate donor substitutions are based on the principle of ferroelectric materials. From an empirical point of view, two primary conditions should be satisfied by these dopants:

(1) The substitution should have higher valence states than original ions.

(2) The radii of the dopants should be comparable to that of the original A/B-site ion, so that the perovskite structure can be maintained.

Based on the rules stated above, group VA, group VIA and group VB elements (B^{5+}) are selected as B-site dopant candidates to substitute Ti/Zr. The ionic radii of group VA elements V, Nb, Ta, and group VB elements Sb, Bi are respectively 0.59, 0.69, 0.68, 0.62, and 0.72 Å with a valency of +5, and those of group VIA elements Mo, W 0.62 and 0.62 Å with a valency of +6, which are compatible with that of Ti^{4+} ion (0.68 Å). In addition, we screened all group IIIA and group VB elements (A^{3+}) as dopants in the Pb site in $PbTiO_3$. The ionic radii of group IIIA elements Sc, Y, La, and group VB elements Sb, Bi are 0.73, 0.89, 1.06, 0.76, and 0.96 Å, respectively, with a valency of +3, which are compatible with that of Pb^{2+} ion (1.20 Å).

The tolerance factor, introduced by Goldschmidt [131], is used to characterize the packing situation of the perovskite structure and is defined as follows:

$$R_A + R_O = t(2)^{1/2}(R_B + R_O)$$

$$\text{Or} \qquad t = (R_A + R_O)/(2)^{1/2}(R_B + R_O) \tag{6-5}$$

where R_A, R_B, and R_O are the ionic radii of A, B and O ions, respectively. When t is equal to 1, the packing is said to be ideal. The tolerance factor was calculated for both $PbBO_3$ and $ATiO_3$ systems with a full A-site/B-site substitution, and is in the relatively stable range (0.75-1.00) of perovskites.

6.3 Computational Methodology

The 2×2×4 supercell is adopted for theoretical calculations. It is assumed that in the doped system, a Pb ion at the spatial centre of the supercell is missing, and one or two Ti ions are replaced by dopants, depending on the chemical valence of the dopants. Besides the substituted systems, PbO deficient, Pb deficient and defect-free PZT systems are also considered in order to compare with the doped ones. The lattice parameter of the supercells, a=b=7.892 Å and c/a = 1.047, are used based on experimental values of the undoped PZT (Zr/Ti = 25/75) [122].

In the calculation of the electronic and ion structures of these systems, the pseudopotential approach is used, where the Pb *5d*, *6s*, *6p*, O *2s*, *2p*, Ti *3d*, *4s*, Zr *4s*, *4p*, *4d*, *5s* orbital were regarded as valence orbitals. For the dopants, the outermost *d* and *s* orbitals of the group IIIA, VA, and VIA elements and outermost *s* and *p* orbitals of group VB elements are considered as valence electrons in the calculations. The plane-wave calculations are based on density functional theory (DFT) with the generalized gradient approximation (GGA). Perdew-Burke-Ernzerhof (PBE) exchange-correlation parameterization is used in the calculations for ionic and electronic ground state. For

density of states and bandgap calculations, the meta-GGA-PBE method is applied due to its better prediction of the bandstructure of the systems. The convergence tests were performed before any geometry optimization, from which a 2×2×1 K-mesh and the cutoff energy at 400 eV for all the supercells are employed. The calculations of the DOS and band structures are conducted with a 6×6×3 K-mesh and a cutoff energy of 400 eV.

6.4 B-site Donor Substituted $Pb(Zr_xTi_{1-x})O_3$

6.4.1 Group VB Elements (Sb^{5+}, Bi^{5+})

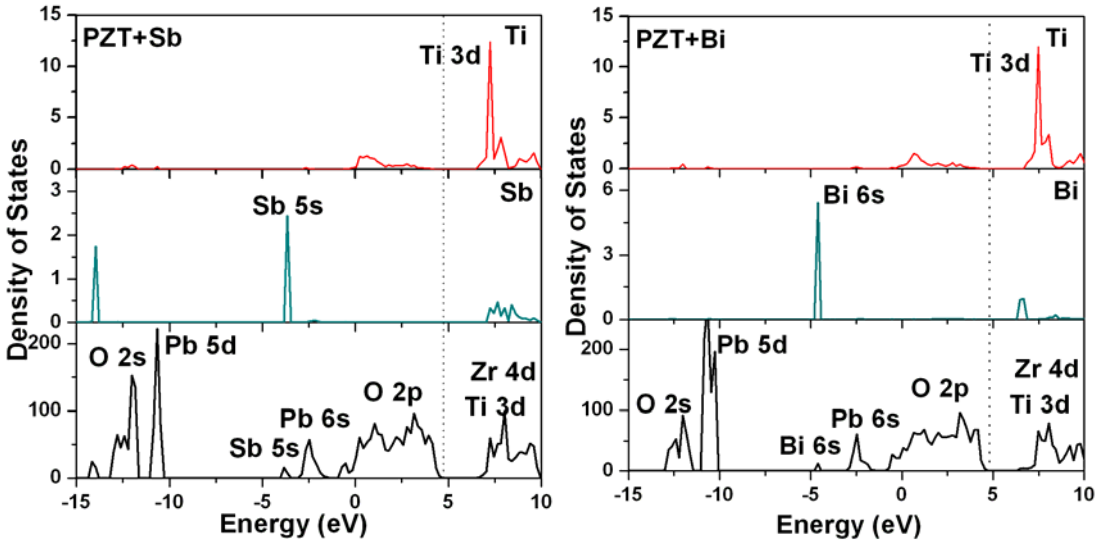

(a) (b)

Figure 6.1: Calculated DOS and PDOS of the PZT systems with (a) Sb substitution and (b) Bi substitution.

The density of states (DOS) of the Group VB Elements (Sb^{5+}, Bi^{5+}) substituted systems were shown in Fig. 6.1. The Bi-substituted PZT (PZTB) and Sb-substituted PZT (PZTS) have similar conduction band structures as that of undoped PZT (Figs 4.6 and 4.12). The energy states of Sb and Bi ions are mainly located below the Fermi level. Once released from the oxygen vacancies, the electrons occupy the Ti *3d* states and reduce the π bonds between Ti *3d* and O *2p* similar as the electrons in undoped PZT.

6.4.2 Group VA Elements (V^{5+}, Nb^{5+}, Ta^{5+}) and Group VIA Elements (Mo^{6+}, W^{6+})

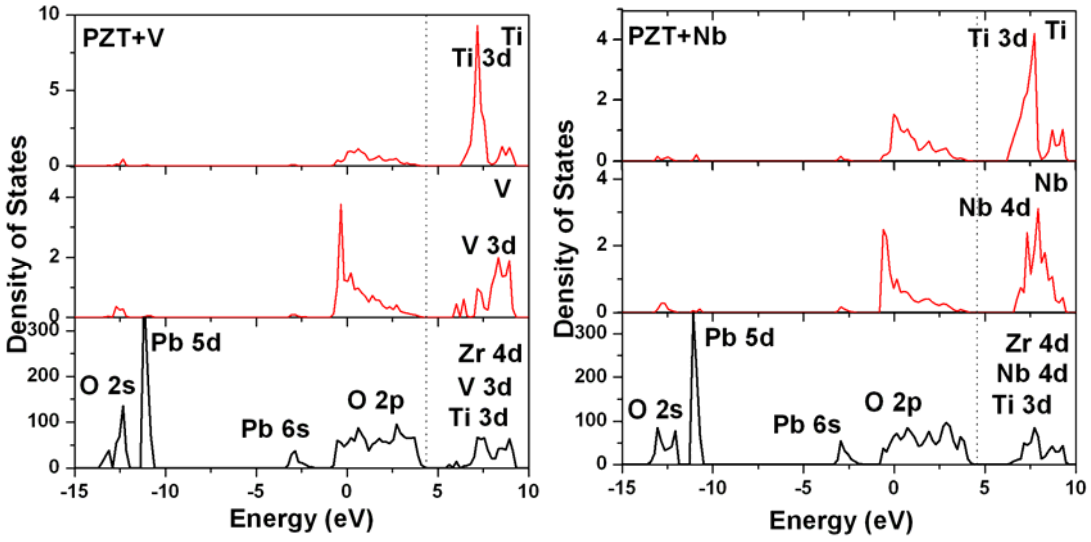

(a) (b)

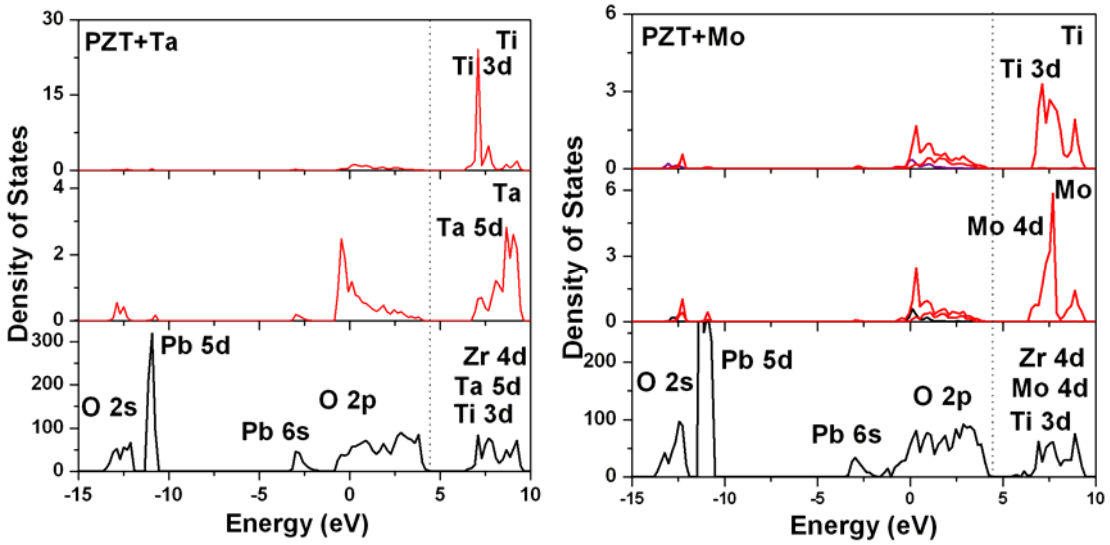

(c)

(d)

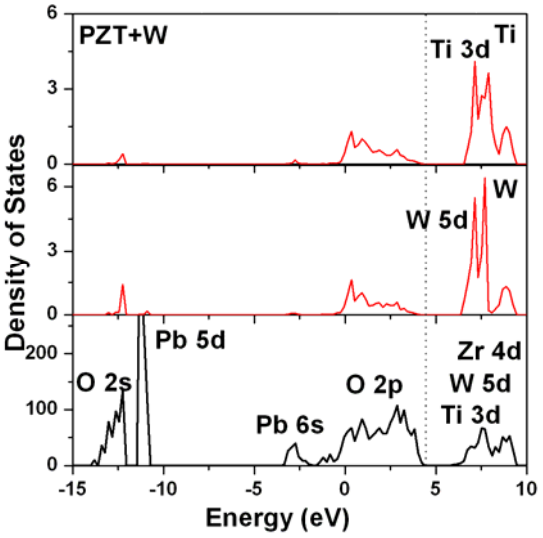

(e)

Figure 6.2: Calculated DOS and PDOS of the PZT systems with (a) V substitution, (b) Nb substitution, (c) Ta substitution, (d) Mo substitution, and (e) W substitution.

Contrary to the group VB donors substituted into lead zirconate titanate, the group VA elements substituted systems have the conduction band minimums (CBM) that consist of both *d* states of the dopants and Ti *3d* states. V *3d* states in V-doped PZT

(PZTV), Nb *4d* states in Nb-doped PZT (PZTN), Ta *5d* states in Ta-doped PZT (PZTT), Mo *4d* states in Mo-doped PZT (PZTM), and W *5d* states in W-doped PZT (PZTW) also contribute to the CBM. These *d* states of dopants are recognized to share the remaining electrons released by oxygen vacancies with the Ti *3d* orbitals [41, 42]. Thus fewer Ti *3d* states are occupied, and the π bonds between the Ti and O are maintained. Therefore, these substituted systems may be less susceptible to ferroelectric fatigue.

6.5 A-site Donor Substituted $Pb(Zr_xTi_{1-x})O_3$

6.5.1 Group VB Elements (Sb^{3+}, Bi^{3+})

The DOS of the PZT systems substituted by the group VB elements at A-site are shown in Fig. 6.3. Aliovalent Bi substituted PZT and aliovalent Sb substituted PZT have similar conduction band structure to that of undoped PZT. Moreover, the DOS results are even identical to those of PZT systems substituted by group VB elements (Bi, Sb) at B-site. The energy states of Bi ions (Bi *6s*) are mainly located at 10 eV below the Fermi level, and those of Sb ions (Sb *5s*) at around 8 eV below Fermi level. As the substitution of Bi and Sb has little effect on the electronic structure of the conduction band minima (CBM) of the PZT system, these two systems remain charge-transfer insulators.

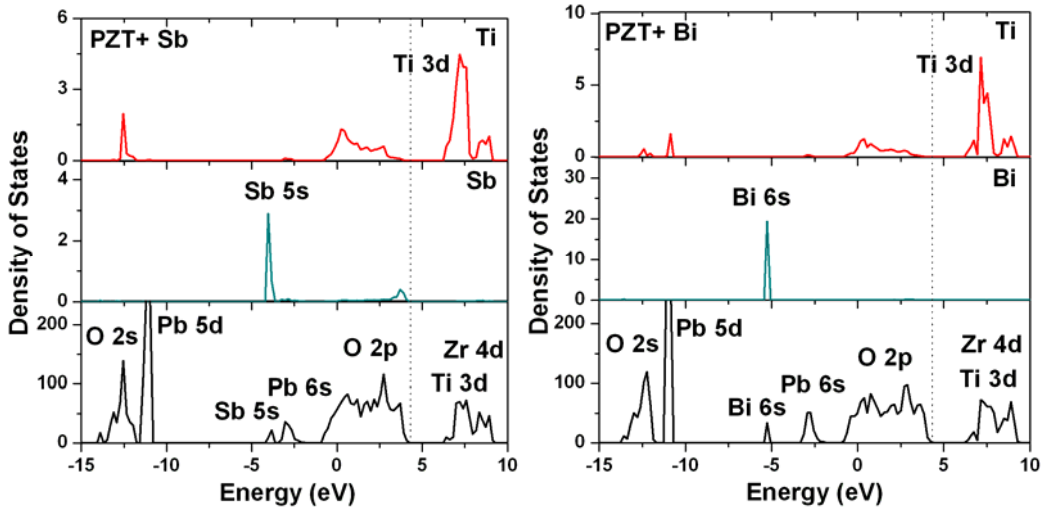

(a) (b)

Figure 6.3: Calculated DOS and PDOS of the PZT systems with (a) Sb substitution and (b) Bi substitution.

Theoretical studies have shown that the possible origin of the fatigue is associated with the reduced π bonds between Ti *3d* and O *2p* states caused by remaining electrons released from oxygen vacancies [17]. While the stability of ferroelectricity is closely related to the magnitude of these bonds [73, 92, 118, 119], the occupation of Ti *3d* states by the electrons is detrimental to the bonding. As the CBMs of the Bi-substituted and Sb-substituted PZT are still dominated by the Ti *3d* states, the electrons released from oxygen vacancies could accordingly occupy the Ti *3d* states and reduce the π bonds between Ti *3d* and O *2p* as in the undoped PZT. Considering our previous results for the group VB elements (Bi, Sb) as the B-site substitutions, we conclude that the group VB substitutions (Bi, Sb) do not relieve the fatigue problems of PZT, regardless of their site occupancy.

Moreover, it is also interesting to observe that the energy and optical band gap of the substituted systems are reduced with the increased atomic number of the dopants for group VB trivalent A-site substitutions. For these systems, the band gaps have charge-transfer gaps between occupied O *2p* valence band and unoccupied Ti *3d* conduction band, as shown in Fig. 6.4(b). The Ti *3d* bandwidth (W) is closely related to the ionic size of the A-site cation, since the ionic size of the A-site cation mediates the Ti-O-Ti bond angle. As the size of A-site cation decreases, the Ti-O-Ti bond angle bends and deviated from 180° (the angle is calculated to be 164.5° in pure PZT system, 157.4° in Bi-doped PZT system and 155.7° in Sb-doped PZT system), resulting in a narrower electronic bandwidth (W) and accordingly broader band gaps.

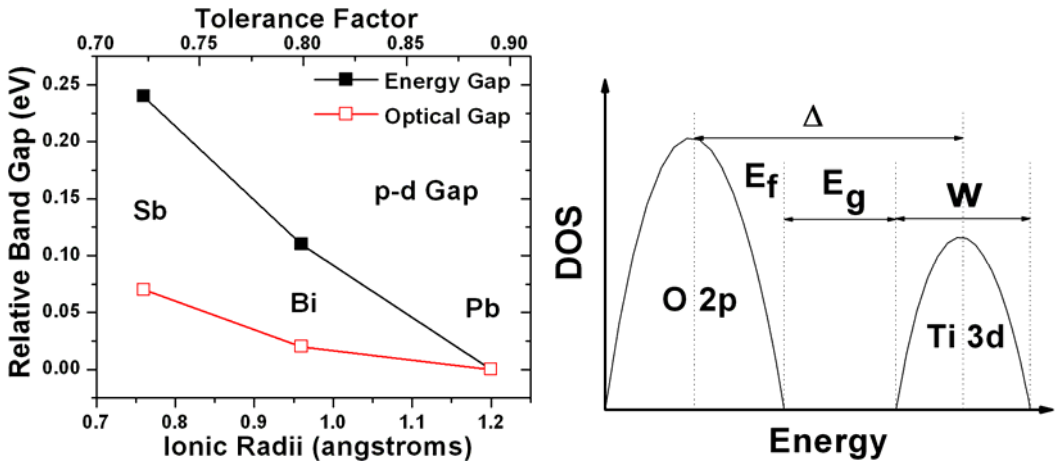

(a) (b)

Figure 6.4: (a) Calculated variations of energy band gaps and optical band gaps of PZT with group VB substitutes and (b) Schematic density of states of PZT systems with group VB substitutes. E_f denotes the Fermi energy. Δ is the energy difference between filled O *2p* bands and unoccupied Ti *3d* band. W is one-electron band width of Ti *3d* states.

6.5.2. Group IIIA Elements (Sc^{3+}, Y^{3+}, La^{3+})

For the group IIIA element substituted systems, the CBMs consist of both dopants' states and Ti *3d* states; La *4f* states, Sc *3d* states and Y *4d* states also contribute to the CBM in respective system (Figure 6.5). These donor states share the remaining electrons at the CBMs released by oxygen vacancies with the Ti *3d* orbitals. With fewer occupied Ti *3d* states and therefore less reduced π bonding, the La-, Sc- and Y-substituted systems are less susceptible to ferroelectric fatigue [41, 42].

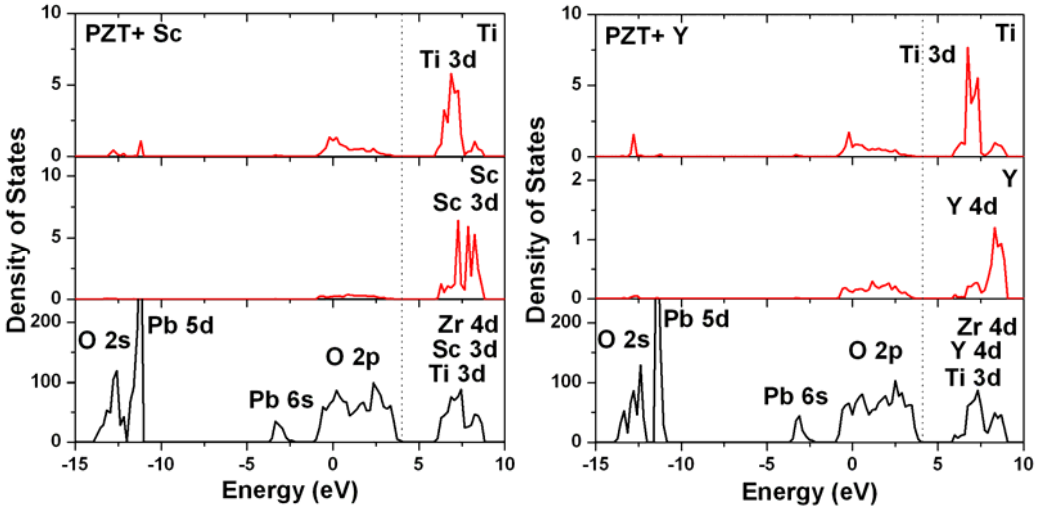

(a) (b)

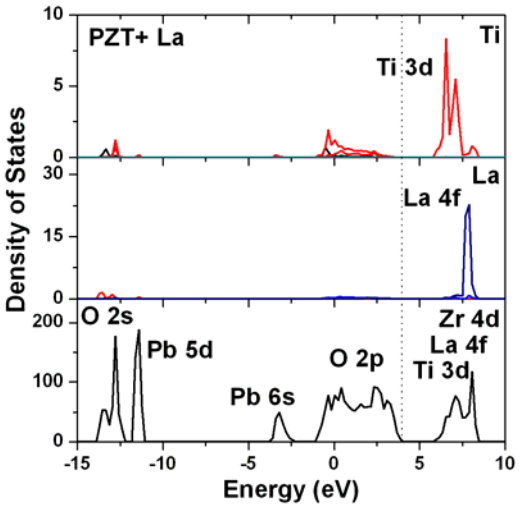

(c)

Figure 6.5: Calculated density of states (DOS) and partial density of states (PDOS) of the PZT systems with (a) Sc substitution, (b) Y substitution, and (c) La substitution.

Moreover, the correlation between electrons introduced into PZT by the group IIIA trivalent cations introduce impurity electron band with intensive Ti *3d* states in the band gap, consistent with a Mott-Hubbard description of the transition metal compound in Zaanen, Sawatzky, and Allen (ZSA) framework (Figure 6.6a) [132]. The substituted PZT systems are no longer rigidly charge-transfer insulators and the character of Mott-Hubbard band gap appears more dominant with increased substitution level until a pure Mott-Hubbard insulator is achieved at full substitution of A-site cations by the substitutions. This effect of substitution in PZT is similar to the situation observed in the La- or Y-doped $BaTiO_3$ and $SrTiO_3$ systems [133, 134].

The calculated shift of energy and optical band gaps of the group IIIA elements substituted PZT systems are summarized in Fig. 6.6. The chemical trend of the optical

band gaps by the substitution is consistent with that of energy band gaps, which also agrees well with available experiments.[27] Similar to the chemical trends of group VB trivalent substitutions, a reduction of both energy and optical band gap of the doped systems with increased atomic number of the for group IIIA trivalent dopants was observed.

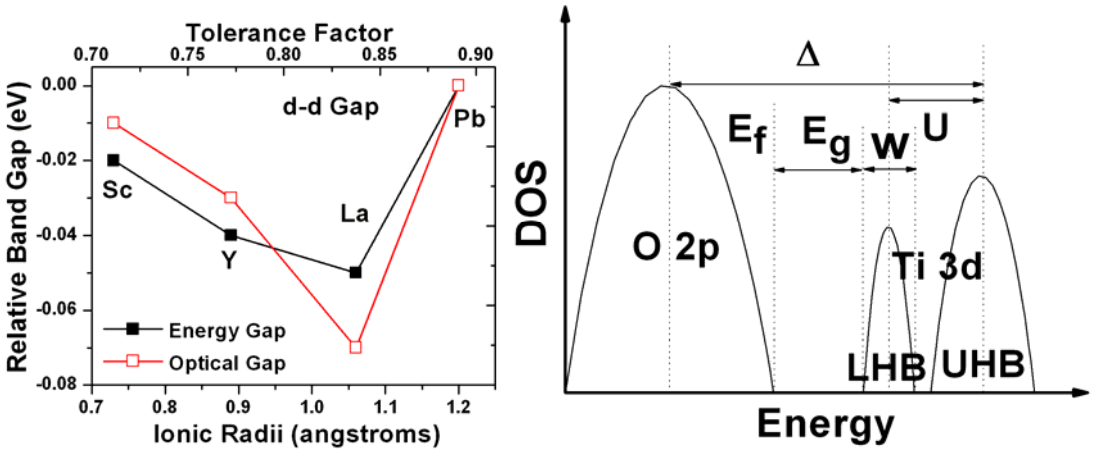

(a) (b)

Figure 6.6: (a) Calculated shift of energy band gaps and optical band gaps of PZT with group IIIA dopants. (b) Schematic density of states of PZT systems with Group IIIA dopants. LHB is the lower Hubbard band, and UHB is the upper Hubbard band. E_f denotes the Fermi energy. Δ is the energy difference between filled O *2p* bands and unoccupied Ti *3d* band. W is one-electron band width of Ti *3d* lower Hubbard band.

As mentioned earlier, substitution of group IIIA dopants Sc^{3+}, Y^{3+}, and La^{3+} for Pb^{2+} introduces an impurity band in the PZT band gap, leading to the reduction of the band gap with respect to pure PZT. This mid-bandgap impurity band is ascribed to a lower Hubbard band (LHB) associated with Ti *3d* electrons. The splitting of the lower Hubbard

band from the upper Hubbard band (UHB) is due to the correlation between electrons introduced into PZT by the group IIIA trivalent cations. On the other hand, the systematic reduction of band gaps with the increased atomic number of group IIIA dopants is associated with the Ti *3d* t_{2g} electron bandwidth (W). Ti *3d* electron transfer in titanium oxides is governed by the supertransfer process mediated by the O *2p* states rather than the direct transfer between the *3d* states.[28] The Ti-O-Ti bonding angle deviates more and more from 180°, as the ionic size decreases with the atomic number of group IIIA substitutions (161.4°, 157.5°, 156.1° for La, Y and Sc, respectively, substituted PZT systems from our calculations). Accordingly, the electron bandwidth (W) becomes smaller, and the band gap energy increases, while atomic number of group IIIA substitutions decreases.

6.6 Formation Energy of Oxygen Vacancies

The formation energies (E_f) of the neutral oxygen vacancies in the substituted and pure PZT systems were also calculated (Table 1) based on Eq.(5-3). The formation energy of oxygen vacancies in Pb-deficient PZT could be as low as −3.80 eV, as shown in Table 6.1. Accordingly, a large number of Pb-O Schottky vacancy pairs exist in the PZT lattice. Poykko and Chadi found that these Schottky vacancy pairs are not closely bound. As oxygen vacancies have a strong mobility, they could easily migrate to the electrode interfaces, or form oxygen vacancy planes to pin the domain walls [95].

Our results on donor substituted PZT show that all the substituted systems have relatively higher formation energy of oxygen indicating that donor substitution can better stabilize the oxygen in Pb-deficient situations than PZT, no matter they are A-site or B-site dopants. However, of all the B-site donor substituted systems, the formation energies in V/Mo/Bi/Sb-doped PZT systems are still negative and lower than that in defect-free PZT. Only three systems (Nb, Ta, and W) have comparable formation energies as that of defect-free PZT, even in Pb deficient in these systems. In contrast, our calculated results on the A-site donor substituted systems have even higher formation energy of oxygen vacancy than pure PZT. This effective reduction of oxygen vacancy concentration by the substitution of Pb^{2+} ions results in the softening of a large number of ferroelectric properties in PZT including relieved fatigue, enhanced dielectric constant, reduced coercive field and increased remnant polarization.

Table 6.1 Calculated formation energy of oxygen vacancies in pure PZT, Pb-deficient PZT and A-site substituted PZT systems under oxygen rich conditions, where the chemical potential of oxygen in oxygen-rich condition was determined by considering the isolated oxygen molecular with a bonding length of 1.21 Å.

	Undoped		A-site					B-site						
			Group IIIA			Group VB		Group VA			Group VIA		Group VB	
Dopants	Pure	Pb-deficient	Sc	Y	La	Sb	Bi	V	Nb	Ta	Mo	W	Bi	Sb
Formation Energy (eV)	0.37	-3.80	0.39	0.45	0.41	0.54	0.40	-0.45	0.72	0.93	-0.26	0.33	-3.62	-1.53

6.7 Summary

A first-principles density functional theory study of the electronic structures, optical behaviors, vacancy formations, and fatigue behaviors in donor-substituted lead zirconate titanate was conducted. The role of the substitution is discussed and the mechanisms of the substitution behavior are suggested.

(1) For B-site donors, we find that the Nb, Ta, and W-doped PZT systems have the highest oxygen vacancy formation energy and least occupied Ti 3d states at CBM by electrons. Therefore, high fatigue resistance can be expected in these three systems. Sb and Bi-doped systems have relatively large oxygen vacancy concentrations, and the π bonds between Ti ions and O ions in these systems will be weakened once electrons are released. Improvement of fatigue behavior cannot be expected in these systems. Our conclusion on Nb, Ta, W, and Sb doped systems is confirmed experimentally [21, 24, 25, 33, 64, 65]. It is also worth mentioning that although Mo and V-doped PZT systems also have fewer occupied Ti 3d states, their oxygen formation energies are lower than those of Nb, Ta, and W doped systems, which restrict their effectiveness in improving the fatigue.

(2) For A-site donors, it is found that all the substitutions are found to effectively dilute the concentration of the oxygen vacancies by releasing two electrons to compensate the holes in Pb-deficient lattice, leading to the softening of the ferroelectric properties of PZT. Moreover, the conduction bands in the group IIIA element (Sc^{3+}, Y^{3+}, La^{3+})

substituted PZT systems are shared by Ti 3*d* and dopant states. These unique band structures lead to a reduced occupation on Ti 3*d* by the electrons released from oxygen vacancies, which makes them less susceptible to fatigue. On the other hand, group VB elements substituted (Bi, Sb) either as trivalent *A*-site donors or as pentavalent *B*-site donors fail to relieve the fatigue of PZT systems due to the lack of dopant states at the CMB of respective system.

(3) The systematical shift of both energy and optical bandgap with atomic number of the dopant is closely related to the character of the band gaps and the electron bandwidth of Ti 3*d* states. Group VB trivalent substitutions do not change the character of the band gap of the charge-transfer insulator PZT, and their ionic sizes determine the electron bandwidth of Ti 3*d* states and the band gap. Group IIIA trivalent dopants, however, introduce impurity band with Mott-Hubbard character into the PZT band gap, leading to a reduction of band gap compared with that of pure PZT. The systematic shift of the band gap can be explained by the changes of LHB mediated by the ionic size of group IIIA substitutions.

Chapter VII

Acceptors Substituted Lead Zirconate Titanate

Materials in this chapter have been published in Applied Physics Letters (Volume 92, Page 112909), and Functional Materials Letters (In press). They are reproduced with permission of American Institute of Physics and World Scientific.

While we study the donor substitutions in Chapter VI, in this chapter, we study the defect structures in acceptor substituted lead zirocnate titanate, which is key to understand the substitution effects. We find that the preferences of the acceptors to form certain defect structures with the oxygen vacancies determine their effects on the ferroelectricity of the lead zirconate titanate system.

7.1 Introduction

As many species of the donors have been intensively investigated both experimentally and theoretically [19-25, 31-33, 35, 36, 58-61], the results on the acceptors lack much attention, as they are generally believed to create the unwelcomed oxygen vacancies in lead titanate. However, the research on the acceptor substituted lead titanate has become a hot topic recently as unique mechanisms governing the substitution effects were found that are contrary to the common belief [26-30, 34, 37, 62, 63]. Specifically, aliovalent *3d* transition metal (TM) acceptor substitutions at B-site have been intensively studied. Zhang and Whatmore proposed a dipole model for Mn-doped lead zirconate titanate (PZT), pointing out that the associated clusters between the oxygen vacancies and the acceptors reduces the mobility of oxygen vacancies [26]. This model is supported by the microscopic investigations of Fe-doped $PbTiO_3$ by Mestric *et al*., which have been experimentally identified as well as theoretically confirmed by the existence of associated clusters [27-30, 34, 37, 120].

Therefore in this chapter, we use computation to look into the defect and electronic structures in $PbTiO_3$ with various diluted concentrations of acceptors. By analyzing the energetics of various configurations, we firstly envisage the picture of the defect structures in lead titanate under numerous acceptor substitution conditions, where an oxygen vacancy is induced by the dopants in order to maintain local electro-neutrality. Moreover, by examining the density of states, we aim to understand the different electronic structures in ferroelectric perovskites with different elements. The effects of

the defect and electronic structures on the ferroelectricity of the $PbTiO_3$ are also discussed in detail. We hope that this work will help identify the valuable mechanisms of element substitution modulated defect structure and ferroelectric ordering in acceptor substituted lead titanate.

7.2 Calculation Methodology

We exhaustively investigate the aliovalent acceptors by screening group IIIB, group VB elements, and *3d* transition metal elements (A^{3+}) as dopants at the Ti site in $PbTiO_3$. The ionic radii of aliovalent group IIIB elements (Al, Ga, In, and Tl), group VB elements (Sb and Bi), and *3d* transition metals (Cr, Mn, Fe) are 0.51, 0.62, 0.81, 0.95, 0.76, 0.96, 0.63, 0.66, and 0.64 Å, respectively. The tolerance factor, which was introduced by Goldschmidt [116], is calculated for each $PbAO_3$ system with full Ti-site substitution by the acceptors, and is in the relatively stable range (0.78 – 0.97) of perovskites.

In order to accommodate two acceptors substituting at the Ti sites and one oxygen vacancy, a number of $3\times3\times3$ supercells are constructed. The larger supercell is necessary to reduce the interactions between the defects and their images. Various defect structures are considered for each acceptor-substituted $PbTiO_3$. In each defect structure, one oxygen atom is removed from the lattice in order to maintain local the electroneutrality, which might be previously bonded with the Ti ions in the *xy* plane, or along the *z* direction. The defect structures of the acceptor dopants with respect to the oxygen vacancy are considered as follows: (1) the dopants and the oxygen vacancy form

a defect cluster ($A'_{Ti} - V_O^{\bullet\bullet} - A'_{Ti}$); (2) one dopant forms a defect pair with oxygen vacancy ($A'_{Ti} - V_O^{\bullet\bullet}$), the other is isolated (A'_{Ti}); and (3) all the defects are isolated (A'_{Ti} , $V_O^{\bullet\bullet}$, A'_{Ti}).

First-principle density functional theory (DFT) calculations with local density approximations are performed to optimize the ionic and electronic structures of the substituted lead titanate. The pseudopotential approach with the projector-augmented wave formalism is adopted. Pb *5d*, *6s*, *6p*, O *2s*, *2p*, Ti *3d*, *4s*, group IIIB and VB substitutes outermost *s*, *p*, *d* orbitals (*3s*, *3p* only for Al), and TM *3d*, *4s* orbital are regarded as valence orbitals. A $1\times1\times1$ Monkhorst–Pack grid and a cutoff energy of 400 eV are employed for all the supercells. The structure optimizations are performed with experimental lattice parameters (a=b=3.904 Å and c/a=1.063) of the lead titanate [106]using the Vienna *ab-initio* simulation package (VASP) [69].

7.3 Defect Structures

7.3.1 Isolated Defects: Cr Substitution

Three isolated point defects are the most energetically favorable arrangement for Cr-substituted $PbTiO_3$, where the Cr substitutes and the oxygen vacancy prefer not to stay in the nearest neighbor positions of each other. Two important characteristics are worthy of highlighting in this isolated-point-defect structure.

First, a close examination of the atomic relaxations for the Cr substituted system

reveals that the cations neare to the oxygen vacancy are displaced away from the vacancy, compared with the pure $PbTiO_3$ lattice free of oxygen vacancies (Figure 7.1a). It is very similar to the microscopic configuration that has been observed by the previous studies on oxygen deficient pure lead titanate [27, 37, 48]. The displacement resulting from the Coulomb interaction between the oxygen vacancy and the cations, leads to a shortened bond between the neighboring Ti atom and the uppermost oxygen atom in Fig.7.1b. The bond lengths between Ti ion and uppermost O ion are 1.80 Å in oxygen-deficient $PbTiO_3$ and 2.36 Å in pure $PbTiO_3$ systems, indicating a strong hybridization between and a defect-induced polarization change. It is noteworthy that atomic relaxation gives rise to a tail-to-tail polarization pattern around the vacancy, which effectively pins the domain walls as pointed out by Park and Chadi [48]. The pinning effect can be quite strong, as the high mobility of the oxygen vacancies makes them agglomerate in planes, leading to fatigue. This mechanism deduced from the pure oxygen deficient lead titanate is significant in the Cr-substituted $PbTiO_3$ as well, where defects are free and isolated, and the bond lengths between Ti ions and uppermost O ions are seldom changed by the Cr substitution.

Second, it is found that Coulomb repulsive interaction between negatively charged Cr dopant (Cr'_{Ti}) and surrounding ions in the Cr-containing octahaedra increases the bond length between Cr and O ions (Figure 7.1c), indicating that the hybridization is weaker. This weakened hybridization induces the shortened displacement and reduced polarization, as a strong hybridization is necessary to stabilize the ionic displacement in lead titanate and lead to the ferroelectricity [67, 79].

To summarize, Cr substitution cannot relieve domain wall pinning effects caused by the oxygen vacancy, it also further deteriorates the ferroelectricity due to the weaker hybridization between Cr and oxygen ions. This defect structure is consistent with experimental observations on Cr-doped PZT systems [121, 122]

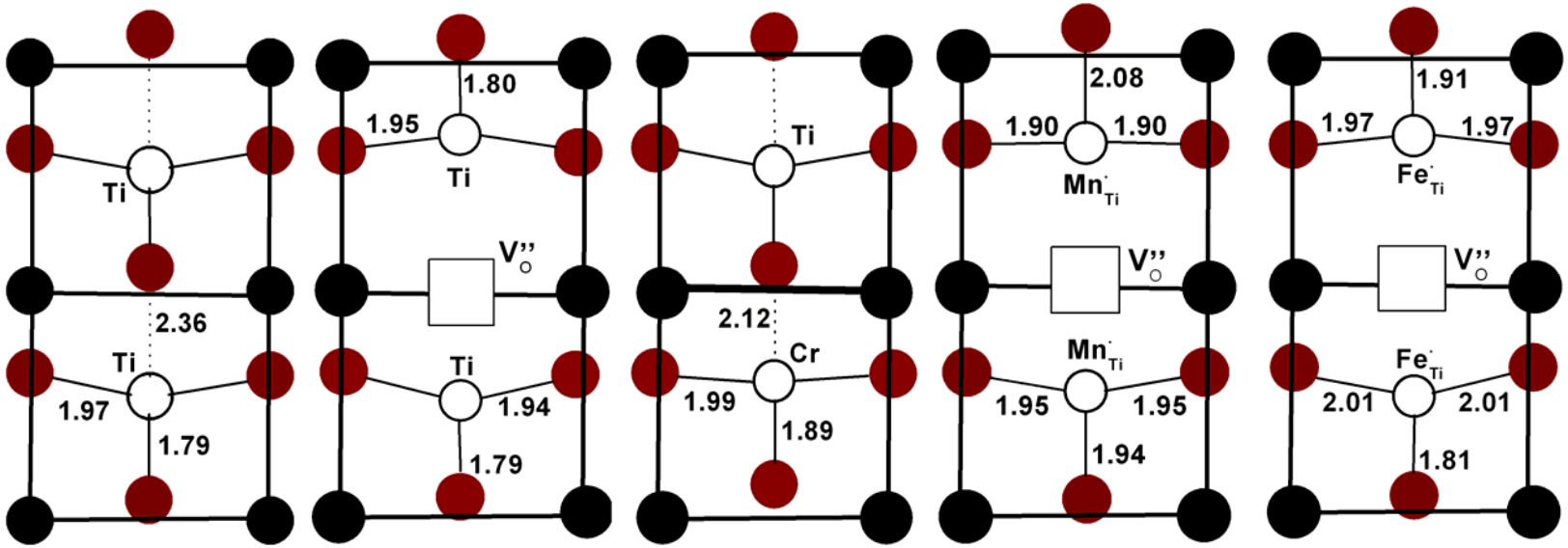

Figure 7.1: Schematic atomic structures for (a) pure $PbTiO_3$, (b) oxygen-deficient $PbTiO_3$, (c) Cr-substituted $PbTiO_3$, (d) Mn-substituted PbTiO3, and (e) Fe-substituted $PbTiO_3$. The numbers given indicate the respective bond length in Å. The black solid circles are Pb atoms, red solid circles represent O atoms, the open circles stand for B-site atoms, and open squares are oxygen vacancies.

7.3.2 Defect Cluster along *z* Direction: Group IIIB (Al, Ga, In, Tl) and *3d* Transition Metal (Mn, Fe) Substitution

Comparing the energetics of the optimized lead titanate with different defect structures, we find that the group IIIB (Al, Ga, In, Tl) and the transition metal (Mn, Fe) doping preferentially forms defect clusters along z direction in the lead titanate lattice, where two substitutions are located at nearest-neighbor Ti sites along *z* direction and the oxygen vacancy is centered between the dopants, which agrees well with earlier studies on the Fe-doped $PbTiO_3$ [27, 28, 30, 37, 122]. The important characteristics of this defect structure are described below.

First, in these defect structures, the oxygen vacancies are tightly bound with the acceptors by the Coulomb interactions between them, where partial charge compensation occurs. Therefore, as a whole, the clusters are much more immobile than isolated free defects and, hence, the migrations and agglomerations of oxygen vacancy are effectively hindered.

Second, compared with the oxygen-deficient lead titanate without any substitution, the atomic displacements are smaller within $A'_{Ti} - V_O^{\bullet\bullet} - A'_{Ti}$ defect cluster structures, due to the stronger Coulomb attractive interaction between the positively charged oxygen vacancy ($V_O^{\bullet\bullet}$) and negatively charged dopants (A'_{Ti}). The bond lengths between Ti ions and uppermost O ions are increased, respectively, to 1.82, 1.90, 2.09, and 2.31 from 1.80 Å by Al, Ga, In, and Tl substitutions, as indicated in Fig. 7.2. As this bonding is

weakened, the tail-to-tail polarization pattern is weakened and, therefore, the local pinning effects are slightly relieved by the group IIIB elements substitution.

In summary, the defect cluster relieves the space charge effects by constraining the oxygen vacancy motion, as well as alleviates the domain pinning effect by relaxing the tail-to-tail polarization pattern.

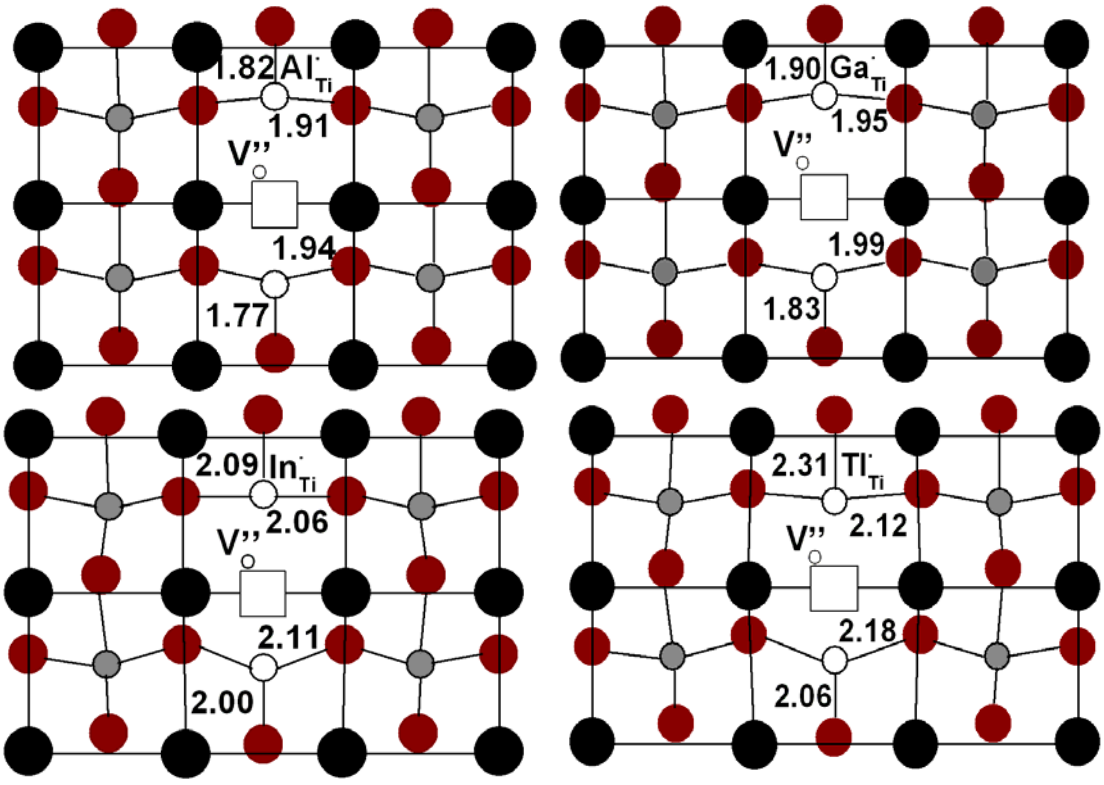

Figure 7.2: Schematic atomic structures for (a) Al-substituted $PbTiO_3$, (b) Ga-substituted $PbTiO_3$, (c) In-substituted $PbTiO_3$, and (d) Cr-substituted $PbTiO_3$. The numbers given indicate the respective bond length in Å.

7.3.3 Defect Cluster in xy-plane: Group VB elements (Bi, Sb) Substitution

The remarkable finding for group VB substitutions is that they favor defect clusters lying in the *xy* plane (Figure 7.3), indicating that these dopants stabilize the oxygen atoms along the *z* direction at the cost of losing oxygen in *xy* planes. As a defect cluster, this structure still suppresses the space charge effects in a similar way discussed previously. Moreover, the defect clusters induce the head-to-head polarization patterns, which are normal to the bulk polarizations (like a 90° domain wall). Contrary to the significant pinning effect of 180° domain walls, these 90° domain-wall-like structures can effectively respond to the applied electric field [14]. Therefore, the domain wall pinning effects of oxygen vacancies are further diminished by group VB substitutions, compared with group IIIB elements.

Moreover, we find that the preference of the defect structures by different groups of elements is believed to be associated with the ionic sizes and the electronegativities of the dopants. As shown in Table 7.1, dopants with higher electronegativities (thus, closer to that of oxygen) and larger ionic sizes favor the formation of the defect cluster in the xy plane, whereas smaller ionic size and electronegativity of the substitution create the cluster along z direction. The exception to this rule is Cr, with fairly low electronegativity and small ionic radius, which prefers isolated point defects structure.

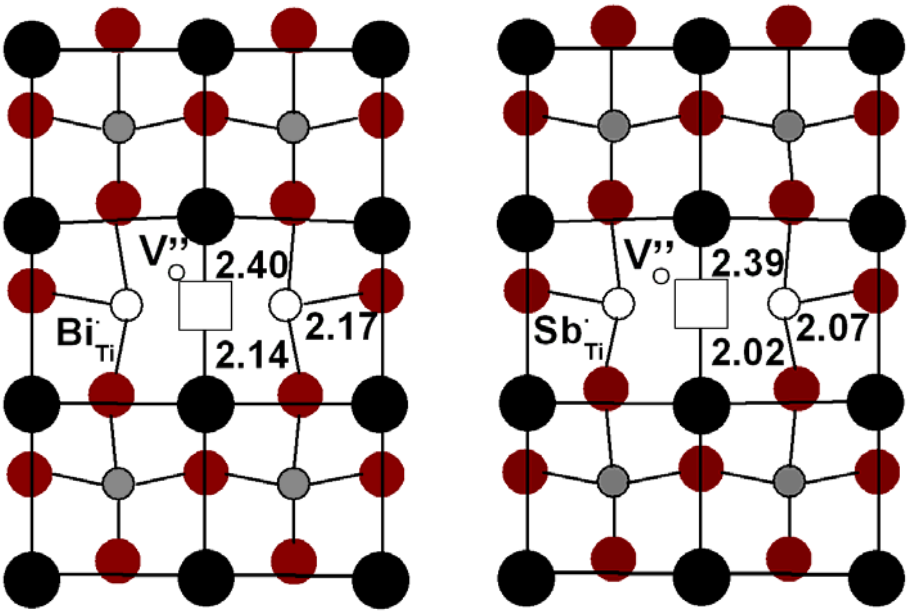

Figure 7.3: Schematic atomic structures for (a) Bi-substituted $PbTiO_3$, (b) Sb-substituted $PbTiO_3$. The numbers given indicate the respective bond length in Å.

The reason behind this exception is that the lattice relaxation and the effective charge are two important factors in determining the binding energies of defect clusters. When the effective charge is kept constant, the variation of binding energy is mainly attributable to the various relaxations of the lattice around the defect. In the PbTiO3 system, Cr leads to a larger displacement than Fe in the defect cluster, therefore, the binding energy is decreased. On the other hand, when the effective dopant charge decreases, the binding energy is strongly decreased; this is largely due to the electrostatic interaction. Take Al and Cr substitutions for instance, their substitutions result in similar relaxations in the defect cluster but the effective dopants charge of Cr is lower (as we will see in fig. 4). We conclude that Cr substitutions lead to the large relaxation as well as the low effective charge in defect clusters structure, which makes the cluster unstable.

Table 7.1: The calculated bond lengths and defect structures of pure, oxygen deficient, 3d transition metal elements substituted, group IIIB elements substituted, and group VB elements substituted $PbTiO_3$. The electronegativities and ionic radii of the dopants are found to determine their defect structure. $\Delta b_{z\text{-}1}$, $\Delta b_{xy\text{-}1}$, $\Delta b_{z\text{-}2}$, and $\Delta b_{xy\text{-}2}$ respectively indicate the difference in the bond length of each bond with respect to the oxygen deficient $PbTiO_3$. In oxygen deficient $PbTiO_3$, $b_{z\text{-}1}$, $b_{xy\text{-}1}$, $b_{z\text{-}2}$, and $b_{xy\text{-}2}$ are 1.80, 1.95, 1.79 and 1.94 Å, respectively.

		$\Delta b_{z\text{-}1}$ (Å)	$\Delta b_{z\text{-}2}$ (Å)	$\Delta b_{xy\text{-}1}$ (Å)	$\Delta b_{xy\text{-}2}$ (Å)	Defect Structure	Electronegativity	Ionic Radius (Å)
No Substitution	Ti (With V_O)	0	0	0	0	/	1.54	0.68
	Ti (Without V_O)	0.56	0.00	0.02	0.03	/	1.54	0.68
3d Transition Metal	Cr	/	0.10	/	0.05	*Isolated Point Defects*	1.66	0.63
	Mn	0.28	0.15	-0.05	0.01	*Cluster Along z*	1.55	0.66
	Fe	0.11	0.02	0.02	0.07	*Cluster Along z*	1.83	0.64
Group IIIB Elements	Al	0.02	-0.02	-0.04	0.00	*Cluster Along z*	1.61	0.51
	Ga	0.10	0.04	0.00	0.05	*Cluster Along z*	1.81	0.62
	In	0.29	0.21	0.11	0.17	*Cluster Along z*	1.78	0.81
	Tl	0.51	0.17	0.17	0.24	*Cluster Along z*	1.62	0.95
Group VB Elements	Sb	0.59	0.23	0.12	/	*Cluster In xy*	2.05	0.76
	Bi	0.60	0.35	0.22	/	*Cluster In xy*	2.02	0.96

7.4 Electronic Structures

The densities of states (DOS) of the optimized *3d* TM substituted lead titanate configurations (Figure 7.4) reveals that TM *3d* levels are introduced above the valence band maxima (VBM) into the energy gaps by the TM substitution. Furthermore, strong hybridization between O 2p and TM 3d electrons can be observed in the valence band and conduction band, indicating formation of A–O bonds, as shown in Figs 7.1d and 7.1e. The TM 3d states are also important to absorb the remaining electrons in lead titanate, in a similar way as in the donors substituted $PbTiO_3$. Once these electrons are released (by the formation of oxygen vacancies or electron injection from the electrodes), they occupy the TM 3d states rather than the Ti 3d states at VBM, and hence maintain the π bonds between Ti 3d and O 2p [35, 36].

In comparison, for group IIIB and group VB elements substituted lead titanate, the densities of states (DOS) reveal that the conduction bands and valence bands of acceptor substituted $PbTiO_3$ are almost unchanged with respect to that of pure lead titanate. Weak hybridizations between O 2p and TM 3d electrons can be observed in the valence band and conduction bands. However, this bonding is not very strong as the main peaks of the group IIIB and the group VB dopants are located below valence band (5 and 10 eV below the Fermi level, respectively), as shown in Figure 7.4. However, the mechanism for ferroelectricity enhancement for the donors does not hold in the group IIIB and VB acceptors substituted lead titanates.

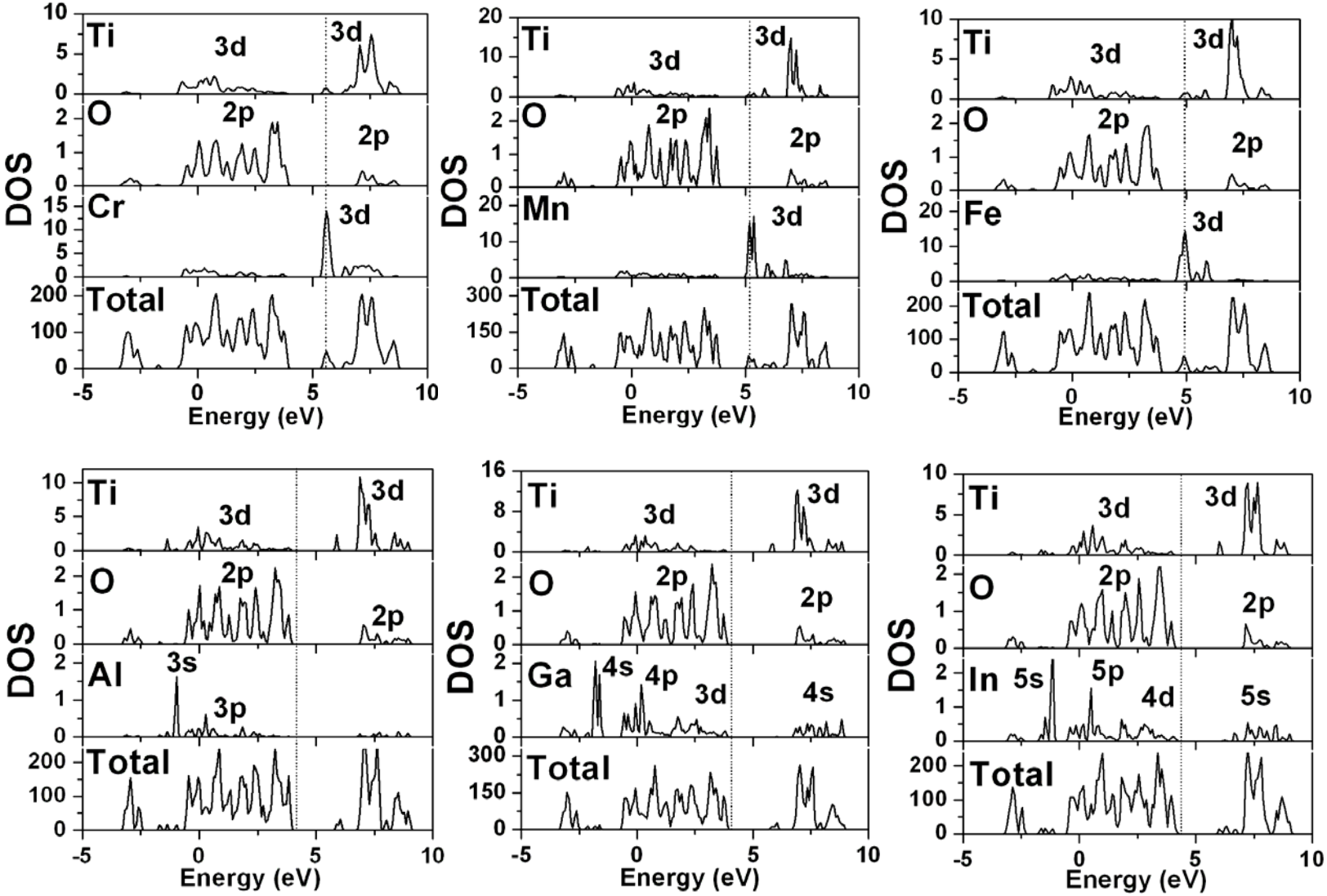
DOS
Ti
3d
3d
O
2p
2p
Cr
3d
Total
Energy (eV)
DOS
Ti
3d
3d
O
2p
2p
Mn
3d
Total
Energy (eV)
DOS
Ti
3d
3d
O
2p
2p
Fe
3d
Total
Energy (eV)
DOS
Ti
3d
3d
O
2p
2p
Al
3s
3p
Total
Energy (eV)
DOS
Ti
3d
3d
O
2p
2p
Ga
4s
4p
3d
4s
Total
Energy (eV)
DOS
Ti
3d
3d
O
2p
2p
In
5s
5p
4d
5s
Total
Energy (eV)

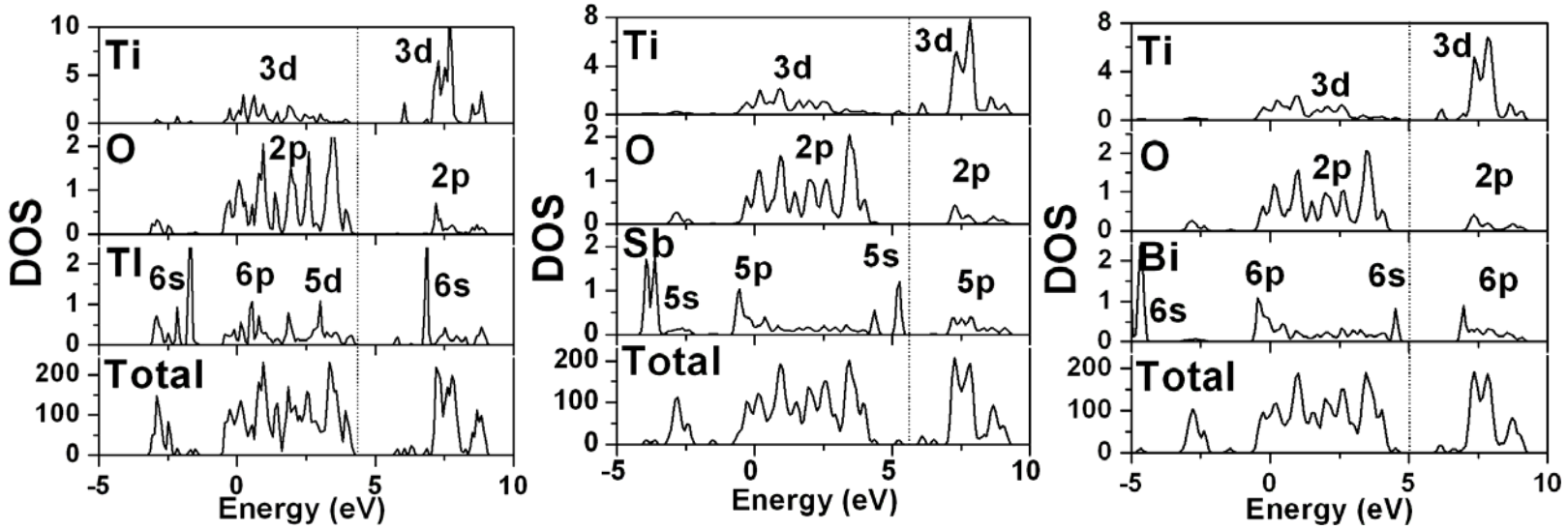

Figure 7.4: Total and partial density of states (DOS) for acceptor-doped $PbTiO_3$ systems in their groundstates.

7.5 Summary

We conclude that the improved ferroelectric behavior experimentally observed from the group IIIB and VB elements substituted PZT are closely associated with the immobile $A'_{Ti} - V_O^{\bullet\bullet} - A'_{Ti}$ defect clusters, which greatly reduces the mobility of oxygen vacancies and weakens the space charge effects. Moreover, it is noteworthy that the group IIIB dopants relieve the tail-to-tail polarization patterns, diminishing the domain wall pinning effects. Froup VB substitutions, however, prefer a different defect cluster structure, where the cluster lies in the xy plane. The structure induces a head-to-head polarization pattern normal to the bulk polarization, which makes the domain pinning effect of oxygen vacancy to the lattice even weaker. The preference of the orientation of the defects in the clusters is believed to be associated with the ionic size and the electronegativity of the substitution.

Chapter VIII

Realization of Degradation Improved Lead Zirconate Titanate: Experimental Approaches

Materials in this chapter have been published in Journal of Applied Physics (Volume 102, Page 074119). They are reproduced with permission of American Institute of Physics.

Following our theoretical studies, we carried out experimental studies on the degradation enhanced lead zirconate titanate using pulse laser deposition (PLD) technique. By examining the microstrcutures and ferroelectric properties of W-substituted and pure lead zirconate titanate thin film samples, we conclude that the experimental results are consistent with our theoretical predictions.

8.1 Introduction

Our theoretical calculations and analysis have shown that elemental substitution can be an effective way to improve the fatigue behavior of PZT films. Many dopants have been developed for PZT [19-26, 31-34, 58-63]. Particularly, donor dopants in PZT have been found to enhance the dielectric constants, increase the bulk resistivity, reduce the coercive field, as well as improve the fatigue property of PZT [19-25, 31-33, 58-61]. As discussed in the previous chapters, the reduced susceptibility to fatigue of the donor substituted PZT is believed to be caused by the reduction in oxygen vacancy concentration, as well as the reduced occupation of Ti *3d* states by the electrons with the help of donor states such as the Nb *4d* and the La *4f* states. In addition, modification of the electrodes has been proposed to overcome the fatigue problem in PZT. When oxide or hybrid-metal-oxide electrodes, such as $LaNiO_3$ (LNO), (La, Sr)CoO_3 (LSCO), RuO_2, and IrO_2, are used to replace the Pt electrode, the fatigue can be reduced by the fact that these oxides can reduce or reoxidize reversibly and repeatedly without degradation [18, 52-56].

In this part of the thesis, we follow the theoretical calculations with experimental studies on the ferroelectricity of the W doped $Pb(Zr_xTi_{1-x})O_3$ to verify the theoretical predictions. We study the microstructure, ferroelectric properties, and fatigue behavior of doped PZT thin films deposited by pulsed laser ablation on $LaNiO_3$ bottom electrodes.

8.2 Experimental Procedure

The nominal chemical composition of pure PZT in this study is $PbZr_{0.3}Ti_{0.7}O_3$. Two batches of ceramics, undoped (PZT) and 1 mol % W-doped PZT (PZTW), are fabricated by conventional solid state reaction, in which 30 mol % of excess PbO powder are added in order to compensate the Pb loss during calcination, sintering, and film deposition. A KrF excimer laser (λ=248 nm, pulse width=25 ns) is used in the laser ablation process. The target-substrate distance is kept at 45 mm during deposition. The laser ablation is carried out at a laser fluence of 2.5×10^{-2} J/mm^2 and a repetition rate of 5 Hz. The LNO film acting as bottom electrode and template is first deposited on SiO_2 /Si substrate at an oxygen partial pressure of 50 mTorr and at a substrate temperature of 873 K. The PZT and PZTW films with the thickness of about 150 nm are then deposited on LNO/SiO_2 /Si in an oxygen partial pressure of 300 mTorr and at a substrate temperature of 873 K. After the deposition, the films are naturally cooled down in the oxygen partial pressure of 300 mTorr.

Structures of the PZT and PZTW thin films are characterized using a Shimadzu XRD-7000 diffractometer with Cu Kα radiation. Microstructures of the thin films are examined using a Hitachi S-4100 field emission scanning electron microscopy (FESEM). Secondary ion mass spectrometry (SIMS) depth profiles of the films are measured on Cameca IMS-*6f* Magnetic SIMS using an oxygen ions source. X-ray photoelectron spectra (XPS) are performed using a VG Escalab MKII spectrometer with an Al x-ray source (1486.6 eV). An analyzer with pass energy of 200 eV is adopted and C *1s* peak at

284.6 eV from adventitious carbon is used as an internal reference. The ferroelectric and fatigue properties are measured using a Radiant Precision Workstation with an electrical field of 120 kV/cm.

8.3 Effects on Microstructures

Figure 8.1 shows the θ-2θ XRD scans of the PZT/LNO and PZTW/LNO heterostructures. Except for the (100), (200), and (110) peaks, no peaks from the harmful pyrochlore phase or any other secondary phase in PZT and PZTW films can be seen, indicating both thin films have typical tetragonal perovskite structures. The strong (100) diffraction of the undoped PZT film is attributed to the textured LNO template, which has very small lattice mismatch with that of PZT as well as has the pseudo-perovskite structure as PZT. The W dopants cause strains in the PZT lattice, which further decrease the lattice mismatch between PZT (110) and LNO template. Thus, a strong (110) peak appeared and the orientation of the PZTW film is no longer highly (l00) oriented.

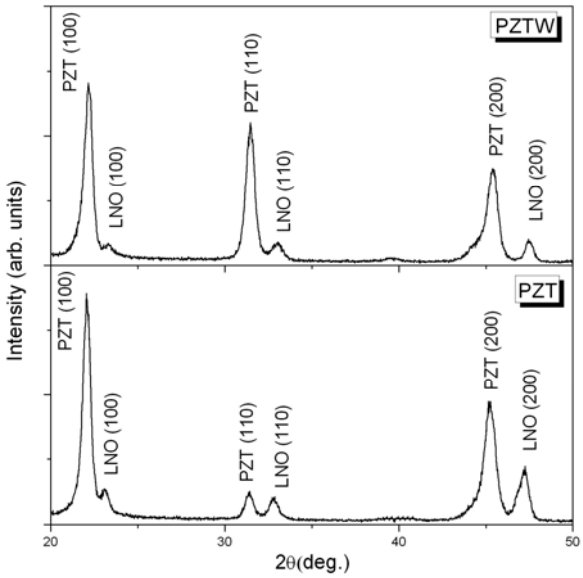

Figure 8.1: XRD θ-2θ scans of the highly (100) oriented PZT and PZTW thin films on silicon substrates with the LNO bottom electrodes.

FESEM images of the PZT and PZTW thin films are shown in Figs 8.2a and 8.2b. It can be seen that both surfaces of the PZT and PZTW films are smooth and crack-free without droplets from laser ablation. The PZTW film seems much denser than the PZT film, and the surface of the PZTW film is also smoother. The average grain size of the PZT film is approximately 90 nm, while that of the PZTW film is slightly larger at about 105 nm. Although the cause of the microstructure changes has not been clearly understood, two reasons may explain these microstructure changes. Firstly, as Ti acts as the nucleation site in perovskite PZT due to its low crystallization temperature, the introduction of W dopants into PZTW reduces the number of crystalline sites. Secondly, the donor dopants may reduce the concentration of oxygen vacancy while W ions increase the domain wall mobility and reduce the precipitates at the grain boundary,

which subsequently expedites the crystalline of the perovskite structure.

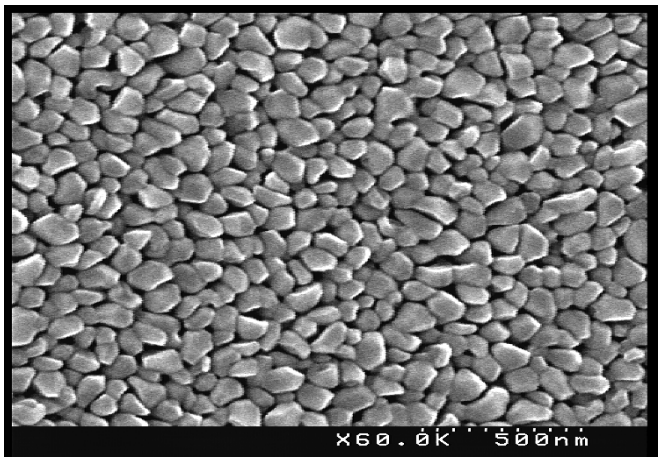

(a)

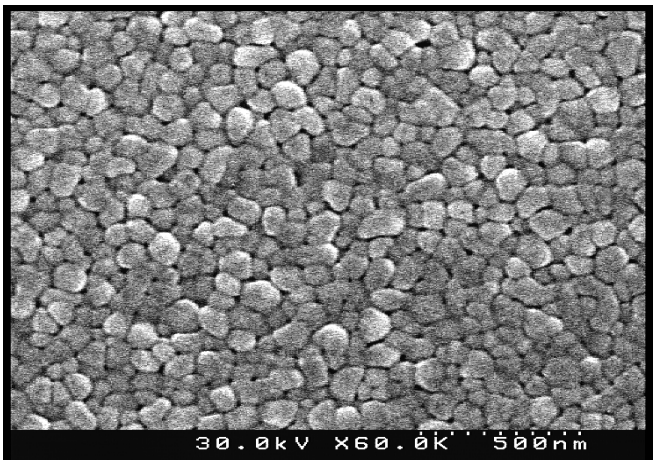

(b)

Figure 8.2: Surface morphology of PZT (a) and PZTW (b) thin films.

Figure 8.3 shows the SIMS depth profiles of the PZT/LNO and PZTW/LNO. The profiles indicate that there is no obvious interdiffusion between the PZT (PZTW) layer and the LNO bottom electrode (Figure 8.3). The low deposition temperature, short

deposition time due to the high deposition rate of pulsed laser deposition (PLD), and a large enough target-substrate distance inhibit the migration of elements. The presence of the dopant W is also confirmed by the SIMS analysis. And the thickness from this profile is close to the value measured from cross-sectional FESEM.

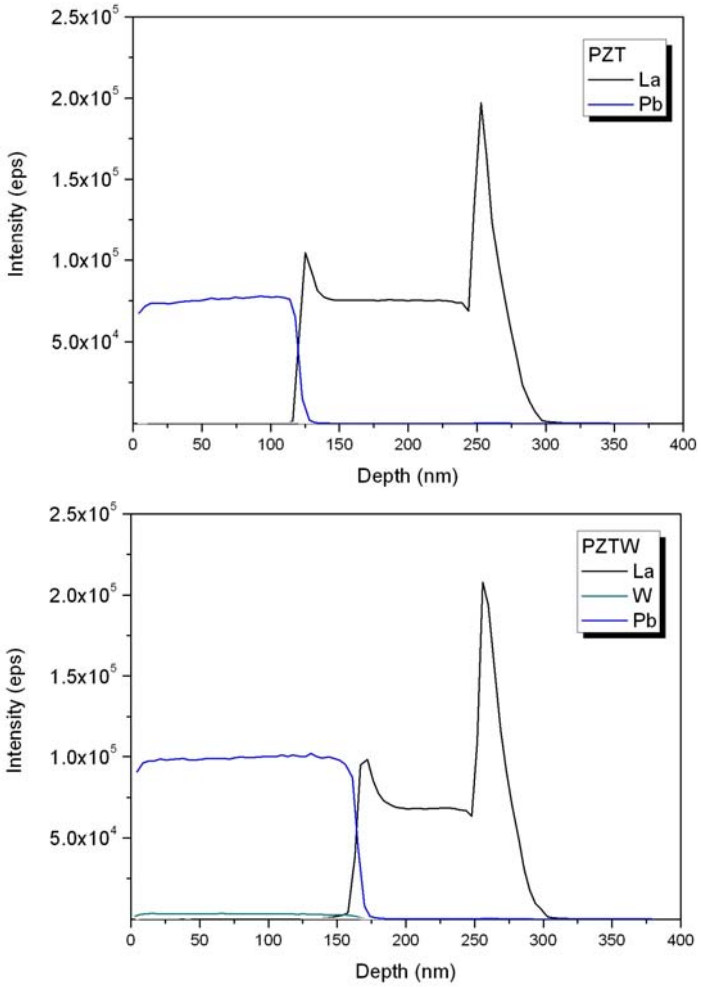

Figure 8.3: SIMS depth profile of the PZT and PZTW thin film deposited on LNO bottom electrodes.

Figure 8.4 shows the XPS spectrum of PZT and PZTW films. The spectrum of

PZTW film confirms the existence of W in PZTW films. Moreover, no appreciable difference in the spectral shape of Pb *4f*, Ti *2p*, Zr *3d*, and O *1s* is observed between PZT and PZTW, which indicates that W doping with small doping level (1 mol %) does not lead to changes of the valence states of other ions. XPS was also used to investigate the oxidation states of tungsten in the PZTW thin films. As shown in Figure 8.4, W $4f_{7/2}$ in the as-deposited thin film has a binding energy of 35.0 eV, while W $4f_{5/2}$ has an energy of 37.0 eV, which confirms that W ions are in the +6 valence state.

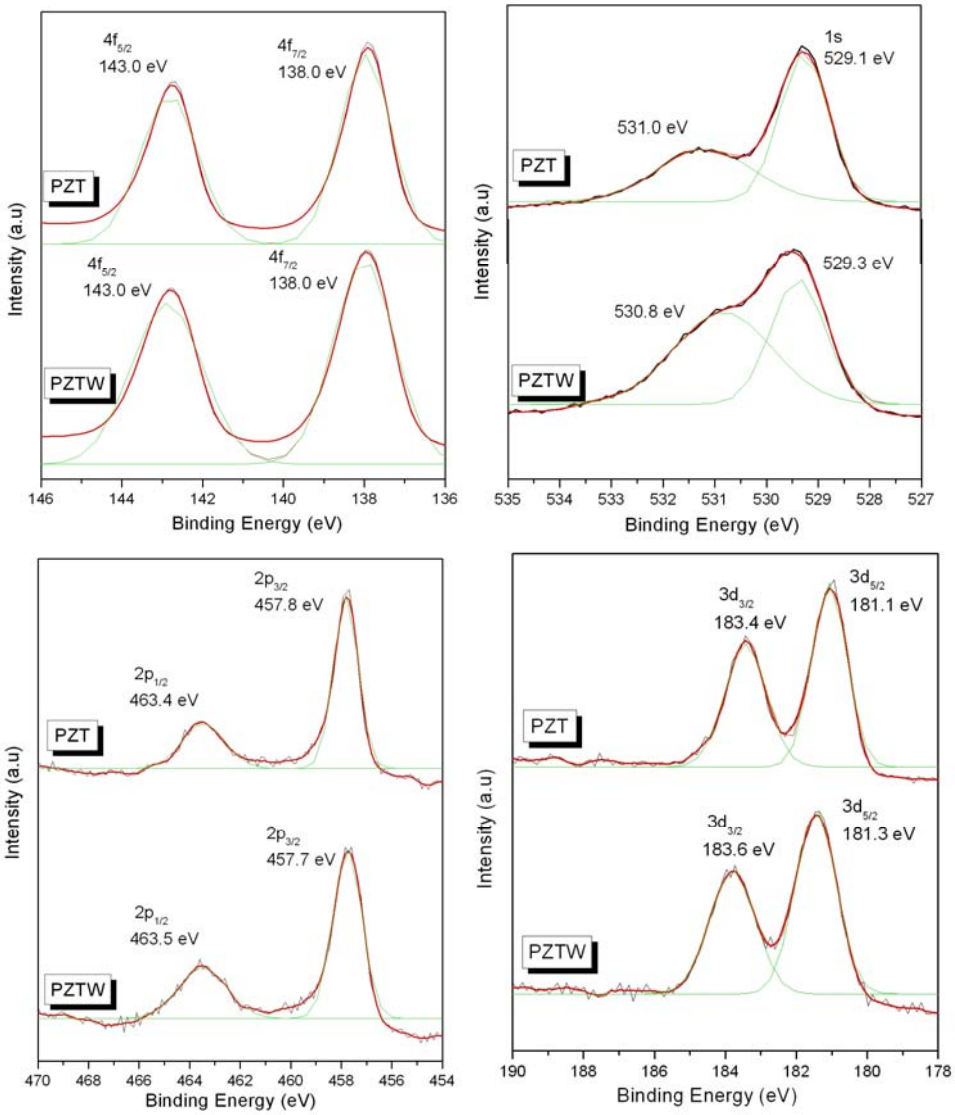

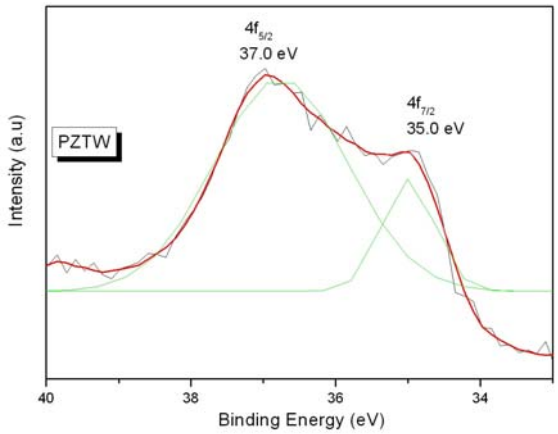

Figure 8.4: High resolution spectra of (1) Pb *4f*, (2) O *1s*, (3) Ti *2p*, (4) Zr *3d*, and (5) W *4f* photoelectrons for the PZT and PZTW thin films.

8.4 Effects on Ferroelectric Property and Fatigue Behavior

Figure 8.5 reveals the coercive field, saturation polarization, and the remnant polarization of the Au/PZTW/LNO and Au/PZT/LNO capacitors. The asymmetry of the two hysteresis loops is caused by the different materials of the electrodes which result in built-in electric fields at the ferroelectric/electrode interfaces. The remnant polarization and the saturation polarization of the PZT thin film are 20.16 and 35.20 μC/cm^{-2}, respectively, and the coercive field is 41.25 kV/cm. While the saturation polarization and coercive field of the PZTW thin film were found to be 46.50 μC/cm^{-2} and 29.65 kV/cm, smaller than those of the PZT films, the remnant polarization is slightly increased to 16.05 μC/cm^{-2}. The changes in remnant polarization and coercive field by dopants have been discussed.[13–16,23,24] In the present case, the increased saturation polarization and lowered coercive field may be explained by increase in the mobility of domain walls,

which was achieved by suppression of the oxygen vacancies. The decreased remnant polarization of the PZTW thin film is attributed to the increased (110)-oriented grains in PZTW thin film. Our observations on the Au/PZTW/LNO capacitors are similar to those observed from Pt/PZTW/Pt capacitors prepared by sol-gel technique [59].

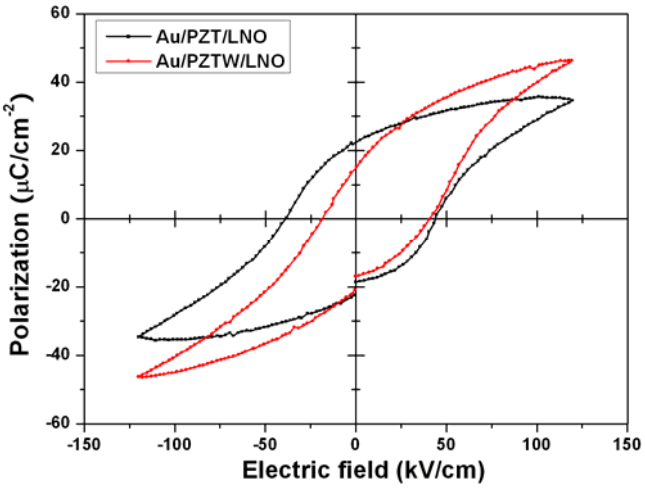

Figure 8.5: Hysteresis loops of polarization of Au/PZT/LNO and Au/PZTW/LNO capacitors.

The fatigue measurement was carried out by repeated switching under 70 kV/cm square waves with a frequency of 50 kHz. Figure 8.6 shows the normalized fatigue behavior of the PZT and PZTW films. The slight asymmetry of the positive and negative normalized polarization is due to the different materials used as top and bottom electrodes. It is clear that the PZTW thin film possesses better fatigue behavior than that of the PZT thin film. The normalized remnant polarization of the PZT film decreases by about 65% at Au side and about 45% at LNO side after 2.6×10^{10} cycles. However, there is only about 10% reduction in remnant polarization for the PZTW film at the LNO side, and about 20% at the Au side.

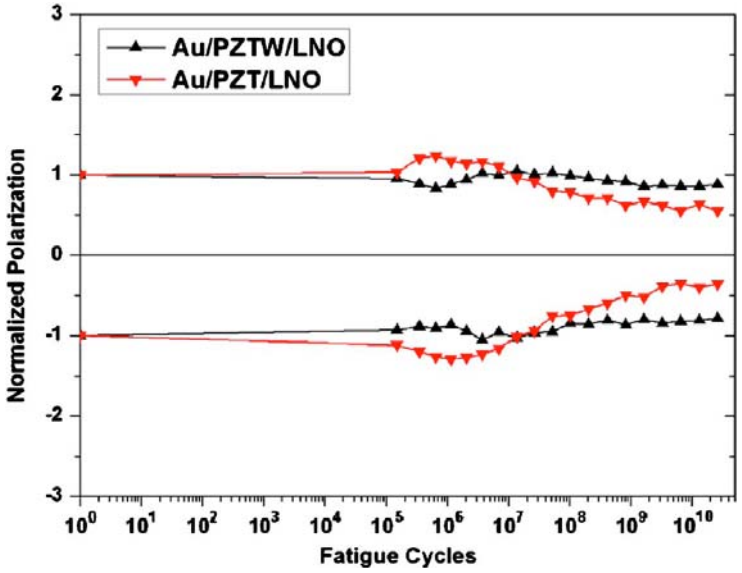

Figure 8.6: Comparison of fatigue properties of Au/PZT/LNO and Au/PZTW/LNO capacitors.

8.5 Summary

$Pb(Zr_{0.3}Ti_{0.7})O_3$ thin films doped with 1 mol % W have been successfully grown on $LaNiO_3$ bottom electrodes using pulse laser deposition. X-ray diffraction analyses reveal that the films grow with high (l00) orientations. The W doping induces changes in the microstructure of the PZT films, where smoother surface and reduced porosity were observed. Although the remnant polarization PZTW is lower than that of the PZT film, the PZTW film showed higher saturation polarization, lower coercive field, and better fatigue behavior, suggesting suppression of oxygen vacancies in PZT thin films by dopant W. As our theoretical results have indicated that the formation energy of oxygen vacancies in Pb-deficient conditions can be greatly increased by W doping, and

furthermore, the W *5d* states share the conduction band minimum with Ti *3d* states, which helps to reduce the occupation of Ti *3d* states by the electrons released from oxygen vacancies. Therefore, the experimental results are consistent with our theoretical predictions that the PZTW is less susceptible to fatigue.

Chapter IX

Summary and Future Work

9.1 Summary

We have systematically and exaustively invetsigated the effects of elemental substitution on the ferroelectric properties of lead zirconate titanate, using *ab initio* density functional theory calculations. Different candidates of dopants are selected by screening the periodical table of elements, by matching the ionic sizes with the original ions, and by choosing the desired valences for donors and acceptors. In our studies, group VA, VIA elements (B-site donors), group IIA elements (A-site donors), group IIIB elements (B-site acceptors), group VB elements (A-site donor, B-site acceptor/donors), and 3d transition metals (B-site acceptor) are investigated. For each substituted system, the electronic structure, defect structure and defect formation are examined.

Our studies reveal that there are different mechanisms behind the improved ferroelectric properties of PZT especially the fatigue behaviors for donor substitutions and acceptor substitutions. The conclusions are summarized below:

(1) For donors substitutions, we conclude that two mechanisms contribute to the improved ferroelectric properties of the donor substituted PZT. First, the formation energy of the oxygen vacancies is increased by the donors, resulting in a diluted oxygen vacancy concentration in the lead zirconate titanate lattice. Therefore, the domain pinning effect and space charge effect are reduced. Second, the donor states share the conduction band minima with the Ti 3d states, reduce the occupation of the Ti 3d states by the electrons, and weaken

the electronic suppression effect on the polarization in lead zirconate titanate. More practically, our calculations predict that group VA elements (V, Nb, Ta) and group VIA element (W, Mo) as B-site donors, and group IIIA elements (Sc, Y and La) as A-site donors can effectively improve the ferroelectric properties and fatigue of PZT. It is noteworthy that our experimental results also confirm the predictions of our theoretical studies.

(2) It is also interesting to observe the systematic variation in the band gaps of lead zirconate titanate with the dopants. Moreover, for group IIIA elements doped lead titanate as A-site donors, we found that correlations between the dopant electrons introduce the Mott-Hubbard band gap into PZT, which is intrinsically a charge-transfer insulator. This leads to a systematic reduction of energy and optical band gaps with increased atomic number of group IIIA substitutions. A similar chemical trend was found for group VB substitutions, which is closely related to the electron bandwidth of Ti 3d states in the charge-transfer band gaps. Our theoretical calculations show that all the trivalent dopants effectively dilute the concentration of the oxygen vacancies under Pb-deficient conditions.

(3) For acceptors substitutions, the mechanisms dominating the substitution effects on the improved ferroelectric properties are related to the defect structures. Three defect structures of the acceptors and the oxygen vacancies are identified. More importantly, our calculations reveal that the

acceptor-oxygen-vacancy-acceptor cluster structure either along z direction or in xy plane is energetically preferred for most acceptors substituted lead zirconate titanate. This cluster configuration greatly reduces the oxygen vacancy mobility, therefore diminishing the domain pinning effects and space charge effects. Moreover, close examination of the atomic positions in the clusters indicates that the domain pinning caused by the tail-to-tail polarization patterns along the z direction are relieved by the group IIIB and 3d transition metal dopants. The more striking finding is that group VB dopants induce head-to-head polarization patterns in the xy plane, which makes the domain pinning effects even weaker.

We expect that our study will make great contributions to the community. Firstly, our study enhances the scientific understanding of the microscopic mechanisms behind various types of doping. Secondly, from an engineering point of view, our reasonable predictions of the improved ferroelectric properties of lead zirconate titanates by certain substitutions can guide the experimentalists, narrow their scope of searching, and finally expedite the commercialization of lead zirconate titanate based devices.

9.2 Future Work

Although some of our conclusions have been confirmed by the available experimental results, further work is still needed to verify some important findings as listed below:

(1) No work has confirmed the two distinct defect-cluster structures favored by the group IIIB and group VB acceptors, which are along the z direction and in the xy plane respectively. It could be challenging work.

(2) Since ferroelectric properties are determined by the microstructures of the lead zirconate titanate thin films, which was not featured by our first-principle calculations, optimal grain growth parameters must be found by experimentalists in order to fabricate high performance ferroelectric thin films.

(3) Defect induced magnetism is of great interest in the search of new multiferroic materials, which may become an important future work since we have worked out the defect formation mechanism.

REFERENCE

[1] Tejuca, L.G. and J.L.G. Fierro, *Properties and Applications of Perovskite-Type Oxides,*(CRC Press,1993)

[2] Scott, J.F., Science **315**, p. 954 (2007)

[3] Lines, M.E., *Principles and Applications of Ferroelectrics and Related Materials,*(1977)

[4] Xu, Y., *Ferroelectric materials and their applications,*(North-Holland New York, NY,1991)

[5] Uchino, K., *Ferroelectric Devices,*(Marcel Dekker,2000)

[6] Ishiwara, H., M. Okuyama, and Y. Arimoto, *Ferroelectric Random Access Memories: Fundamentals and Applications,*(Springer,2004)

[7] Scott, J.F. and C.A. Paz de Araujo, Science **246**, p. 1400 (1989)

[8] Scott, J.F., Ferroelectrics Review **1**, p. 1 (1998)

[9] Dawber, M., K.M. Rabe, and J.F. Scott, Reviews of Modern Physics **77**, p. 1083 (2005)

[10] Auciello, O., J.F. Scott, and R. Ramesh, Physics Today **51**, p. 22 (1998)

[11] Scott, J.F., et al., Journal of Applied Physics **70**, p. 382 (1991)

[12] Scott, J.F. and M. Dawber, Applied Physics Letters **76**, p. 3801 (2000)

[13] Poykko, S. and D.J. Chadi, Applied Physics Letters **75**, p. 2830 (1999)

[14] Meyer, B. and D. Vanderbilt, Physical Review B **65**, p. 104111 (2002)

[15] He, L. and D. Vanderbilt, Physical Review B **68**, p. 134103 (2003)

[16] Xiangyi, F., et al., Ferroelectrics **281**, p. 163 (2002)

[17] Miura, K. and M. Tanaka, Jpn. J. Appl. Phys **35**, p. 2719 (1996)

[18] Yu, Y.J., et al., Applied Physics A: Materials Science & Processing **78**, p. 733 (2004)

[19] Vijay, D.P. and S.B. Desu, Journal of the Electrochemical Society **140**, p. 2640 (1993)

[20] Zou, Q., et al., Thin Solid Films **402**, p. 65 (2002)

[21] Zheng, H., et al., Journal of the European Ceramic Society **21**, p. 1371 (2001)

[22] Shannigrahi, S.R. and H.M. Jang, Applied Physics Letters **79**, p. 1051 (2001)

[23] Lee, W.I. and J. Lee, Materials Research Bulletin **30**, p. 1185 (1995)

[24] Klissurska, R.D., et al., Journal of the American Ceramic Society **78**, p. 1513 (1995)

[25] Haccart, T., D. Remiens, and E. Cattan, Thin Solid Films **423**, p. 235 (2003)

[26] Chen, J., M.P. Harmer, and D.M. Smyth, Journal of Applied Physics **76**, p. 5394 (1994)

[27] Zhang, Q. and R.W. Whatmore, Journal of Physics D: Applied Physics **34**, p. 2296 (2001)

[28] Meštrić, H., et al., Phys Rev B **71**, p. 134109

[29] Erhart, P., et al., Physical Review B **76**, p. 174116 (2007)

[30] Eichel, R.A., et al., Physical Review Letters **100**, p. 95504 (2008)

[31] Eichel, R.A., Journal of the American Ceramic Society **91**, p. 691 (2008)

[32] Ignatiev, A., et al., Materials Science & Engineering B **56**, p. 191 (1998)

[33] Ryder, D.F. and N.K. Raman, Journal of Electronic Materials **21**, p. 971 (1992)

[34] Choi, G.P., et al., Materials Science & Engineering B **41**, p. 16 (1996)

[35] Carim, A.H., et al., Journal of the American Ceramic Society **74**, p. 1455 (1991)

[36] Klissurska, R.D., K.G. Brooks, and N. Setter, Ferroelectrics **225**, p. 171 (1999)

[37] Tagantsev, A.K., et al., Journal of Applied Physics **90**, p. 1387 (2001)

[38] Parr, R.G. and W. Yang, *Density-Functional Theory of Atoms and Molecules,*(Oxford University Press, USA,1989)

[39] Koch, W. and M.C. Holthausen, *A chemist's guide to density functional theory,*(Wiley-VCH New York,2001)

[40] Dreizler, R.M. and E.K.U. Gross, *Density functional theory,*(Springer-Verlag New York,1990)

[41] Miura, K. and M. Tanaka, Jpn. J. Appl. Phys **36**, p. 226 (1997)

[42] Miura, K. and M. Tanaka, Jpn. J. Appl. Phys **35**, p. 3488 (1996)

[43] Meštrić, H., et al., Physical Review B **71**, p. 134109 (2005)

[44] Setter, N. and E.L. Colla, *Ferroelectric Ceramics: Tutorial Reviews, Theory, Processing, and Applications,*(Birkhauser,1993)

[45] Nagel, N., et al., MRS Symposium Proceedings **655**, p.

[46] Kinney, W., INTEGR FERROELECTR **4**, p. 131 (1994)

[47] Scott, J.F. and B. Pouligny, Journal of Applied Physics **64**, p. 1547 (1988)

[48] Gruverman, A., O. Auciello, and H. Tokumoto, Applied Physics Letters **69**, p. 3191 (1996)

[49] Colla, E.L., et al., Applied Physics Letters **72**, p. 2763 (1998)

[50] Brennan, C., Ferroelectrics **150**, p. 199 (1993)

[51] Arlt, G. and H. Neumann, Ferroelectrics **87**, p. 109 (1988)

[52] Scott, J.F. and M. Dawber, Applied Physics Letters **76**, p. 3801 (2000)

[53] Woodward, D.I., et al., Applied Physics Letters **84**, p. 4650 (2004)

[54] Park, C.H. and D.J. Chadi, Physical Review B **57**, p. R13961 (1998)

[55] Scott, J.F., et al., Journal of Applied Physics **70**, p. 382 (1991)

[56] Dimos, D., et al., Journal of Applied Physics **76**, p. 4305 (1994)

[57] Poykko, S. and D.J. Chadi, Journal of Physics and Chemistry of Solids **61**, p. 291 (2000)

[58] Chae, B.G., et al., Thin Solid Films **410**, p. 107 (2002)

[59] Zou, Q., H.E. Ruda, and B.G. Yacobi, Applied Physics Letters **78**, p. 1282 (2001)

[60] Nakamura, T., et al., Integrated Ferroelectrics **9**, p. 179 (1995)

[61] Wang, Y., et al., Applied Physics Letters **80**, p. 97 (2002)

[62] Lee, J., et al., Applied Physics Letters **72**, p. 3380 (1998)

[63] de Araujo, C.A.P., et al., Nature **374**, p. 627 (1995)

[64] Zhang, R.F., et al., Solid State Ionics **166**, p. 219 (2004)

[65] Shannigrahi, S. and K. Yao, Applied Physics Letters **86**, p. (2005)

[66] Majumder, S.B., Y.N. Mohapatra, and D.C. Agrawal, Applied Physics Letters **70**, p. 138 (1997)

[67] Cheng, W.X., et al., Integrated Ferroelectrics **75**, p. 173 (2005)

[68] Iijima, T., et al., Jpn. J. Appl. Phys., Part 1 **39**, p. 5426 (2000)

[69] Choi, W.-Y., et al., Materials Letters **37**, p. 119 (1998)

[70] de Gironcoli, S., S. Baroni, and R. Resta, Physical Review Letters **62**, p. 2853 (1989)

[71] King-Smith, R.D. and D. Vanderbilt, Physical Review B **47**, p. 1651 (1993)

[72] Resta, R., Reviews of Modern Physics **66**, p. 899 (1994)

[73] King-Smith, R.D. and D. Vanderbilt, Physical Review B **49**, p. 5828 (1994)

[74] Singh, D.J. and L. Nordstrom, *Planewaves, Pseudopotentials, And the Lapw Method,*(Springer Verlag,2006)

[75] Blaha, P., et al., Computer Physics Communications **59**, p. 399 (1990)

[76] Andersen, O.K., Z. Pawlowska, and O. Jepsen, Physical Review B **34**, p. 5253 (1986)

[77] Hamann, D.R., M. Schlüter, and C. Chiang, Physical Review Letters **43**, p. 1494 (1979)

[78] Kresse, G. and J. Hafner, (1994)

[79] Vanderbilt, D., Phys. Rev (1990)

[80] Kresse, G. and D. Joubert, Physical Review B **59**, p. 1758 (1999)

[81] Blöchl, P.E., Physical Review B **50**, p. 17953 (1994)

[82] Wu, Z., R.E. Cohen, and D.J. Singh, Physical Review B **70**, p. 104112 (2004)

[83] Kresse, G. and J. Hafner, Physical Review B **47**, p. 558 (1993)

[84] Kresse, G. and J. Furthmüller, Physical Review B **54**, p. 11169 (1996)

[85] Gonze, X., et al., Computational Materials Science **25**, p. 478 (2002)

[86] Soler, J.M., et al., Journal of Physics: Condensed Matter **14**, p. 2745 (2002)

[87] Dovesi, R., et al., Zeitschrift Fur Kristallographie **220**, p. 571 (2005)

[88] Feynman, R.P., Physical Review **56**, p. 340 (1939)

[89] Nielsen, O.H. and R.M. Martin, Physical Review B **32**, p. 3780 (1985)

[90] Cohen, R.E. and H. Krakauer, Ferroelectrics **136**, p. 65 (1992)

[91] Cohen, R.E. and H. Krakauer, Physical Review B **42**, p. 6416 (1990)

[92] Cohen, R.E., Nature **358**, p. 136 (1992)

[93] Resta, R., Modelling and Simulation in Materials Science and Engineering **11**, p. R69 (2003)

[94] Singh, D.J., Physical Review B **52**, p. 12559 (1995)

[95] Poykko, S. and D.J. Chadi, Applied Physics Letters **76**, p. 499 (2000)

[96] Betsuyaku, K., et al., Jpn. J. Appl. Phys., Part 1 **40**, p. 6911 (2001)

[97] Man, Z.Y. and X.Q. Feng, Solid State Communications **123**, p. 333 (2002)

[98] Robertson, J., Journal of Applied Physics **93**, p. 1054 (2003)

[99] Astala, R. and P.D. Bristowe, Computational Materials Science **22**, p. 81 (2001)

[100] Suzuki, T. and M. Fujimoto, Journal of Applied Physics **89**, p. 5622 (2001)

[101] Li, H., et al., Applied Physics Letters **81**, p. 4398 (2002)

[102] Kohn, W. and L.J. Sham, Physical Review (1965)

[103] Robertson, J., et al., (1996)

[104] Hohenberg, P. and W. Kohn, (1964)

[105] Pople, J.A. and D.L. Beveridge, *Approximate molecular orbital theory,*(McGraw-Hill, New York,1970)

[106] Vosko, S.H., L. Wilk, and M. Nusair, Canadian Journal of Physics **59**, p. 1200 (1980)

[107] Perdew, J. and A. Zunger, Physical Review B **23**, p. 5048 (1981)

[108] MacDonald, A.H. and S.H. Vosko, Journal of Physics C: Solid State Physics **12**, p. 2977 (1979)

[109] Wang, Y. and J.P. Perdew, Phys Rev B Condens Matter **44**, p. 13298 (1991)

[110] Perdew, J.P., K. Burke, and M. Ernzerhof, Physical Review Letters **77**, p. 3865 (1996)

[111] Lee, C., W. Yang, and R.G. Parr, Physical Review B **37**, p. 785 (1988)

[112] Perdew, J.P. and Y. Wang, Physical Review B **45**, p. 13244 (1992)

[113] Bloch, F., Zeitschrift für Physik A Hadrons and Nuclei, **52**, p. 555 (1929)

[114] Monkhorst, H.J. and J.D. Pack, Physical Review B **13**, p. 5188 (1976)

[115] G. Lehmann, M.T., Physica Status Solidi (b) **54**, p. 469 (1972)

[116] Samara, G.A., Ferroelectrics **73**, p. 145 (1987)

[117] Vanderbilt, D., Current Opinion in Solid State & Materials Science **2**, p. 701 (1997)

[118] Sághi-Szabó, G., R.E. Cohen, and H. Krakauer, Physical Review B **59**, p. 12771 (1999)

[119] Sághi-Szabó, G., R.E. Cohen, and H. Krakauer, Physical Review Letters **80**, p. 4321 (1998)

[120] Piskunov, S., et al., Computational Materials Science **29**, p. 165 (2004)

[121] Ghosez, P., et al., Physical Review B **60**, p. 836 (1999)

[122] Shirane, G., R. Pepinsky, and B.C. Frazer, Acta Cryst. **9**, p. 131 (1956)

[123] Migoni, R., H. Bilz, and D. Berle, Physical Review Letters **37**, p. 1155 (1976)

[124] Bersuker, I.B., PHYS LETT **20**, p. 589 (1966)

[125] Gerson, R., Journal of Applied Physics **31**, p. 188 (1960)

[126] Gerson, R. and H. Jaffe, Journal of Physics and Chemistry of Solids **24**, p. 979 (1963)

[127] Hau, S.K., et al., Applied Physics Letters **66**, p. 245 (1995)

[128] Du, X. and I.W. Chen, Journal of Applied Physics **83**, p. 7789 (1998)

[129] Chu, F., et al., Integrated Ferroelectrics **48**, p. 161 (2002)

[130] Burns, G. and B.A. Scott, Physical Review Letters **25**, p. 1191 (1970)

[131] V. M. Goldschmidt, Skr. Nor. Vidensk.-Akad., [Kl.] 1: Mat.-Naturvidensk. Kl. 8, 2 (1926)

[132] Zaanen, J., G.A. Sawatzky, and J.W. Allen, Physical Review Letters **55**, p. 418 (1985)

[133] Robey, S.W., et al., Physical Review B **48**, p. 562 (1993)

[134] Fujimori, A., et al., Physical Review B **46**, p. 9841 (1992)

[135] E.Erdem, et al., Functional Materials Letter 1, 1 (2008)

[136] Erdem, E., et al., Magnetic Resonance in Chemistry **43**, p. 174 (2005)

[137] Erdem, E., et al., phys. stat. sol.(b) **239**, p. R7 (2003)